MAJIS instrument characterization

MSc Thesis

Paolo Haffoud

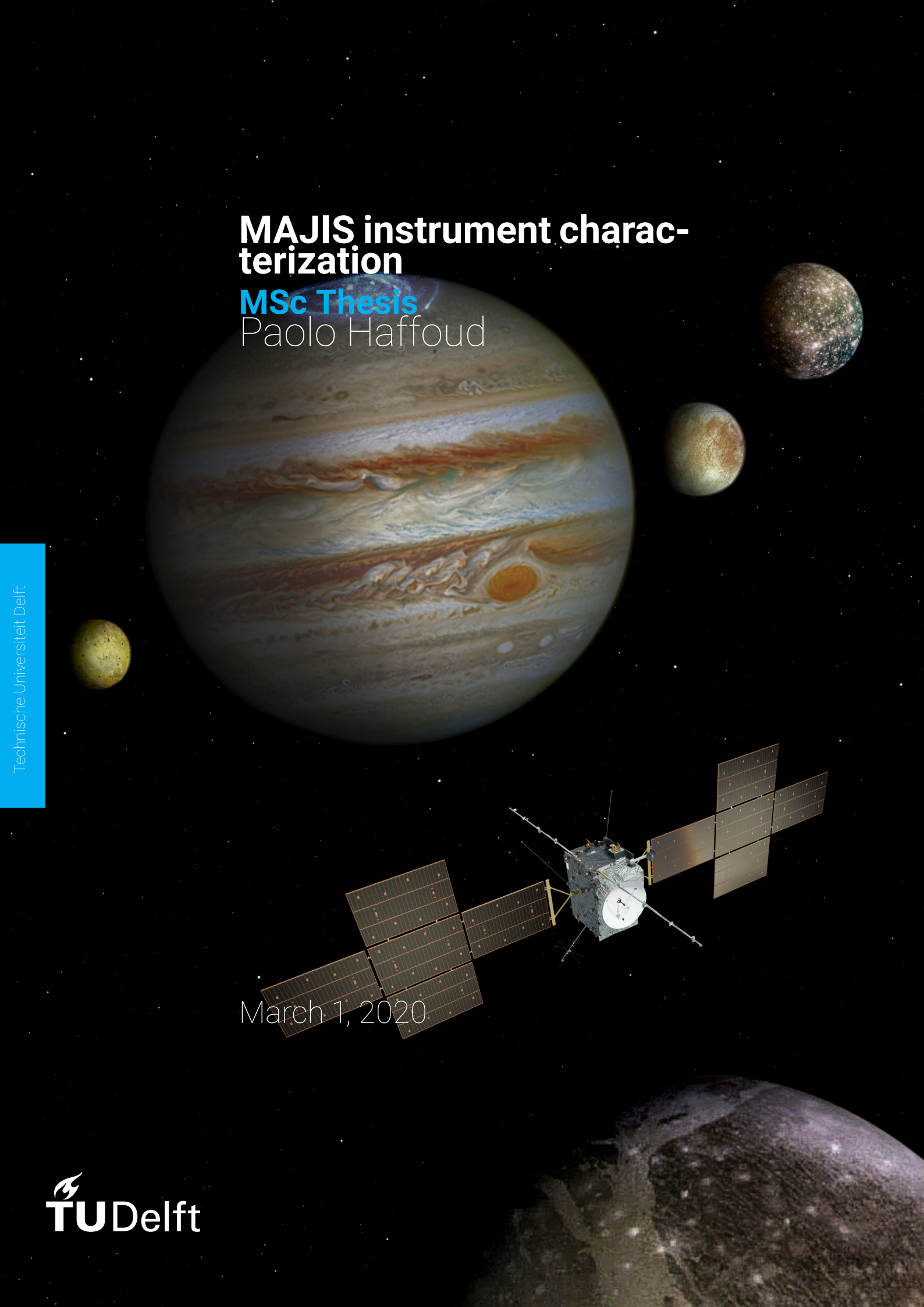

March 1, 2020

Technische Universiteit Delft

TU Delft

MAJIS instrument characterization
MSc Thesis

by

Paolo Haffoud

To obtain the degree of Master of Science
at the Delft University of Technology,
to be defended publicly on Tuesday March 24, 2020 at 02:00 PM.

Student number:	4739949	
Project duration:	June 3, 2019 – March 24, 2020	
Thesis committee:	Prof. Dr. B.R. Brandl,	TU Delft, supervisor
	Pr. Dr. L.L.A. Vermeersen,	TU Delft
	Pr. Dr. F. Poulet,	Institut d'Astrophysique Spatiale d'Orsay, external supervisor

An electronic version of this thesis is available at http:/repository.tudelft.nl/.

Cover image credits: ESA

TU Delft

Abstract

The JUICE (JUpiter ICy moons Explorer) mission by ESA aims to explore the emergence of habitable worlds around gas giants and the Jupiter system as an archetype for gas giants. MAJIS (Moons and Jupiter Imaging Spectrometer) is the visible to near-infrared imaging spectrometer onboard JUICE which will characterize the surfaces and exospheres of the icy moons and perform monitoring of the Jupiter atmosphere. The launch is scheduled for June 2022 with the first MAJIS observations inside the Jovian system occurring more than 7.5 years later. MAJIS will use two Teledyne H1RG detectors for both spectrometer channels (VIS-NIR and IR). For this mission, they will be operated in a non-standard way. The detectors will allow near/full-frame retrieval over short integration times (« 1 sec) while maintaining good noise performance. This is due to the relatively high levels of irradiance of the targets compared to the detector well depths, and to mitigate the high rate of radiation spikes from the Jovian environment. Additionally, the detectors will operate at higher temperatures than previous space missions due to stringent resources constraints, impacting the dark current levels. We will present the characterization strategy suitable for evaluating the performances of the VIS-NIR and MW-IR channel according to the MAJIS operational specifications. This methodology was tested during two characterization campaigns using two MAJIS Engineering Grade detectors. The first campaign was performed at the Institut d'Astrophysique Spatiale for the MW-IR detector. The second campaign was performed at the Institut royal d'Aéronomie Spatiale de Belgique for the VIS-NIR detector. This MSc thesis will describe the analyses and results of both campaigns. Based on these results, the capacity of MAJIS to reach its scientific objectives will be discussed.

Contents

Nomenclature

Acronyms

3GM	Gravity and Geophysics of jupiter and Galilean Moons
ADC	Analog-to-digital converter
BB	Black-body
BPF	Band-pass filter
CDS	Correlated double sampling
CREMA	Consolidated Report on Mission Analysis
DIT	Detector integration time
DVGA	DeltaV Gravity Assist
ESP	Extended Science Phase
FET	Field effect transistor
FOV	Field of view
FPA	Focal plane array
FPE	Focal plane electronics
FPU	Focal plane unit
FWC	Full well capacity
GALA	GAnymede Laser Altimeter
GCO-500	Ganymede Circular Orbit
GEO	Ganymede Elliptical Orbit
HAWAII	HgCdTe Astronomical Wide Infrared Imager
HR	High resolution
IAS	Institut d'astrophysique spatiale
IASB	Institut d'aéronomie spatiale de Belgique
IFOV	Instantaneous field of view
iPDR	Instruments Preliminary Design
J-MAG	JUICE MAGnetometer
JANUS	Jovis, Amorum ac Natorum Undique Scrutator
JUICE	Jupiter Icy Moons Explorer
JWST	James-Webb Space Telescope
LEE	Low Energy Endgame

LVF	Linear variable filter
MAJIS	Moons and Jupiter Imaging Spectrometer
MW-IR	Mid-wave infrared
NSP	Nominal Science Phase
OH	Optical head
OS	Oversampling
PEP	Particle Environment Package
PRIDE	Planetary Radio Interferometer and Doppler Experiment
QE	Quantum efficiency
RIME	Radar for Icy Moons Exploration
ROIC	Read-out Integrated Circuit
RPWI	Radio and Plasma Wave Investigation
S/C	Spacecraft
SPICE	Simulation Program with Integrated Circuit Emphasis
SWI	Sub-millimeter Wave Instrument
SWPF	Short-wave pass filter
UVS	Ultraviolet Spectrograph
VIS-NIR	Visible near-infrared

Greek Symbols

α	Absorption length	m
η	Quantum efficiency	
λ	Photon's wavelength	m
λ	Poisson parameter	
ν	Photon frequency	Hz
ϕ	Photon flux	$1/(\mathrm{m}^2 \cdot \mathrm{s})$
σ	Standard deviation	

Roman Symbols

C_0	Capacitance	F
d	Thickness of detector	m
G	Conversion gain	e-/DN
G_r	Volume generation rate	
h	Planck's constant	$\mathrm{m}^2 \cdot \mathrm{kg/s}$
J	Dark current	e-1/s
k	ADC conversion factor	V/DN

P_i	Incoming power	W
q	Charge of an electron	C
r	Reflectivity	
R_r	Volume recombination rate	
S_{DN}	Signal	DN
S_{e-}	Signal	e-
T	Absolute temperature	K
V_{max}	Maximum output voltage	V

List of Figures

List of Tables

1 Introduction

The **JUpiter ICy moons Explorer** (JUICE) mission is a space exploration mission of the European Space Agency (ESA) planned for a departure in 2022 [15]. JUICE is the first of the three L class missions that are currently part of the European Space Agency science program Cosmic Vision. The primary science objectives of JUICE derive from two of the four questions at the heart of the Cosmic Vision program. These two questions are [13]:

- *"What are the conditions for planet formation and the emergence of life?"*
- *"How does the Solar System work?"*

To help answering these questions JUICE will investigate Jupiter and its system using 10 instruments and one experiment. Particular importance will be given to the study of three icy moons of Jupiter: Ganymede, Europa, and Callisto.

The JUICE spacecraft is expected to launch on 2022 aboard an Ariane 5 launch vehicle for an arrival in 2029. During its 7-years cruise, it will make several gravity assists on the planets in the inner solar system before reaching the Jupiter system. MAJIS (Moons And Jupiter Imaging Spectrometer) is an imaging spectrometer in the VIS-NIR and MW-IR range. It is a key instrument for the JUICE mission. Similar instruments have been used aboard several space missions and have shown great results for the study of various bodies in the Solar System.

The MAJIS instrument will have significant contributions to the scientific success of the mission. Its observations will include the study of the chemical composition of the surface of the icy moons (organic species and non-ice water chemicals), the study of their exospheres, and the characterization of Jupiter's atmosphere, rings, and smaller moons.

MAJIS has two channels covering the spectral ranges: 0.5 to 2.35 µm (VIS-NIR) and 2.25 to 5.54 µm (MW-IR). Two H1RG detectors provided by Teledyne will be used for these two channels. The principal investigator for MAJIS is the Institut d'Astrophysique Spatiale d'Orsay. The IAS is among the leading research institutes dedicated to space sciences in France. Among other responsibilities, the IAS is responsible for the selection and characterization of the infrared detectors. An essential aspect of the characterization of the flight detectors is to ensure they fulfill the expected requirements.

1.1. Research questions and objectives

MAJIS is a complex instrument which involves multiple subsystems. All these subsystems have their own contributions to the SNR of MAJIS. The following diagram describes the main elements of the subsystems constituting MAJIS or entering into play for the measured performances:

Figure 1.1: Overview of the elements contributing to the SNR of the MAJIS instrument

The main objective of this thesis is to participate in the characterization of the detectors (FPA) for the space instrument MAJIS (see † in Figure 1.1). The FPAs and FPEs performances will have a major impact on the SNR that the MAJIS instrument will have in-flight. However, there are numerous elements that will also contribute to the SNR which will not be treated in this thesis. The scope of this thesis is, therefore, limited to

aspects which are relevant to the characterization of the detectors of MAJIS. With this aim the following main research questions have been formulated:

- **How does the MAJIS instrument operate ?** What is the role of the detectors in the overall performances of the instrument ? What are the operational specificities of the detectors and their impacts to the MAJIS instrument acquisition modes ?
- **What are the procedures to characterize the detectors' various performance parameters?** These parameters include:
  - Linearity
  - Full-well capacity
  - Quantum efficiency
  - RON
  - Gain
  - Dark current
  - Latency
  - Operability
- **Are the two experimental characterization set-ups dedicated to the two channels working as expected?** Can all measurements be performed successfully? The MAJIS detector being very sensitive to the straylight, what level of stray-light is present?
- **What are the performances of the MW-IR and VIS-NIR EM detectors ?** Do any potential issues with the **FM** detectors arise from the characterization of the **EM** detectors?
- **What is the impact of the detector's performances on the performances of the MAJIS instrument?** Will the **FM** detectors allow the instrument to reach its scientific goals ?

The MAJIS development is driven by a complex consortium with several public and private institutes. It is out of the scope of this MSC thesis to tackle all the development aspects and evaluating the performances of each sub-system. The thesis is therefore focused on specific aspects of the instrument, namely the characterization of the focal planes. As the planning of the instrument shifted during the thesis, the results presented in this work concern the engineering models of the detectors. The characterization objectives are similar to the FM models, although slightly degraded in terms of operational parameters. Regarding to the JUICE mission, the objectives related to the study of the Icy moons are the ones mainly addressed.

1.2. Thesis outline

This MSc thesis is composed of two parts. Chapter 2, 3, and 4 form a summary of the literature study completed during the thesis. Chapter 5, 6, 7, and 8 compose the original work of the MSc thesis.

Chapter 2 gives a description of the JUICE mission, its context, and the main objectives it tries to achieve. In addition, the MAJIS objectives are also presented. Following this, in Chapter 3, the MAJIS instrument is introduced from a technical point of view. Chapter 4 is dedicated to summarizing the physics of the detectors used on the MAJIS instrument. This chapter includes a general summary of the physics of infrared detectors and a more specific description relating to the type of detector used for MAJIS.

Chapter 5 presents, in detail, the methodology used for the characterization campaigns of the detectors. The methodology contains the data-reduction, the characterization procedures, and a description of the experimental set-up used for the VIS-NIR and MW-IR campaigns. Chapter 6 and Chapter 7, respectively describe the results of the MW-IR EM FPA campaign performed at the IAS and the VIS-NIR EM FPA campaign performed at the IASB. These two chapters also include discussions on the consequences for the instrument while in-flight. Within Chapter 8, the impact on the performances of the MAJIS instrument is addressed. This is based on the current models of the instrument and the updated expected performances of the detectors, as they have been studied during this MSc thesis. Finally, a general conclusion is reached in Chapter 9, recommendations for future work are also proposed.

2

MAJIS/JUICE Objectives

In this chapter, a general overview of the JUICE mission and the MAJIS instrument will be given. The JUICE mission builds upon several previous missions that explored the Jovian system. The most notable one being NASA's Galileo mission, which was dedicated to the study of Jupiter and its moons.
Based on our current scientific knowledge and the observations of previous missions, the Cosmic Vision program put the conditions for the emergence of life and the working of the Solar System as two of its main subjects of interest. Following these goals, the JUICE mission will try to investigate the habitability of the Galilean moons of Jupiter and investigate Jupiter as a typical example for gas giants.

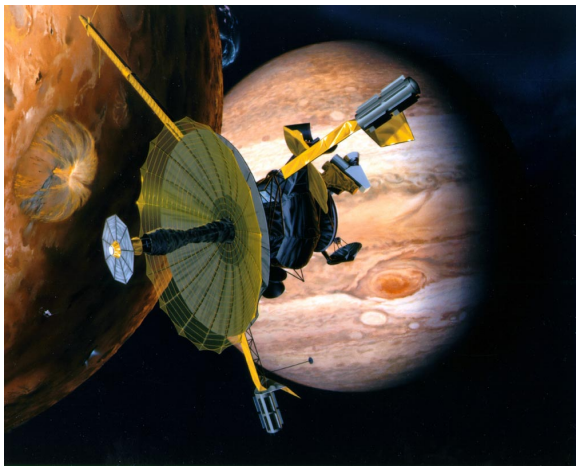

Figure 2.1: Galileo Mission - Nasa [26]

The MAJIS instrument is one of the 10 instruments that will be aboard the spacecraft to reach its scientific goals. As a spectrometer, MAJIS will mainly analyze the composition of the surface of the icy moons and characterize the atmosphere of Jupiter.

First, a description of the mission and the history of the exploration of Jupiter's system will be made. Then, the primary mission phases will be summarized, and the planned trajectory of the JUICE spacecraft will be described. Finally, the scientific objectives of the JUICE mission and more specifically, the MAJIS instrument w.r.t. Ganymede, Europa, and Callisto will be detailed.

2.1. Mission description and history

2.1.1. History

The Jovian system was initially explored through the flybys of the Pioneers mission (1972, 1973) which took the first images of Io, Europa, Ganymede and Callisto with a low resolution [12]:

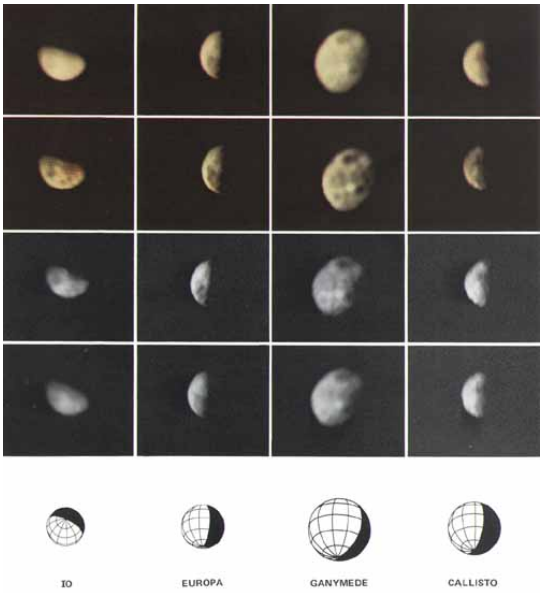

Figure 2.2: Pioneer 10 first images of the moons of Jupiter

NASA's Voyager missions (1977) were the next to explore Jupiter's system with two flybys. The scientific objectives focus was on the moons and the ring system. They detected ice water on the surface of Europa and volcanic activity on Io [12].

The NASA and ESA collaborative mission Ulysses (1990), focused on the study of the Sun. However, it took advantage of its two gravity assists around Jupiter to investigate the Jovian magnetosphere [12].
The Galileo mission was launched in 1989 and reached Jupiter's orbit in 1995 [20]. It was the first mission to enter into an orbit around Jupiter. It led to many scientific discoveries about the Jovian system. A few notable ones are [20]:

- It confirmed Voyager's observations of volcanic activity on Io [23]
- It indicated the possibility that a subsurface ocean existed under the surface of Europa [17] [22]
- It discovered that Ganymede had its own intrinsically produced magnetosphere [4]
- It found that ammonia clouds were present in Jupiter's atmosphere [16]

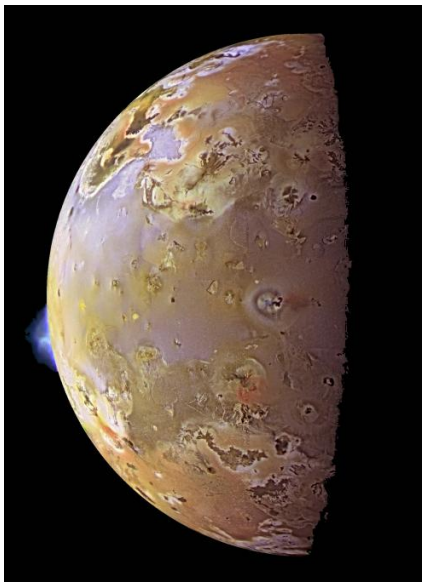

Figure 2.3: Io's volcanic activity - Galileo - Nasa [25]

The JUICE mission is the next step in the exploration of the Jovian system. It builds upon the discoveries of those previous missions and will try to investigate the potential habitability of Ganymede, Europa, and Callisto.

2.1.2. Targets

The observational cases that this thesis will focus on are based on the important targets of the JUICE mission. One important goal of JUICE is the exploration of three of the Galilean moons (Ganymede, Europa, and Callisto) as potential habitats.

1. *Ganymede*

   Ganymede is the largest moon of Jupiter and the largest moon in the Solar system. With a radius of 2,634 km, it is even larger than Mercury. It is the third farthest Galilean moon from Jupiter. Under its surface, it has a subsurface liquid water ocean. It is the only moon known to have its own magnetic field. It has a small iron-rich liquid core. Its thick mantle is composed of silicate minerals and ice. It also has a thin heavily-cratered icy crust surface. [12]

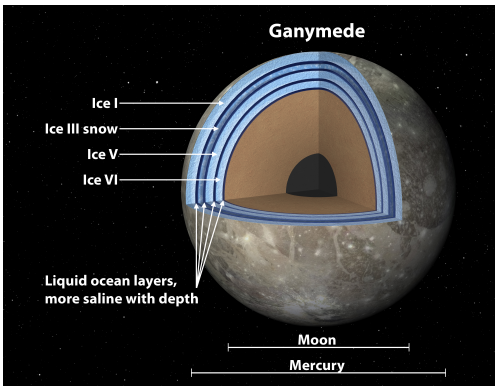

Figure 2.4: Ganymede's internal structure - Nasa [27]

2. *Europa*

   Europa is the fourth-largest moon of Jupiter. It is the second farthest away Galilean satellite. It has a radius of 1,560 km. It is believed to have a metallic iron core surrounded by a silicate mantle. Its surface is a flat young icy crust. Because of its surface composition, Europa is one of the brightest objects in the Solar system with an albedo of 0.64. It is also believed to have a liquid subsurface water ocean. The ocean is kept liquid by the heating produced from the massive tidal forces Europa is subjugated to.

3. *Callisto*

   Callisto is the second-largest moon of Jupiter and the third-largest moon of the Solar system (Titan, in orbit around Saturn, is also larger). It has a radius of 2,410 km, which makes it similar to Mercury in size. It is the farthest of the Galilean satellites. It even orbits outside the main radiation belt of Jupiter. It is thought to have a small core composed of silicate minerals. It is possible that Callisto also has a subsurface ocean [21]. Callisto's surface is a very ancient cratered icy crust. [12]

2.1.3. Mission Description

The JUICE mission is expected to launch in June 2022 aboard an Ariane 5 rocket. Any delay on the launch date would imply switching to an Ariane 6 rocket for the mission. With a 2022 launch, the satellite would arrive in the Jovian system around 2029. The JUICE mission will be the first satellite to explore the outer Solar System not launched by NASA.

The JUICE mission is part of the Cosmic Vision program, which is the third campaign of space science and space exploration of the ESA. As part of this campaign, ten missions will be launched:

- Three large-class missions,
- five medium-class missions,
- two small class missions.

The JUICE mission is focused on two main topics. These are given in the Science Requirements Document [41] as:

- Emergence of habitable worlds around gas giants
- Jupiter system as an archetype for gas giants

To fulfil its objectives, JUICE will explore various relevant aspects of the Jupiter system. Ganymede, Europa, and Callisto's internal structures, exospheres, and surfaces shall be thoroughly investigated. The moons fall into two main categories, mostly rocky moons (Europa) and rocky and icy moons (Ganymede and Callisto). Some of the main features of interest of these moons are:

- Europa: Ice outer shell and subsurface ocean.
- Ganymede: Full planetary differentiation of the rocky interior and metallic core, thick outer ice shell and subsurface ocean.

- Callisto: Partial planetary differentiation with a rocky and icy interior. Possible subsurface ocean.

The JUICE mission objectives imply that the satellite shall investigate all the primary features of the Jupiter system and characterize the interactions that take place. The **blueprint** of the approach selected for JUICE can be described in three acts:

- Comparative study of the three moons of interest, with special care given to Ganymede's habitability and planetary characteristics.

- A thorough characterization of the magnetosphere, meteorology, composition, and structure of Jupiter's atmosphere from the top to the thermosphere.

- Study of the interactions within the Jupiter system, specifically of the tidal effects caused by Jupiter on all its moons and the electrodynamic couples between Jupiter and its moons' atmospheres, sub-surface oceans, and magnetospheres.

Overall, nineteen science objectives were established as a result of this blueprint. These objectives will be further described in this chapter.

2.2. Description of mission phases

2.2.1. Trajectories

The images from this section were captured using [14].

The trajectories of the JUICE spacecraft are an essential part of the analysis of the performances of the MAJIS instrument. The trajectories are going to determine the exact environmental conditions the instrument and the targets will be in during the observations.

The JUICE trajectories, based on the CREMA report, can be accessed through SPICE kernels dedicated to the analysis of the JUICE mission.

Trajectory description

The material presented in this section is taken from the version 3.0 of the CREMA report [8].

The mission is currently planned for a departure in 2022. The trajectory is composed of 3 successive main mission phases.

1. Interplanetary Transfer Phase (< 10 years)

2. Nominal Science Phase (> 3.5 years)

3. Extended Science Phase (> 100 days)

Interplanetary Transfer Phase

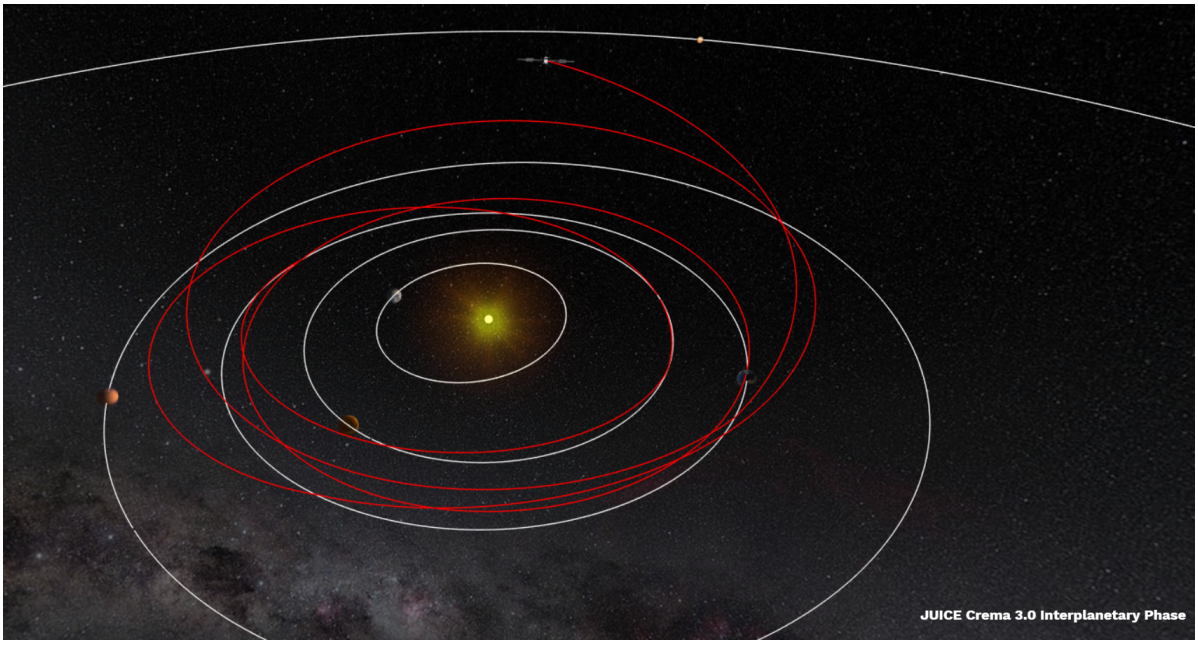

Figure 2.5: JUICE's interplanetary phase trajectory

During the interplanetary transfer, the S/C will travel from launch to insertion into Jupiter orbit. This phase ends with the energy reduction phase when in orbit around Jupiter. This phase may include flybys of Venus, the Earth, Mars, and the Moon. Various options for this phase are still currently being analyzed and studied, departures up until 2025 are being considered. This phase is separated from the rest of the mission. It is assumed that every option will lead to the same DeltaV for the NSP and ESP.

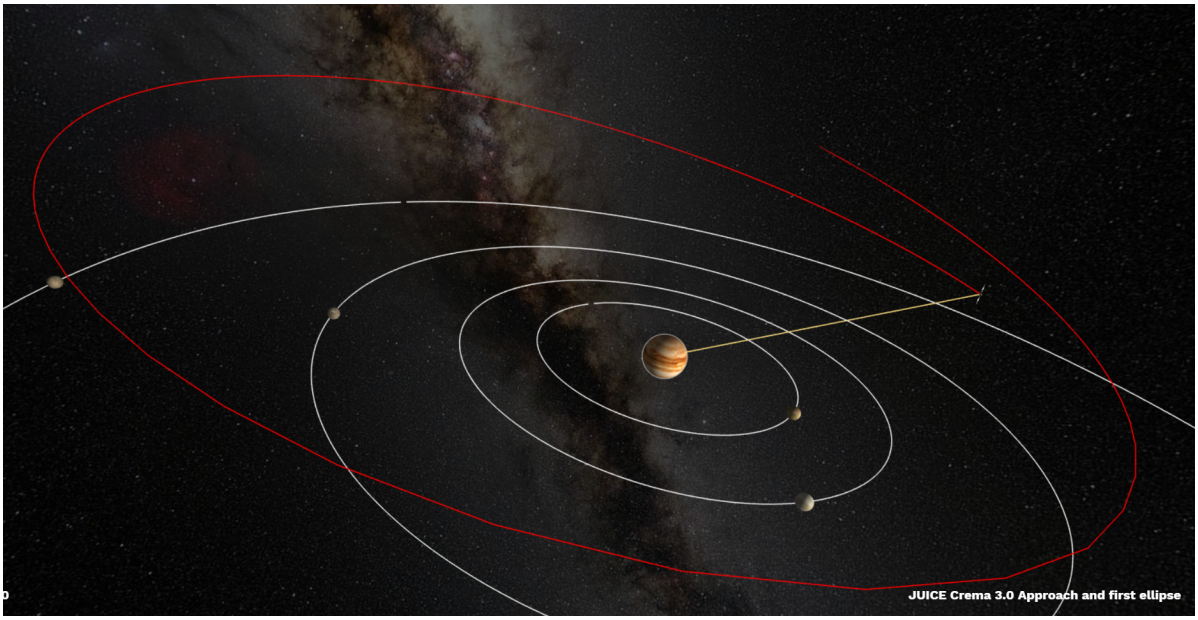

Figure 2.6: JUICE's insertion in orbit around Jupiter with Ganymede gravity assist

Before S/C insertion in orbit around Jupiter, a Ganymede gravity assist will take place that will facilitate the capture process.

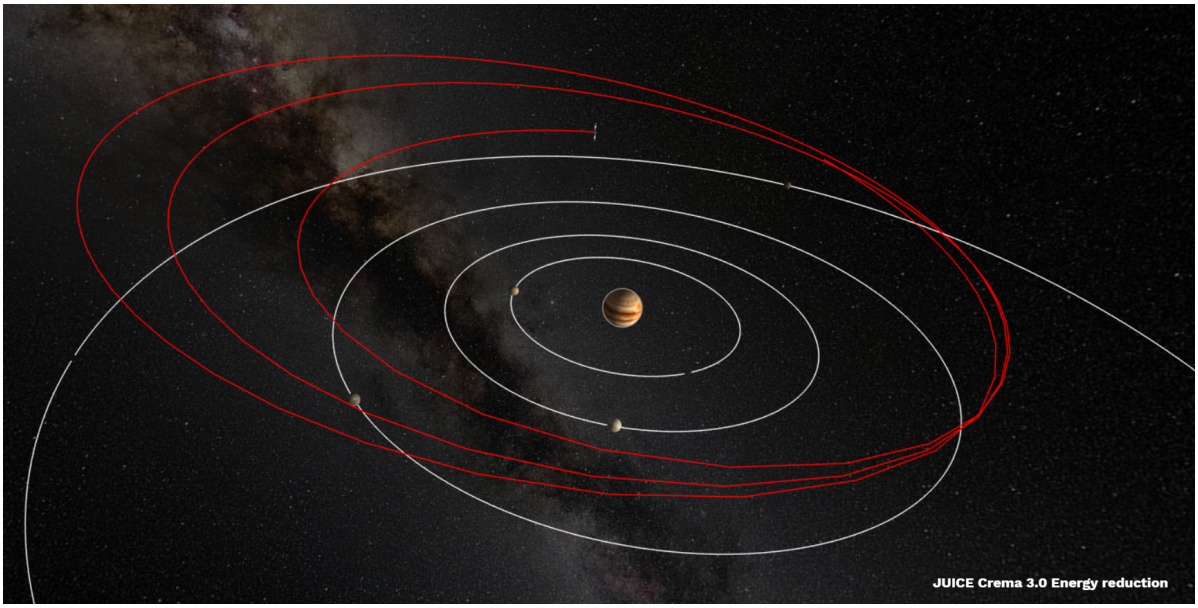

Figure 2.7: JUICE's energy reduction for orbit around Jupiter

After capture, the energy of the S/C is reduced over several orbits.

Nominal Science Phase

1. *Europa flybys*

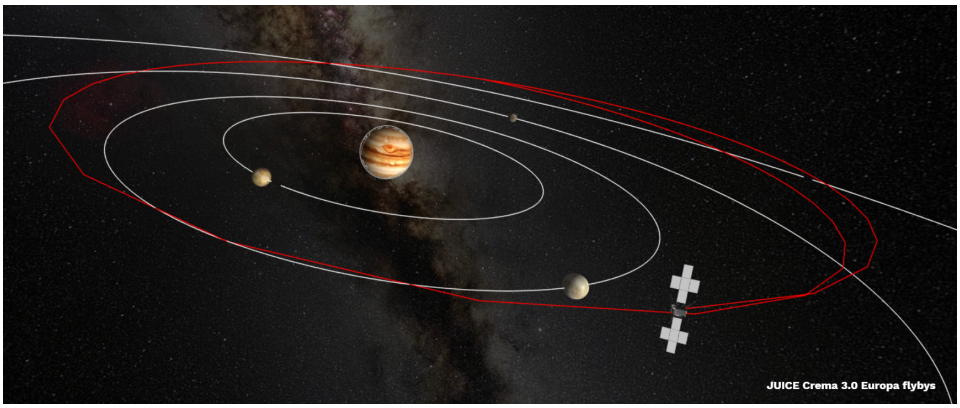

Figure 2.8: JUICE's second flyby of Europa

The next step is the Europa phase, which consists of only two flybys of Europa in the daylight of the target area, the amount of radiation is therefore kept at a minimum while the scientific goals can still be reached.

2. *Jupiter high inclination and Callisto flybys*

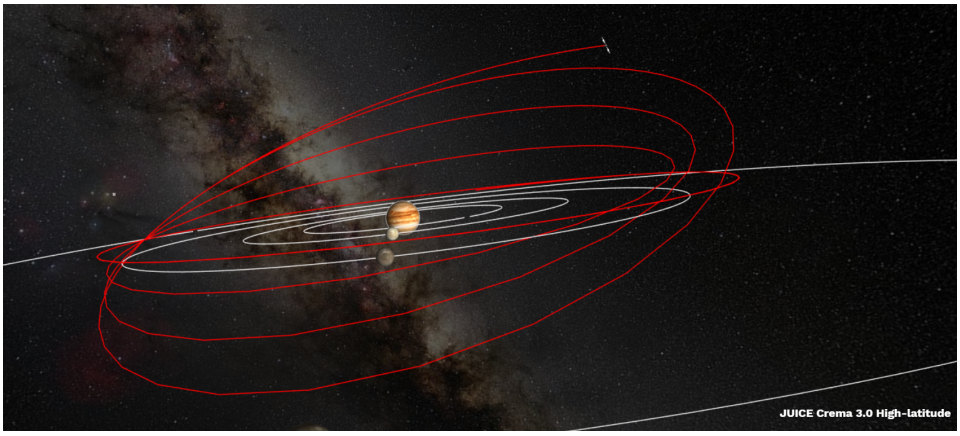

Figure 2.9: JUICE's high inclination orbit around Jupiter

Then, the inclination of the orbital plane is increased using resonant gravity assists, probably using Callisto flybys. This is followed by a DVGA using Ganymede. After three months at a 29-degree inclination, the inclination of the orbital plane is reduced back to allow for the transfer to Ganymede.

3. *Transfer to Ganymede*

   The final goal for JUICE is to reach an orbit around Ganymede. To reach this orbit, the infinite velocity w.r.t. Ganymede is reduced through two actions.

   - First, the so-called Standard Ganymede-Callisto Ladder is used. This consists of making several gravity assists with Ganymede and Callisto, in a sequence GGGCC. This will, in addition to reducing the infinite velocity, allow for a change of the argument of perijove.
   - The second action is the Low Energy Endgame, which consists of successive moon flybys separated by resonant transfers. This approach was chosen because it spares the most DeltaV.

4. *Ganymede orbits* This phase follows after the Ganymede orbit insertion. During this phase, two kinds of orbits will be used.

   - First, the S/C will be put in an elliptical orbit called GEO for 150 days. For this orbit, the apoapsis will be at a distance of 10000km of the center of mass and the periapsis will be at a distance of 200km. As the apoapsis is relatively high, this orbit is highly influenced by third-body perturbations from Jupiter. These perturbations will first lead to a reduction of the ellipticity of the orbit during three weeks to a near-circular orbit with a radius around 4500km. This near-circular orbit will hold for around 15 weeks, after which, the orbit will go back to an elliptical orbit for about three weeks. This phase will mainly be used to study the magnetosphere and build a regional mapping of Ganymede.
   - After the final three-weeks elliptical orbit, the S/C will enter its final orbit GCO-500, a circular orbit of 500 km radius, tailored to require little station-keeping manoeuvers. This phase main-goal is to produce a global mapping of the moon from a low altitude, in conjunction with a study of the interior of the moon.

Extended Science Phase

Once the nominal science phase is over, the S/C will start its extended science phase. During this phase, the S/C has two options. It can perform an uncontrolled impact on Ganymede. This would mean that the S/C's trajectory would naturally evolve to an impact, without outside manoeuvring. Another approach is the controlled impact; for this approach, a de-orbiting procedure is followed by the S/C so that its trajectory's pericenter allows for impact with Ganymede. Two main issues can be noted here, as the ship is getting to the end of its lifetime, its thrusters' performances might be hard to predict and result in not enough DeltaV being produced leading to an uncontrolled crash. Also, if the entire tank is emptied to ensure enough DeltaV is produced, the impact becomes very safe but unpredictable.

2.2.2. Selected opportunities

To come up with initial propositions for operational scenarios, the science team dedicated to the MAJIS instruments had to take into account several constraints:

- Feasibility with respect to the MAJIS instrument and the satellite pointing requirements.
- Compatibility with power and D/L requirements
- Compatibility with shared time allocation (for every instrument)

Thus began an iterative process of development of the operational scenarios. Each round of analysis leads to an incremental increase in the description of the details of the mission.

Overall, three types of observation will be used. Minor bodies, Io and the rings of Jupiter will fall under the distant observations category. Europa, Ganymede, and Callisto will all have flyby observations. Ganymede will also be observed from orbit. These different type of observations will lead to differences in MAJIS resolutions, from 100 km/pix to 100 m/pix.

During the MSc thesis, the research work will mainly be focused on the GCO-500 and the flybys of Ganymede.

2.3. Scientific objectives

This section will describe the scientific objectives necessary to the fulfillment of the blueprint described in the first section. The following section will detail the objectives of the MAJIS instrument for the three icy moons. Finally, some possible synergies between MAJIS and other instruments will be presented.

2.3.1. General

This section is based on the description of the science objectives of JUICE made in [41]. The scientific objectives are divided into the two categories defined by the blueprint.

Habitability of Ganymede, Callisto, and Europa

1. *Ganymede*

   For Ganymede, in addition to its habitability, the focus was put on its planetary features.

   - The existence of a subsurface ocean on Ganymede was suggested by the observations made during the Galileo mission. The JUICE mission objective is to confirm and characterize more accurately the ocean's depth, composition, conductivity, and interactions with the interior and icy shell.

     In addition to this, JUICE shall provide a better understanding of the interior's planetary differentiation. The current gravitational model and its dependency on the tidal interactions will have to be better characterized.
   - To better understand the status and history of the hydrosphere of the moons of the Jupiter system, JUICE will also investigate the icy shell of Ganymede, its chemistry, physical properties, and interactions with the subsurface ocean.
   - The auroras observed on Ganymede are a strong visual cue to the interactions taking place between the magnetospheres of Ganymede and the Jovian system. One objective of JUICE is to characterize the magnetic and electric environment, to help better understand the structure of the subsurface ocean.

     The exospheres of the satellites will also be characterized. This will help with the understanding of the sputtering and sublimation processes which are at the origin of the icy moons' atmospheres.
   - Ganymede's surface is a testimony to a wide variety of processes: ancient and recent impacts (the most diverse of any body in the Solar System), tectonism, cryovolcanism or slow space weathering. JUICE will characterize the features of the surface of Ganymede to provide a better understanding of these processes for all icy satellites in the outer Solar System.

     To have a better overview of the geology of Ganymede, a high spatial resolution and extensive coverage of the surface will be necessary.

- The Galileo mission, corroborated by ground-based data, has shown that several non-water ice components can be found on the surface of Ganymede. However, the exact composition and distribution are unknown and will have to be investigated by JUICE, through high spatial resolution and SNR. This knowledge would help better understand the history of Ganymede's surface, internal processes, and external interactions.

2. *Europa*

- Similarly to Ganymede, the presence of non-water components in Europa's ice has been suggested by the Galileo mission. JUICE will characterize the composition of the surface. Specifically, hydrated compounds have been spotted and will have to be thoroughly investigated. Therefore, JUICE will also have to be able to have high spatial resolution and SNR on Europa.
- The Galileo and Voyager missions' observations have shown that a subsurface water ocean was present on Europa. This ocean will be investigated to characterize its depth, composition, and interaction with the interior and surface ice shell of Europa.

  Special care will be given to the observation of the most currently active regions of Europa, to better describe the exchange processes between the ocean and the ice surface and to estimate the thickness of the ice shell in these regions.
- As there are few craters at the surface of Europa, it has been deduced that the surface is relatively young. Furthermore, the feature spotted on its surface could be characteristic of tectonism, cryovolcanism or diapirism.

  O_2 has been detected as a primary component of Europa's atmosphere. This O_2 could also be present in the subsurface ocean, which would give favorable conditions for the apparition of life.

  There is a lack of data on the presence of outgassing or plumes at Europa. The observation of plumes at Enceladus has led to a better understanding of the chemistry and interactions taking place. JUICE will, therefore, try to identify these types of activities on Europa.

  Overall, any recent active processes in the atmosphere, surface, and ionosphere of Europa is a feature of interest for JUICE.

3. *Callisto*

- Unlike Europa, Callisto's surface is ancient and does not show any active processes. This would be indicative of the absence of internal dynamics. However, Galileo's data has suggested that below the ice shell, a subsurface ocean could be present. JUICE will, therefore, characterize both the subsurface ice shell and the internal ocean.

  JUICE will make observations of the surface features of this moon and link them with the subsurface icy shell observations. The current gravity field model will also be improved by the measurements, which will give insight into the interior and the differentiation of the planet. JUICE's measurements of the induced magnetic field and the time dependency of the second-degree gravity field will help characterize the subsurface ocean.
- Various non-water compounds are present on the surface and in the atmosphere of Callisto. JUICE will characterize both the compounds present on Callisto's surface to better understand the local geology, and the compounds in the atmosphere to help identify any asymmetrical releases.
- As mentioned previously, Callisto's surface is ancient and covered in dark crater-abundant plains. The surface has features characteristic of significant erosion and degradation. Because of its relatively minimal evolution, Callisto's observations can be used to get insight into the history of the early Jupiter system.

  JUICE will estimate the age of the surface of Callisto and explore the erosion and deposition that took place. Also, global observations will help investigate the planetary differentiation of Callisto.

The Jupiter system as an archetype of gas giants

1. *Jovian Atmosphere*

- Exploring a gas giant such as Jupiter can give insight into the many gas giants exoplanets that have been observed and into the processes dictating the reactions in planetary atmospheres. JUICE

will investigate the processes that take place in the atmosphere, responsible for the mixing of momentum and material. For this purpose, high duration measurements over a wide range of wavelengths will be taken. JUICE will observe the atmosphere of Jupiter from the troposphere to the upper thermosphere, linking these observations to the deep interior and the external environment.

- Heavy molecules are present in minority in Jupiter's atmospheres. These molecules can lead to a better understanding of the history of the nebula material that helped form the gas giants in the Solar System.

  JUICE will investigate the distribution and variability of stratospheric hydrocarbons, the origins and distribution of exogenic species, localized and non-equilibrium compounds in the troposphere, and the spatial distribution of volatiles.

  These measurements will respectively help get a better understanding of the chemistry of the middle atmosphere and troposphere; constrain external sources of material; the processes that lead to cloud formation.

  In the polar regions of Jupiter, the chemistry of tropospheric clouds at high latitudes and the thermospheric auroras will be studied by JUICE.

- The vertical structure of Jupiter is not well-understood. The processes governing it, which are linked to external sources (the Sun, the moons, ...) and internal sources (from the deep interior to the upper atmosphere), will be characterized by JUICE, thanks to the long observational times allocated.

  An accompanying study of the chemistry of the cloud forming in the troposphere will be performed. This will help gain insight into the processes leading to cloud formation on gas giants.

2. *Jovian Magnetosphere*

- The inner magnetosphere of Jupiter is home to the synchrotron radiation belt, the primary plasma sources (Europa and Io), a neutral and a plasma torus, and a magnetodisc. In the middle magnetosphere, the magnetic field contains the plasma. In the outer magnetosphere, the magnetopause's distance to Jupiter is variable, depending on the Sun's relative position and other environmental conditions.

  JUICE will explore the magnetosphere at high latitudes and between Ganymede and Europa. JUICE will also focus on Jupiter's magnetodisc.

- The corotation of the plasma highly influences the magnetosphere. Three processes are of key interest to JUICE. First, the transport of matter liberated from Io both outward and inward. Secondly, the injection of particles in the middle magnetosphere from hot plasma to cold plasma. Thirdly, the acceleration of matter along the connection of magnetic field lines.

  These processes and other transport processes will be investigated by JUICE to develop our understanding of these interactions further.

- Exchange processes between the magnetosphere and the moons' surfaces will be explored by JUICE. These can lead to resurfacing processes that are key to the interpretation of JUICE's surface observations.

  JUICE will also monitor the particles in the neighbourhood of Ganymede and Callisto and the exchange processes with Jupiter's magnetosphere. The history of the atmospheres of the icy satellites will be explored. For its volcanism and to characterize the composition of its surface, Io will also be investigated by JUICE.

3. *Jupiter System*

- Due to the heavy tidal forces acting on it, Io is the most volcanically active body in the Solar System. Eruption durations are very varied. They can be short as well as many years long.

  The presence of water on Io is very marginal if there at all. Many surface species and Fe-bearing salts and silicates are present on its surface. JUICE will investigate the volcanism and surface composition of Io.

- JUICE will explore both the mapping and composition of the ring system of Jupiter. Inside the ring system, the small satellites of Jupiter will also be studied. Their shape and composition will

be investigated. The orbital elements and the interactions with the ring system of the two main satellites (Thebe and Amalthea) will also be characterized. Finally, to account for the fact that they can exchange matter with the giant satellites, the composition of at least one irregular satellite will be studied.

2.3.2. MAJIS objectives for the selected opportunities

In this section, the objectives assigned to the MAJIS instrument with respect to the icy satellites are summarized.

Ganymede

1. *Characterization of the ice shell*

   - Make comparisons between surface characteristics and subsurface aspects to explore the interactions taking place in the interior and near the surface.

     For these purposes, MAJIS will take measurements of the reflectance at the surface of Ganymede in the VIS-NIR and IR range with a spatial resolution of at least 125 m / pixel. The spectral resolution shall at least be 5nm in the VIS-NIR range and 10 nm in the IR range. This will allow for the distinction between sulfuric acid hydrate and Magnesium and Sodium enriched salt hydrates.

     (When not mentioned, the spectral resolution goal is to reach at least 5nm in the VIS-NIR range and 10 nm in the IR range.)

2. *Characterization of Ganymede's environment and its exchanges with the magnetosphere of Jupiter*

   - Explore the origin of aurorae on Ganymede.

     MAJIS will take images in the VIS-NIR and IR range of the aurorae, with a spatial resolution better than 1 km / pixel and a temporal resolution of 1 min.

   - Investigate the exact sources and sinks of both the ionosphere and exosphere of Ganymede

     MAJIS will take images in the VIS-NIR and IR wavelengths of the atmosphere of Ganymede. This shall provide information on the species present in the atmosphere and their densities at a spatial resolution of at least 1 km / pixel. For this objective, it is expected that observations will be performed for a long period with high temporal resolution, to allow to relate observations with magnetospheric variations. These measurements will help determine the composition of the atmosphere and, specifically, whether the presence of water ice, O2, O3, H2O2, carbon dioxide ices can be confirmed. In addition to this, the use of stellar occultation allows exploring the absorption and emission of species present in the atmosphere of Ganymede. The stellar occultation is performed in the IR range with limb sounding about 5 km from the surface.

3. *Investigate the history and formation of surface features*

   - Estimate the age of the surface on a global and regional scale

     Surface images at high resolution will be captured in both the VIS-NIR and IR wavelengths with medium spatial resolution (2.5-10 km / pixel) on a larger scale to allow for the spotting of any asymmetry or exogenic species.

   - Explore the erosion of the surface and its consequences on the properties of the surface.

     Take images in the IR wavelengths with a spectral resolution of at least 5 nm to allow for the characterization of several water ice bands, hydrated salts and sulfuric acid hydrate at a high spatial resolution.

4. *Investigate the history and chemistry of surface materials on various scales*

   - Explore the presence of organic and inorganic material on the surface

     Measurements in both the VIS-NIR and IR wavelengths will be taken at spatial scales ranging from 5 km / pixel to at least 1 km / pixel. The coverage of the surface shall be greater than 50 % at a resolution higher than 3 km / pixel.

     Characterize the global chemistry and material distribution of the surface on a global scale using various scales of spatial resolution from 10 km / pixel to 100 m / pixel and various illumination conditions.

- Explore the links between the geology of the surface and its composition

  Explore the presence of species indicative of weathering effects from the magnetosphere in the VIS-NIR wavelengths. Investigate the distribution of the states of water ice depending on the locations and the local albedos. At least a 50% coverage should be reached with resolutions higher than 3 km / pixel.

- Characterize the distribution of volatiles on the surface and relate it to the history of the satellite

  Characterize the presence of non-water-ice materials, specifically to identify the presence of volatiles on the surface, by taking images in the VIS-NIR and IR wavelengths at spatial scales ranging from 5 km / pixel to at least 1 km / pixel. At least a 50% coverage should be reached with resolution higher than 3 km / pixel.

Europa

1. *Investigate the chemistry of material other than water ice that could indicate the habitability of the moon*

   - Make comparisons between surface characteristics and subsurface aspects to explore the interactions taking place in the interior and near the surface.

     This objective is completed using the same method as for Ganymede, repeated here below:

     MAJIS will take measurements of the reflectance at the surface of Europa in the VIS-NIR and IR range with a spatial resolution of at least 125 m / pixel. The spectral resolution shall at least be 5nm in the VIS-NIR range and 10 nm in the IR range. Some pre-selected sites of scientific interest will be explored using a high spatial resolution between 100 m and 1 km / pixel.

2. *Characterization of Europa's environment and its exchanges with the magnetosphere of Jupiter*

   - Investigate the presence of surface organic and inorganic species. Relate the observations made to the potential habitability and bio-signatures of Europa.

     For these objectives, the MAJIS measurements of the reflectance at the surface of Europa's dayside will also be used.

   - Explore the links between the chemistry of the surface and the observed local geology. Special interest is given to the interaction with material from the interior of Europa.

     For these objectives, the MAJIS measurements of the reflectance at the surface of Europa's dayside will also be used.

   - Determine the chemistry of the species sputtered from the surface.

     For these objectives, the MAJIS measurements of the reflectance at the surface of Europa's dayside will also be used.

3. *Characterize the currently active processes*

   - Investigate the active processes visible at the edge of the apparent disk of Europa

     MAJIS will scan Europa starting 5 km up, down to the surface in the VIS-NIR and IR wavelengths. These measurements will help determine the species present in the atmosphere of Europa, specifically whether O2, H2O, and CO2 can be identified.

   - Compare the surface observations to the data from the Galileo mission.

     For these objectives, the MAJIS measurements of the reflectance at the surface of Europa's dayside will also be used.

Callisto

1. *Investigate the chemistry of material other than water ice*

   - Investigate the presence of surface organic and inorganic species.

     Investigate the composition and chemistry of surface species and volatile materials using imaging in the VIS-NIR and IR wavelengths with various scales of spatial resolution from 10 km / pixel to 100 m / pixel and various illumination conditions.

     Relate the observations of non-water-ice materials to the geological history and current activities of the surface.

- Investigate the links between the surface chemistry and geology to the magnetospheric activities.
  MAJIS will take measurements of the reflectance at the surface of Callisto in the VIS-NIR and IR range. The spectral resolution shall at least be 5nm in the VIS-NIR range and 10 nm in the IR range. Relate these measurements to the geological activities and the effects of weathering. Also, investigate the presence of species indicative of the radiolysis and ion bombardment.
- Explore the ionosphere and exosphere of Ganymede
  MAJIS will take images in the VIS-NIR and IR wavelengths of the atmosphere of Ganymede. This shall provide information on the species present in the atmosphere and their densities. This would entail either taking images at a spatial resolution of at least 1 km / pixel or the use of stellar occultation on the atmosphere of Callisto. The stellar occultation is performed in the IR range with limb sounding starting 300 km up down to the surface by steps of 5 km.
  Global images will also be taken with a spatial resolution of at least 50 km / pixel.
  These measurements will help determine the composition of the atmosphere.

2. *Investigate the history of Callisto*

- Explore the tectonics and impacts of Callisto
  For these objectives, the MAJIS measurements of the reflectance at the surface of Europa's dayside will also be used.
  Some pre-selected sites of high geologic interest will be explored using a high spatial resolution.
- Estimate the age of the surface on a global and regional scale
  Surface images will be captured in both the VIS-NIR and IR wavelengths with high spatial resolution (at least 1 km / pixel) to allow for the distinction of important geological features.

2.4. Conclusion

In this chapter, the context surrounding the JUICE mission and the MAJIS instrument was described. First, the background of the JUICE mission from a historical and general point of view was described. Then, the trajectory that the spacecraft is expected to take was detailed. Finally, the scientific objectives of JUICE and MAJIS were summarized.

The JUICE mission directly stems from the observations of previous missions which explored the Jupiter system. As part of the Cosmic Vision program, the JUICE mission's objectives revolve around the conditions for the emergence of life. The habitability of Ganymede, Europa, and Callisto is one of the main topics of interest to this mission. Therefore, the JUICE instruments were designed to also reach these scientific objectives. The MAJIS measurements will help investigate various aspects of scientific interest. One of the consequences of the variety of observations that will be required from MAJIS is that much flexibility will be required and, therefore, a lot of operational modes will be tested in the characterization of the instrument.

3

MAJIS Technical description and performances

The MAJIS instrument will be the VIS-NIR and IR spectrometer aboard the JUICE mission [29]. The performances of the instrument will delimit the available scientific prospects in-flight.

In this chapter, the way the MAJIS instrument will operate is presented. As the instrument is still in development, some of the aspects presented in this chapter may be subject to change in the future.

First, a description of the instrument will be given. Then, the specificities of the operation of MAJIS are detailed. This includes the range of operating temperatures, the acquisition mode, and the image acquisition procedures. Following this, the resources necessary for the functioning of the MAJIS instruments are described. Next, the de-spiking procedure used to mitigate the effect of cosmic rays is summarized. Finally, an analysis of a concrete case is introduced in the scope of the scientific objectives of MAJIS.

3.1. Instrument description

MAJIS is an imaging spectrometer, made of a double channel Czerny-Turner imaging spectrometer able to operate in both the VIS-NIR (0.5 – 2.35 µm) and MW-IR range (2.25 – 5.54 µm). The control of MAJIS FPAs is done through their respective FPEs.

A French-Italian consortium is building the MAJIS instrument. The two funding agencies are CNES and ASI, with CNES being the leading agency. The prime contractor of the instrument is IAS. Its responsibilities w.r.t. MAJIS include the OH and Main Electronics final integration, testing and calibration, the FPAs, and the MW-IR channel filter.

The main components of the MAJIS instrument are described in the figure below (IR corresponds sto MW-IR) (JUI-IAS-MAJ-RS-021):

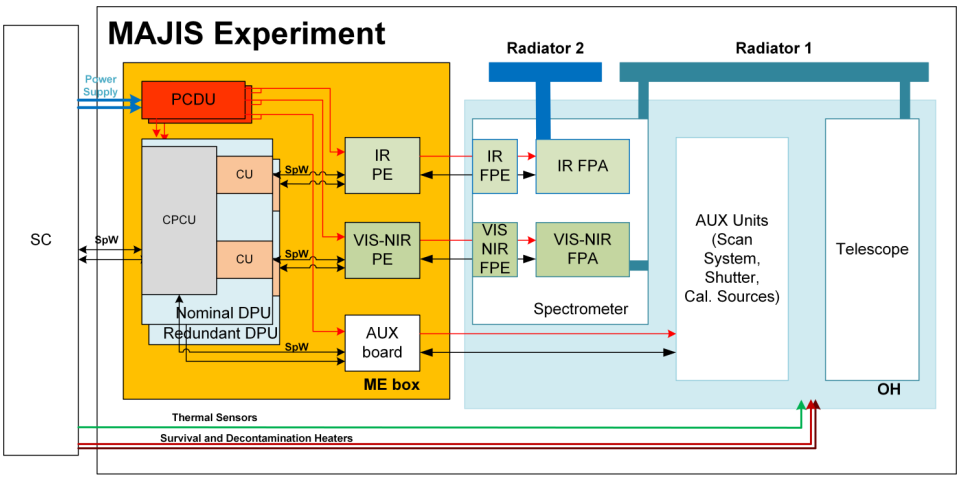

Figure 3.1: MAJIS block diagram

Both channels of the MAJIS instrument use the same telescope. The expected FOV and IFOV of MAJIS are respectively 3.4° and 150 µrad without spatial binning. After the telescope, a dichroic window is used to feed both the VIS-NIR and MW-IR channels of the spectrometer.

The two FPAs for both channels are H1RG detectors provided by Teledyne. These detectors are described in more detail in the following chapter. The pixels of these 1024x1024 detectors are typically binned two by two resulting in a 512x512 array of 36 × 36 µm pixels. For instance, in the main phase GCO-500, this corresponds to a 30 km wide region coverage with a 75 m / pixel maximum spatial resolution, which can be adapted by binning if the observational conditions require it. The spectral sampling is done over 508 spectels (4 of the 512 spectels are not light-sensitive, reference pixels, and are present on each side of the detector). For the VIS-NIR channel, the sampling is 3.65 nm / band, and for the IR channel, it is 6.49 nm / band.

Both detectors are connected to their respective Focal Plane Electronics (FPE), which allows to control and read the video signals produced by the detectors.

A shutter is present in front of the detectors to allow for the capture of dark current frames that will be subtracted to the scientific target frames during their analysis.

The instrument will also use two internal calibration units located inside the OH to allow for calibration while in-flight. These units use different types of light sources. A filament lamp is used for the VIS-NIR and a black body for the IR.

The main features of the MAJIS optical design are reported in the following table:

Parameter	Value	Remarks
Aperture	56 mm spectrum x 85 mm space	
Aperture equiv. diameter	75 mm	
Telescope focal length	240 mm	
IFOV	150 µrad	
Spectral range VIS-NIR	0.5 – 2.35 µm	
Spectral range IR	2.25 – 5.54 µm	
Pixel size	36 µm	
Number of pixels	400	Both channels
Number of spectels	508	Both channels

Table 3.1: MAJIS optical design features

3.2. Temperature

The lower the FPAs' temperatures are, the better the performances of the instrument will be (see Section 4.5). For instance, the JWST, which uses the same brand of detectors, will have most of its instruments operating under 40K [28]. In an ideal scenario, such temperatures would improve the overall performances of the MAJIS instrument and increase the possible scientific returns.

To reach this kind of temperatures, the JWST satellite uses a very large sunshield (about 300 m^2 [28]). This sunshield will protect the spacecraft from the heat radiated by the Sun [1]. Because of this protection, the JWST instruments' temperatures can be maintained below 40K using passive cooling only [1].

This kind of solution was not feasible for the JUICE spacecraft. The JWST cost is about 10 times the cost of the JUICE mission and the JUICE mission will be sent much farther. As JWST, JUICE will use passive cooling for the MAJIS instrument. However, due to the absence of the sunshield, the temperatures that can be reached will be significantly higher.

Due to the overall budget limits, mass limits, and power consumptions limits the higher temperature had to be put up with.

Two radiators (cold and warm) are used for the thermal control of the MAJIS instrument. The cold radiator allows the MW-IR HxRG detector to reach its operating temperature (<90K). The warm radiator is used to regulate both the Optical Head (OH) and the VIS-NIR detector around 140K.

The higher operating temperatures will induce new original challenges for the MAJIS instrument. This reinforces the importance of the characterization of the detectors' performances.

3.3. Acquisition mode - Microcode

The microcode is used to program the type of acquisitions made by the HxRG FPAs. Two microcodes have been developed for the MAJIS mission, corresponding to two acquisition modes.

The two acquisition modes that exist both correspond to different pixels reading speeds. One of the advantages of having multiple available acquisition modes on a detector is that it allows more flexibility on the observations that can be made.

The brightness of the object being observed will influence the acquisition modes used:

- Using an acquisition mode with a higher reading speed allows for the observation of brighter objects without the pixels being saturated by the time they are read (lower minimum integration time). This is a key aspect of the MAJIS observations. Due to the highly radiative environment and the spacecraft trajectories, some observations can be made only using integration times of the order of 100ms.
- Using a slower acquisition mode (when the object is dimmer) leads to less power being used and better read-out noises.

The microcodes have different options to adjust the operation of the detectors. A number of biases can be modified. These biases will lead to different performances on different detectors. They will have to be optimized for the detectors used on MAJIS specifically.

An important option for the acquisition of images is the windowing option. The windowing option will allow reading only a specific number of rows of the detector. (e.g. instead of reading the 1024 rows of the full-frame, only 200 rows starting at the row 400 can be read (i.e. rows 400 to 599)).

The conversion time of a frame is the time it takes the detector to read the whole frame. The conversion time depends on the acquisition mode. The integration time represents the duration during which photons are acquired. The integration time has a lower limit (conversion time). As images are acquired row after row, the lower limit depends not only on the acquisition mode but also on the number of rows used for the image. For a full-frame image (1024 rows) the conversion times are 74 ms for the Fast acquisition mode and 740 ms for the Slow 100kHz acquisition mode.

In addition to the operating temperature bringing new challenges, the integration times will also be very different from most astronomical observations made with these detectors. Usually, these detectors are used in a ramp mode with long acquisition times. Due to the high flux, the instruments will receive from Jupiter and its icy moons, the duration of the acquisition will be shorter (< 1 sec).

3.4. Image acquisition

The nominal 2D acquisitions of the FPAs consist of 400 pixels (36 µm pixel) in the spatial direction and 508 spectels (36 µm spectel) in the spectral direction. Both channels are designed to operate at the same time to acquire data over the entire spectral range simultaneously. If necessary, windowing can be used (see Section 3.3).

The full data acquisition is presented in the form of 3D data cubes where the last dimension represents the repetition of consecutive IFOV step acquisitions.

MAJIS can use several operation modes to adapt to the movement of the spacecraft with respect to the target. Some essential aspects used by MAJIS are:

- *Pushbroom*

  In this mode, the scanning mirrors do not move from their initial position, while the spacecraft follows its trajectory. The repetition time is chosen based on the time taken for the sub-spacecraft position to move by one IFOV.

- *Scanning*

  When using this mode, the mirrors are used to modify dwell times. They can be too long when the sub-spacecraft velocity is too low, or too short when the velocity is too high. For instance, during GCO-500, the motion of the spacecraft might be too fast for high resolution because the target is so close and require to be compensated by the scanning mode.

3.5. MAJIS resources

The technical budget management of the instrument is fundamental to achieve all requirements necessary for the good functioning of the JUICE spacecraft (JUI-IAS-MAJ-RD-007).

Several aspects were taken into account in the budget management, including (JUI-IAS-MAJ-RD-007):

- mass budget,

- power budget,
- data-volume budget,
- thermal budget,
- CPU load budget,
- radiation budget...

The main relevant aspects for the characterization of the detectors are the data-volume, power budget, thermal budget (see Section 3.2), and radiation budget (see Section 3.6).

3.5.1. Data-volume

One of the main resources that will have to be managed during the mission is data-volume. An essential part of the mission planning is to assign to each instrument of JUICE specific data volumes that they will be able to transmit. This implies that the data-volume produced by the instrument has to be estimated and compared to the expected available data-volume that can be sent out to the ground.

The MAJIS observations will use both channels of the instrument producing two types of acquisitions, one for the VIS-NIR range and one for the IR range. Both nominal acquisitions are 400 pixels by 508 spectels. A compression algorithm will be applied to these 16 bits per data elements acquisitions resulting in 5 bits data. However, when measuring for specific acquisitions, binning, spectral editing, and re-sampling might occur and have to be taken into account.

Another critical aspect of data volume management is the optimization aspect w.r.t. the scientific goals (i.e. reach the scientific goals described in the previous chapter while using the least resources possible). Some of the operation modes that will be available in-flight are:

- Pixel binning along rows and columns,
- Reducing the number of pixels in the spatial direction by windowing (400 nominally),
- Reducing the number of spectels to target specific wavelengths (508 nominally),
- Increasing the number of spectels for better spectral resolution up to 640 spectels.

Due to the critical aspect of the observation of Ganymede, it has been decided that the mass memory of JUICE should be empty before inserting into orbit around Ganymede. The data volume analysis performed by the JUICE team will, therefore, be separated between both parts of the mission.

To compute the data volume, the compression and formatting of the data elements need to be taken into account. Each basic data element is 16 bits. This is based on the acquisitions of the HxRG detector. 16 bits is sufficient to sample the full signal dynamics.

3.5.2. Electric power

The electric power budget has to be done not to exceed the power resources made available by the spacecraft. Several parts of the MAJIS instruments require power to function properly. Furthermore, depending on how the instrument is used, the power consumption will vary.

The modes which will consume the most energy are the calibration mode (due to the light sources) and the science mode. Although the calibration mode consumes significantly more power, calibration can be performed outside of the zones of critical scientific importance.

3.6. Despiking procedure

(This section is based on an internal report of the MAJIS team, reference JUI-IAS-MAJ-TN-022)

A central aspect of the MAJIS instrument is the de-spiking procedure that will be followed. Its goal is to reduce the impact of cosmic rays on the detectors. This procedure aims at a maximum of 1% of pixels still affected by spikes after de-spiking. This limit was adopted to be on the same level as the expected non-operability (see Section 5.9) of the flight detectors. Therefore, the overall science impact of the cosmic rays would be limited.

The de-spiking strategy is highly dependent on the integration times used by the detector to perform acquisitions. Because of the availability of 2 read-out modes (see Section 3.3) the integration times can go as

low as 0.056 s using the 1 MHz and as low as 0.560 s using the 100 kHz (800 rows). Depending on the target observed, the available integration times can vary based on the radiance of the object. For that reason, in the IR range (2.25 - 5.53 µm), according to the latest version of the radiometric model, Jupiter's hot-spots can only be observed with integration times around 0.1 s before the detector reaches saturation. Whereas icy-satellites have maximum integration times of around 0.8 s. (In the VIS-NIR Europa has the highest radiance. To adapt to this, the acquisition and de-spiking strategies can be different for the VIS-NIR and IR channels.)

To meet the science requirements, the observations times range between 0.5 s to > 8 s. The MAJIS instrument will take multiple sub-frames of the same target. This will avoid saturation and, as further explained below, also provide samples for the de-spiking procedure.

Even though a radiation shielding protects the detector, the highly radiative environment around Jupiter will still have an impact on the detector. Two series of tests were conducted simulating the Jupiter environment to estimate the number of spikes that could be expected on the detectors during the science phase. The conclusions of these tests showed that in the worst part of the radiation environment of Jupiter, (during the fly-bys of Europa) it is expected that as much as 2.56 high energy electrons/s can reach the detector's binned 36 × 36 µm pixels [18].

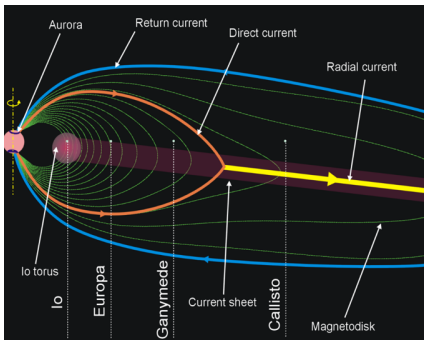

Figure 3.2: Radiative environment around Jupiter [11]

It can be noted that the probability of these spikes significantly decreases the further away from Jupiter the satellite is. In orbit around Ganymede, it is expected that the rate of spikes will be around 0.1 high energy electrons/s/pixel. The impact of these high energy electrons ranges from less than 1% of FWC up to > 10% of FWC. This showcases the extreme importance of the de-spiking procedure for the science return of the mission, especially around Europa, where no relevant data would be acquired otherwise.

To mitigate the impact of these radiations on the scientific quality of the data acquired by MAJIS, the de-spiking procedure is applied. The procedure proposed for the MAJIS instrument is to always divide an acquisition into N sub-frames. Even if the detector is not expected to saturate. The strategy, then, consists in taking for each pixel the average of a given number M (M ≤ N-1), of the lowest values out of the N sub-frames. This procedure makes it most likely to avoid taking values that have been impacted by a spike.

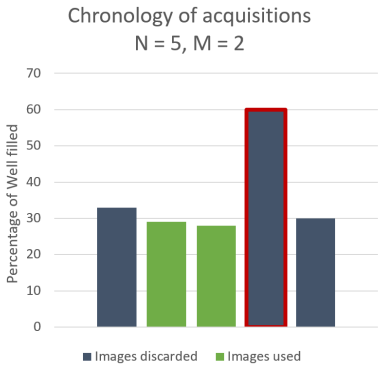

Figure 3.3: De-spiking example for N=5 and M=2

However, it should be noted that using this approach will create a slight negative bias in the observations as the lowest value will always be the one retained. This bias will be evaluated and compensated to preserve the data acquired.

This results in the addition of two new parameters that also will have to be transmitted to the acquisition chain on each observation.

- The number N of sub-integrations. Limited to 8 for internal memory reasons (to the FPE, PE).
- The number M of low outcomes to be averaged after sorting (to the PE)

Various settings were evaluated for the mitigation of the spikes depending on the actual cases encountered for the mission. These settings were optimized using a Monte-Carlo approach simulating the effect of spikes. These simulations have shown that the most effective de-spiking strategy is to always act before the binning, directly on the 18 × 18 µm pixels. This results in a target level of 0.25% residual spikes. A level of 0.25% for the 18 × 18 µm pixels will always result in less than 1% residual spikes on binned pixels.

3.7. MAJIS science expectations

3.7.1. MAJIS science summary

The scientific objectives of MAJIS were detailed in Section 2.3.2. The following table gives a summary of the main contribution of MAJIS to the scientific objectives of the mission (the JUICE objectives list is taken from [41]):

Science Objectives		**MAJIS contribution**
Characterise Ganymede as planetary object and possible habitat	Characterise the extent of the ocean and its relation to the deeper interior	Indirect
	Characterise the ice shell	Significant †
	Determine global composition, distribution and evolution of surface materials	Significant †
	Understand the formation of surface features and search for past and present activity	Significant
	Characterise the local environment and its interaction with the Jovian magnetosphere	Small
Explore Europa's recently active zones	Determine the composition of the non-ice material, especially as related to habitability	Significant
	Look for liquid water under the most active sites	Indirect
	Study the recently active processes	Significant
Study Callisto as a remnant of the early Jovian system	Characterise the outer shells, including the ocean	Indirect
	Determine the composition of the non-ice material	Significant
	Study the past activity	Significant
Characterise the Jovian atmosphere	Characterise the atmospheric dynamics and circulation	Significant
	Characterise the atmospheric composition and chemistry	Significant
	Characterise the atmospheric vertical structure	Significant
Explore the Jovian magnetosphere	Characterise the magnetosphere as a fast magnetic rotator	
	Characterise the magnetosphere as a giant accelerator	
	Understand the moons as sources and sinks of magnetospheric plasma	Small
Study the Jovian satellite and ring systems	Study Io's activity and surface composition	Small
	Study the main characteristics of rings and small satellites	Significant

Table 3.2: Contribution of MAJIS to JUICE science objectives

3.7.2. Implications on the specific cases of my thesis

To evaluate the performances of the MAJIS instrument, this thesis will focus on two specific scientific objectives of MAJIS. These objectives are the characterization of water ice and the characterization of organic species on the surface of Ganymede (see † in Table 3.2). The water ice objective will be analyzed based on the identification of the 2.0 µm absorption band. The organic species objective will be analyzed based on the identification of the 3.3 µm absorption band (C-H stretch).

When in GCO-500, MAJIS will perform high-resolution observations of Ganymede. During these high-resolution observations of Ganymede, MAJIS will have some of its lowest levels of SNR. This makes this case particularly critical for the requirements.

The following table gives the performances of the detectors used by the MAJIS team to develop the radiometric model:

IR detector performance parameter	Original assumption	Updated assumption
λ cut-off (50% of peak QE)	5.56 µm	5.62 µm
Dark current (per binned pixel)	7000 e-/sec	2400 e-/sec
Total read noise (per binned pixel) (Slow 100kHz)	40 e-	30 e-
Total read noise (per binned pixel) (Fast)	80 e-	65 e-
FWD (per binned pixel)	160 000 e-	280 000 e-
QE plateau	80 %	90 %

Table 3.3: Summary of assumed IR FPA performances

IR detector performance parameter	Original assumption	Updated assumption
λ cut-off (50% of peak QE)	2.35 µm	2.51 µm
Dark current (per binned pixel)	25 e-/sec	10 e-/sec (FM) 1200 e-/sec (FS)
Total read noise (per binned pixel) (Slow 100kHz)	40 e-	35 e-
Total read noise (per binned pixel) (Fast)	80 e-	65 e-
FWD (per binned pixel)	240 000 e-	372 000 e-
QE plateau	70-80 %	80 %

Table 3.4: Summary of assumed VIS-NIR FPA performances

With a VIS-NIR and IR FPA reaching the performances shown in Table 3.4, SNR analyses of several selected observational cases have been produced by the MAJIS team (JUI-IAS-MAJ-TN-022).

For these selected cases, the radiative environment was taken into account and the de-spiking procedure was optimized to produce the highest SNR levels possible. For Ganymede high-resolution observations, based on the expected number of spikes per second and the total repetition time available for the observations, it was determined that DITs <200ms would be used. This lead to the following SNR levels for Ganymede HR:

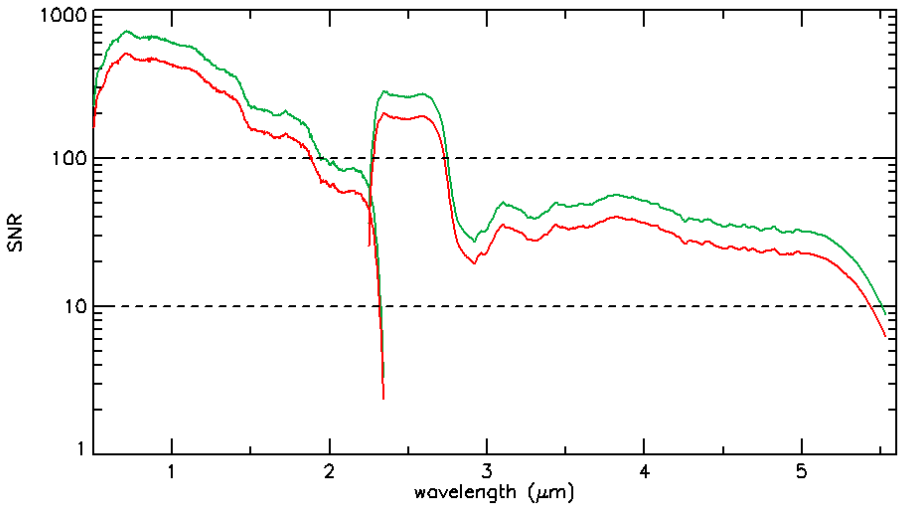

Figure 3.4: SNR for Ganymede HR observations as a function of the wavelength for the IR and VIS-NIR channel of MAJIS

The MAJIS team derived that with the associated SNR, the identification of water ice (2.0 µm) and organic species (3.3 µm, C-H stretch) would be possible on Ganymede HR. If the detectors' performances conform to the performances detailed in Table 3.4 and 3.3, it is expected that the MAJIS instrument will be able to achieve its scientific requirements.

3.8. Conclusion

This chapter summarized the functioning and performances of the MAJIS instrument. There are many factors that will influence the performances of MAJIS, which have to be taken into account to determine the capacities of the instrument in-flight.

When considering resources such as electric power or data volume, it is apparent that the modes of operation and how the software is used will have a substantial impact on the output of MAJIS. As a consequence, ensuring that the scientific goals are reached while minimizing the use of resources will be important for the JUICE mission.

The temperatures and integration times used for the MAJIS detectors will introduce new challenges specific to this mission. The detectors used have not been tested in these conditions before. These aspects have to be taken into account in the methodology of the testing, specifically, it will have a strong impact on the design of the test plan in Section 5.12.

Simulations have been performed for the MAJIS observations. These simulations have shown that for specific detectors' performances it was possible to reach the scientific objectives of MAJIS. The characterization of the detector will help determine whether the assumptions made were legitimate and whether MAJIS can reach its objectives.

It is particularly important to note, that due to the extreme environment, the conditions in which the detectors will be, will vary significantly. The characterization should test whether the detectors can reach satisfying levels of performance in all expected conditions.

4

Physics of IR detectors

Understanding the fundamentals of IR detectors is helpful to put a context around the characterization of the detectors. The characterization will use several performance parameters. The description of the physical phenomena at the origin of these performance parameters is essential to a pertinent analysis of the measurements.

The HxRG detectors are at the forefront of astronomy. They are high-performance hybrid photon detectors. The specificities of these detectors will be addressed.

In this chapter, the physics of IR detectors is presented. First, a chronological history of the development of IR detectors is given. Then, a few points on the classification of IR detectors are developed. Following this, a rapid summary of essential aspects of semiconductors is provided, as they are a fundamental aspect of the functioning of the detectors used for the MAJIS instrument. Then, the working of photon detectors and more specifically, the HxRG detectors are addressed. Several performance parameters will be used to characterize the detectors. The physics underlying these performance parameters are described in the final section.

4.1. IR detectors' history

Infrared radiations have only been discovered during the last 200 years by Herschel through experimentation using a thermometer[35] [33]. Three of the leading initial historical discoveries that can be highlighted are [34]:

- 1821: Discovery of the thermoelectric effect and display of proof of the first thermocouple by Seebeck.
- 1829: First creation of a thermopile by Nobili.
- 1833: Alteration of the thermocouple using bismuth and antimony by Melloni.

These discoveries led to the design of the first IR detectors: thermal detectors. Langley designed the first thermal detector, a bolometer, in 1880.

The photon detectors, which have widely dominated the second half of the twentieth century IR detectors' market [33], where invented at the beginning of the twentieth century. These detectors initially made use of the photoconductivity of a substance made of thallium and sulfur discovered in 1917 [34]. In the thirties, Ag-O-Cs phototubes were introduced, which were more stable and became widely used. In 1933, the German physicist Kutzscher developed new, improved IR detectors based on lead sulfide. These detectors were used exclusively by the Germans until 1944 when they started also being produced in the USA.

Extrinsic photodetectors were first developed in the fifties using germanium [34]. These detectors had to be cooled at lower operating temperatures than their intrinsic counterparts.

The idea for Si detectors was explored in 1967 in [38]. It led to the development of silicon Schottky-barrier detectors [34].

The HgCdTe, semiconductor and metal alloy used for HxRG detectors was first researched to allow for **variable bandgap** detectors by Lawson in 1959. The Corporate Research Center in Hopkins, Minnesota also developed HgCdTe IR detection [36]. As will be further developed below, these alloys are very interesting for IR detectors because they retain the properties of semiconductors while allowing for their energy bandgaps

to be adjusted. The primary motivation at the origin of the development of these IR detectors was, and is still to this day, military applications.

The first generation of HgCdTe IR detectors were photoconductive linear array detectors. An intensive research effort during the late 1970s and the 1980s on photovoltaic HgCdTe devices led to the second generation of IR detectors. These second-generation detectors are photovoltaic two-dimensional arrays detectors. The current detectors from this second generation, such as the one used on the MAJIS instrument, are hybrid structures using photodiodes atop ROICs, connected using indium bumps. Recently, some hybrid 1024 × 1024 pixels FPAs have been developed. The trend, up until today, has been to increase the number of pixels per FPA.

It can also be noted that, as the main application of these IR detectors is military operations, a lot of the research on this topic is regulated and subject to many restrictions.

4.2. Classification

As mentioned in the previous section, there are various types of IR detectors. Overall, two main classes of detectors emerge when classifying detectors. These two types are [34]:

- Thermal detectors
- Photon detectors

Thermal detectors receive an IR flux; the flux heats the material of the detector. The temperature change can then be measured using various approaches to estimate the incoming flux. Some relatively common processes that are used in thermal detectors are:

- Thermoelectric voltage
- Thermoelectric resistance
- Pyroelectric voltage

Photon detectors, such as the HxRG detector used on the MAJIS instrument, operate on a different approach. For photon detectors, photons from an incoming IR flux can generate an electric current when a semiconductor absorbs it. A more thorough description of the physics of photon detectors will be made in Section 4.4.

4.3. Semiconductors

4.3.1. General aspects

A semiconductor is a material that has a conductivity between that of an insulator and that of a metal [39]. This intermediate behavior is due to the presence of free electronic particles called holes (positive particles) and electrons (negative particles) caused by the ionization process of the semiconductor material [7]. These particles are referred to as carriers. The first semiconductors were discovered during the 19th century. Since then, they have become a central material of electronic devices, and their use has become widespread [7]. The most prominent semiconductor material used nowadays is silicon.

4.3.2. Extrinsic semiconductors

An important aspect of semiconductors is that they can be made into electric devices that allow for a change in the electrical resistance of the material by the application of a voltage, changes in temperature, or incoming light [7].

The most common of these devices is the p-n junction. Such a device is built from extrinsic semiconductors. Extrinsic semiconductors have had very small amounts of impurities incorporated in them. These impurities are referred to as dopants or doping agents. Their incorporation will impact the density of holes or electrons in the semiconductor's valence band.

There are two types of dopants used on semiconductors, donors, and acceptors. These two types of dopants will change the densities of carriers in the valence band in opposite ways. For instance, with silicon, when doping a silicon crystal with atoms of phosphorus the doping atoms of phosphorus taking the place of silicon atoms will lead to the addition of free electrons to the crystal. Thus as the phosphorus atoms are giving electrons to the silicon crystal, they are called donors. However, if instead of phosphorus, boron

was used, then, the opposite behavior would be observed. An atom of boron would have a missing electron instead, and therefore a hole would be created in the crystal. Thus, the boron would be referred to as an acceptor.

After the introduction of the doping in the semiconductor, these semiconductors are referred to as extrinsic semiconductors. As a consequence of the presence of a doping agent in a semiconductor crystal, the natural equilibrium of carriers of the semiconductor is imbalanced, and either holes or electrons become prevalent in the semiconductor. As a consequence of the predominance of carriers, these extrinsic semiconductors can be classified into two types. If the doping agent was a donor, then the electrons are more dominant than in the base semiconductor, and the semiconductor is an n-type semiconductor. If on the other hand, an acceptor dopant was used, then the holes became predominant, and the semiconductor is a p-type semiconductor.

Photodiodes, which, as it will be explained further down, are at the basis of the functioning of the detectors used for the MAJIS instrument, are made using extrinsic semiconductors. A photodiode is fabricated by creating a junction of p-type semiconductor and n-type semiconductor.

4.3.3. HgCdTe

HgCdTe or mercury cadmium telluride is an alloy composed of the semiconductor CdTe with a direct bandgap of 1.5 eV [24], and the semimetal HgTe. The resulting bandgap energy of the alloy can, therefore, be up to 1.5 eV depending on the mix used. This is one of the rare materials that can be used to detect infrared radiations in both atmospheric windows [5] [10]. One significant advantage of this alloy is that it can reach high levels of quantum efficiency for IR radiations with thinner detectors.

The main advantages of this material can be summarized as [34]:

- The energy bandgap of the alloy can be adjusted to suit the needs of detection over the 1–40 μm wavelengths range.
- This material has excellent optical coefficients, which allows building detectors with high levels of quantum efficiency.
- The generation and recombination processes in HgCdTe are very convenient, and allow use at high operating temperatures.

The detectors used for the MAJIS instrument make use of p-on-n HgCdTe photodiode.

4.4. Photon Detectors

The detectors used for the MAJIS instrument belong to Teledyne's HxRG family of imaging sensors. The HxRG acronym stands for [5]:

H for HAWAII, or HgCdTe Astronomical Wide Infrared Imager.

x can be 1, 2 or 4 depending on the number of pixels along the rows and columns of the FPA.

R for the 4 columns and rows of reference pixels present on the FPA.

G for the possibility to use a guide window.

These detectors are part of the family of photon detectors. Many phenomena can enter into play as photons and electrons interact for the design of a photon detector. These photo effects are [34]:

- Photoconductivity, when the absorption of photons increases the conductivity of a material.
- Photovoltaic systems, when a material induces an electric current or a voltage when exposed to a photon flux.
- Photoelectromagnetic effect, when a semiconductor in a magnetic field generates an electric current or voltage because of the diffusion of photocarriers due to the presence of a carrier concentration gradient.
- Dember effect, when a structure with a single semiconductor doping type with two contacts is subjected to mass photodiffusion and creates an electrical voltage.

- Photon drag, when a photon travels in a material, while the material has an important velocity in a direction perpendicular to the photon, then, the photon will be displaced horizontally by the moving material.

However, only the photoconductivity and photovoltaic systems have been used on a significant scale so far. Photovoltaic detectors, which detectors of the HxRG family are a part of, can be designed using various structures leading to multiple advantages and disadvantages. Some of the most common ones are [34]:

- p-n junctions,
- Schottky barriers,
- metal-insulator-semiconductor (MIS) photocapacitors.

As photon detectors, these detectors function on the absorption of photons by semiconductors. During the propagation inside a semiconductor, the incoming signal's photons will transform in photocarriers. These photocarriers are at the origin of the output signal of the detector. This signal indicates the presence of light on the detector. The signal assesses the magnitude of the power from the incoming light flux.

4.4.1. Photodiodes

The most popular structure used for photovoltaic detectors is photodiodes [34], which, as mentioned before, is also used on the HxRG family of detectors [30]. A photodiode is made of the junction of a p-type and n-type semiconductor. In the case of this detector, the semiconductor used for the photodiodes is HgCdTe.

As shown in the diagram below, photons are entering the photodiode through the top surface. If these photons have a high enough energy to cross the energy gap, they will spawn an electron-hole pair from both regions of the semiconductor. Following a diffusion process, both types of carriers will reach the depletion region, where the important electric field will accelerate carriers on opposite sides. This will create a photocurrent that can be used for the detection process [34].

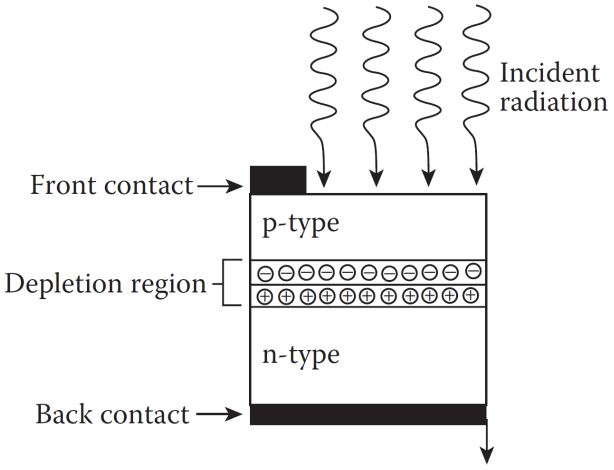

Figure 4.1: p-on-n photodiode diagram [34]

4.4.2. Hybrid CMOS Architecture

Hybrid FPAs were first developed during the 1970s [34]. A hybrid detector is first composed of an absorbing layer. HgCdTe in the case of HxRG detectors. This layer transforms the incoming light into charges that are collected by the p-n junctions. These charges are converted into voltage through the second part of the detector, the ROICs. Both parts of the detector are linked together through indium interconnects [31].

This allows for every pixel to have a single assigned readout electronics chain. Furthermore, because of the indium interconnects and ROIC, the signal from all the pixels of the FPA can be multiplexed. As a consequence, the interface between the cryogenic part of the detector and the electronics can be simplified [34]. Furthermore, in the case of hybrid architecture, the infrared detector material part with the photodiode and the CMOS integrated circuit can be optimized independently both from a material and processing point

of view [32]. It is fundamental for IR detectors. Indeed, silicon arrays are not possible for the IR wavelengths but silicon readouts technology is extremely advanced.

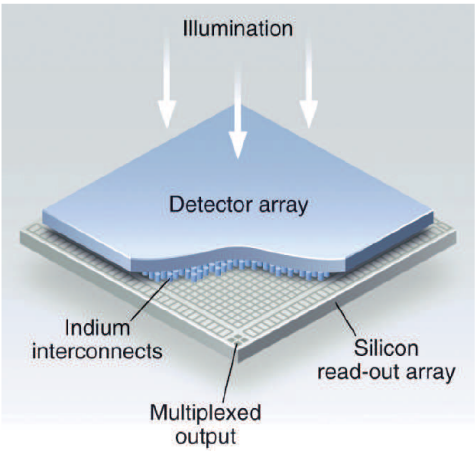

Figure 4.2: HxRG detector hybrid architecture diagram [5]

The diagram below describes the structure used to get the light into the detector up to the ROIC. First, to get as much light as possible into the detector, an anti-reflection coating is applied. In addition to this, Teledyne is currently also using a substrate-removal step to increase the QE of the detector by removing the first layer that had to be crossed [5]. The charges are, then, generated and collected in the photodiode. The charges are then passing through amplifiers to be converted into a voltage. Finally, the signal is transferred using multiplexing and digitized by the ADCs.

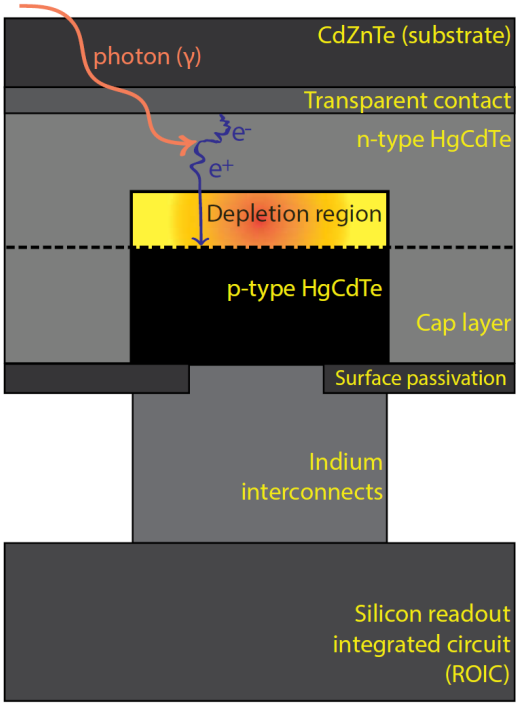

Figure 4.3: HxRG photodiode architecture diagram [30]

One crucial aspect of the design of the MAJIS instrument was that the HxRG detectors were used in a novel way for this mission. The hybrid architecture used, has been optimized for low light level astronomy [5] with long exposures, yet the fluxes associated with the JUICE mission are much higher.

4.5. Performance parameters

This MSc thesis will focus on several performance parameters that are used to characterize the detectors. In this section, the physics of these parameters is described.

4.5.1. Conversion gain

The detector's conversion gain connects the digital signal output to the electrons absorbed by the detector [9]. It is given in e-/DN (or e-/ADU). The digital signal output depends on the readout electronics that are used. Therefore, the conversion gain depends on the detector but, also, on the readout electronics.

It is possible to compute the conversion gains of the detectors using the capacitance of a pixel for an HxRG detector C_0, the conversion factor of the ADC k linking a voltage to a digital signal, and the charge of an electron q [37]:

$$G = \frac{C_0}{kq} \tag{4.1}$$

Using this equation, an expected conversion gain for an H2RG detector was computed to be around 2.15 e-/DN using a 16-bit acquisition mode [37].

It has been shown on various hybrid detectors including the HxRG detectors, that the conversion gain of the detectors given in e-/DN increased the more the well was filled [3]. Using H1RG detectors, variations in gain of 13% from 20 to 70% full-well were observed [3].

Because of these variations, this thesis will sometime refer to a local conversion gain. The local conversion gain represents the gain as it affects the last electrons that have been accumulated. The conversion gain decrease observed in [3] is computed as the average value to be applied to all electrons.

However, chronologically the first electrons that were acquired, had the initial gain applied to them. The more electrons are in the well, the higher the number of electrons required to increase the signal by one DN is. The local conversion gain corresponds to the number of electrons required to increase the signal by one at the current well depth (finite difference).

4.5.2. Well-depth

The detectors described produce very small currents as a result of illumination. These very small currents are unusable by conventional electronics. Therefore, amplifiers built with FETs are used to process the signal [32].

The amplifier will collect charges which will increase its output voltage. These amplifiers have a maximum output voltage V_{max}. The number of charges that can be collected by the amplifier until V_{max} is reached is called the well-depth.

4.5.3. Linearity

Ideally, the response of the detector would be linear up until the well-depth is reached. (i.e. the DN output would be proportional to the electrons absorbed.) However, due to the small nonlinearities in the response of the photodiode [32] and the nonlinearities of the FETs [37] [32], the response of the system is also not entirely linear.

4.5.4. Quantum efficiency

Definition

The quantum efficiency represents the capacity of the detector to absorb photons [32] and convert them into a signal. The differential equation modeling the absorption of the flux is given by the Beer–Lambert law [32]:

$$\frac{\mathrm{d}\phi}{\mathrm{d}l} = -\alpha(\lambda)\phi \tag{4.2}$$

where $\alpha(\lambda)$ is the absorption coefficient in the detector, ϕ is the incoming photon flux, and $\mathrm{d}l$ is the differential thickness of the material. Solving this differential equation allows to compute the ratio η_{ab} of photons absorbed to photons entering [32]:

$$\eta_{ab} = 1 - e^{-\alpha(\lambda)d_1} \tag{4.3}$$

with d_1 being the thickness of the detector. However, not all incident photons end up entering the detector. A reflection factor R called the reflectivity is also to be taken into account. The reflectivity depends

on the refractive index of the material, the refractive index of the material in which the photons are initially propagating, the wavelength of the photon, the angle of incidence, and the absorption coefficient [32].

Having determined the reflectivity r and assuming reflection from the back of the detector negligible, the net quantum efficiency is given by:

$$\eta = (1-r)\eta_{ab} \tag{4.4}$$

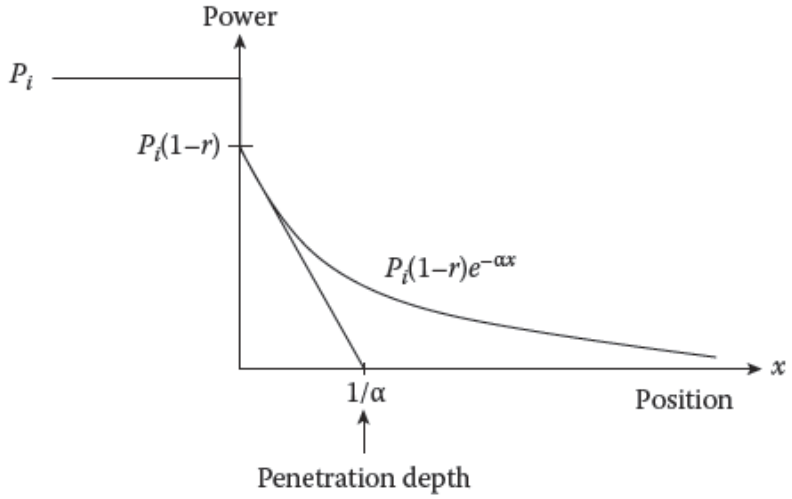

Figure 4.4: Power absorption law in a semiconductor [34]

In practice, the net quantum efficiency will not be characterized. Because there are additional steps required to produce the signal communicating the detection of the photons, additional degradation of the quantum efficiency will occur. The detective quantum efficiency (DQE) will also take into account these degradation processes. It represents the proportion of photons being absorbed and, then, detected to the photons reaching the detector.

General remarks

This process showcases the importance of the thickness of the photodiodes to the quantum efficiency of the photodiode and, thus, the performances of the detector. The quantum efficiency of the detector is dependent on the reflection coefficient and the radiation from the surface of the photodiode. The process also requires that the incoming photons create carriers that can reach the depletion region by diffusion [34].

The QE of the photodiodes relies on the QE of its three regions, the n-type HgCdTe, the p-type HgCdTe, and the depletion region. This is contingent on the diffusion lengths of the electrons and holes being large enough and the thickness of the n-type region being sufficiently small, to increase the probability of a carrier to reach the depletion region. Taking the thickness of the n-type region as the optimization parameter for the quantum efficiency of the photodiode, when the thickness of the n-type region decreases the quantum efficiency of the n-type region increases. However, the quantum efficiency of the other regions will also be affected. This results in a trade-off and a more sophisticated optimization process [34].

4.5.5. Dark current

The dark current is the signal produced by the detector in the absence of any light flux [32].

The origin of the dark current is the generation of carriers in the semiconductor due to the thermal excitation. These carriers are at the source of the dark current.

In extrinsic semiconductors, the probability of free charge carriers is increased compared to intrinsic semiconductors. Therefore, extrinsic semiconductors have much larger dark currents than intrinsic semiconductors [32].

As the generation of carriers is due to the thermal excitation, it is susceptible to temperature changes. FPAs at higher temperatures will have a significantly higher dark current, which is why the nominal operating temperature of IR detectors is low.

The dark current is expected to increase with increasing temperature. The empirical Rule 07 predicts the evolution of dark currents of HgCdTe photodiode as a function of temperatures. Teledyne's HxRG detectors' dark currents can be modeled as a function of temperature using Rule 07. This rule is described by the equations below [40]:

$$J = J_0 \, e^{C \frac{1.24q}{k\lambda_e T}} \tag{4.5}$$

$$\lambda_e = \lambda_{cutoff} \text{ for } \lambda_{cutoff} \geq \lambda_{threshold} \tag{4.6}$$

$$\lambda_e = \frac{\lambda_{cutoff}}{1 - \left(\frac{\lambda_{scale}}{\lambda_{cutoff}} - \frac{\lambda_{scale}}{\lambda_{threshold}} \right)^{Pwr}} \text{ for } \lambda_{cutoff} < \lambda_{threshold} \tag{4.7}$$

where:

Equation Parameter	Parameter Value	Unit
J_0	8367.00001853855	A/cm^2
λ_{scale}	0.200847413564122	µm
$\lambda_{threshold}$	4.63513642316149	µm
Pwr	0.544071281108481	
C	1.16239134096245	

Table 4.1: Parameters for Rule 07

From the previous equation, it is clear that the dark current is a function of λ_e. This explains that the VIS-NIR detectors of the MAJIS instrument will have a significantly lower dark current than MW-IR detectors. This allows VIS-NIR FPAs' nominal operating temperature to be higher.

4.5.6. Noise model

HxRG detectors function on the principle of semiconductors absorbing photons. A photon flux model can assume that a Poisson distribution is followed [32]. The probability mass function of the Poisson distribution is given by:

$$P(k) = \frac{\lambda^k e^{-\lambda}}{k!} \tag{4.8}$$

The photon flux will, therefore, induce a statistical shot noise in the reported measure of the signal.

For large values of λ, the Poisson distribution can faithfully be approximated by a Gaussian distribution of mean λ and standard deviation $\sqrt{\lambda}$. It will be shown later that the photon noise (shot noise) is dominant when large values of λ are encountered.

Furthermore, the dark signal (see the previous section) can also be modeled [9] using a Poisson distribution. Therefore, the dark signal will contribute an additional shot noise.

Finally, the read-out electronics described previously will also have an impact on the noise of the detector. This read-out noise follows a Gaussian statistic [9]. It occurs after the acquisition of the charges, and can, therefore, be added independently to the noise model [9]. To simplify the expression of the equation the quantization noise is included in the read-out noise.

Based on these remarks, the current noise model used is described by the following equation:

$$\sigma_{noise} = \sqrt{\sigma_{RON}^2 + S_{e-}} \tag{4.9}$$

where σ_{noise} is the standard deviation of the signal reported by a pixel (in e-), σ_{RON} is the standard deviation of the Gaussian read-out noise (in e-), and S_{e-} is the signal reported by the pixel (in e-).

Or:

$$\sigma_{noise} = \sqrt{\sigma_{RON}^2 + S_{darke-} + S_{photonse-}} \tag{4.10}$$

where S_{darke-} is the signal due to the dark current reported by the pixel (in e-) and S_{e-} is the signal due to the photons reported by the pixel (in e-).

The following figure (taken from [9]) illustrates the impact of the read-out noise and the shot noises on the total noise, for a read-out noise of 18 e- (typical for an HxRG detector):

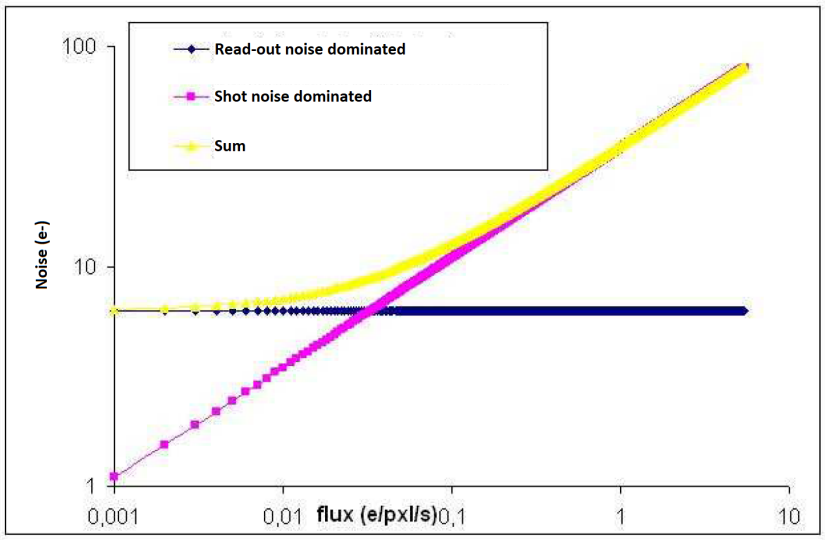

Figure 4.5: Impact of read-out noise and shot noise on the total noise as a function of the incoming flux ($\sigma_{RON} = 18e-$) [9]

Based on Section 4.5.1 observations, it should be noted that the total noise is affected by the local conversion gain and not the average conversion gain. This results in a decrease in the observed noise compared to the model if the average conversion gain is used.

General remarks

One of the consequences of using a thicker detector is an increase in the noise current of the detector. This will reduce the detectivity and therefore, the overall performance of the detector. For given volume generation (G_r) and recombination rates (R_r), the trade-off between noise and quantum efficiency consist in maximizing the ratio [34]:

$$\frac{\eta}{\sqrt{(G_r + R_r)d}} \tag{4.11}$$

where d is the thickness of the detector.

4.6. Conclusion

This chapter showcased several challenges that exist with the development of IR detectors. Currently, the development of IR detectors is not mainly motivated by space research. The HxRG detectors were chosen because they are some of the highest performing detectors for IR astronomy.

A description of the general physics of IR photon detectors was presented. This description gives the relevant background information to the operation of hybrid detectors.

The physical explanations of the performance parameters contribute to a successful realization and analysis of the measurements for the characterization campaigns.

5

FPA's Characterization Methodology

The characterization methodology for the HxRG detectors is discussed in this chapter. Their performances have to be determined in an environment simulating in-flight conditions to gauge compliance with the requirements.

An adapted data reduction scheme has to be implemented due to the specificities of the acquisition of images by MAJIS (see Chapter 3).

Then, the various parameters that will be addressed by the characterization campaign will be reviewed. For each parameter, a description of their respective methodology to characterize them is given in the following sections. These parameters are:

- Linearity
- Full-well capacity
- Quantum efficiency
- RON
- Gain
- Dark current
- Latency
- Operability

The last two sections are dedicated to describing the experimental assembly used for the characterization and the test planning respectively.

5.1. Data reduction

5.1.1. CDS

MAJIS acquisition mode is based on the correlated double sampling (CDS), which consists of making two successive reads on the detector. Specifically, a CDS image results from the subtraction of two images taken successively:

- The first read (reset-read) is performed right after the detector has been reset.
- The second read-out (read) is separated by an interval of time corresponding to the integration time of the CDS image.

The reset eliminates charges generated before the observation time of interest. However, after this reset, variations in offset voltage are observed, which leads to the apparition of a reset noise. This reset noise can be significant (standard deviation of 50-200 electrons). By applying the CDS mode acquisition, this noise

is removed [2]. This is consistent with [2], who recommend using CDS to improve the performances of the HxRG.

The three following 512-rows images show an example describing the construction of a CDS image. The first image shows both the reset-read (bottom 512 rows) and the read (top 512 rows) captured by the detector. Then, the following image is the CDS resulting from the subtraction of the read and reset-read:

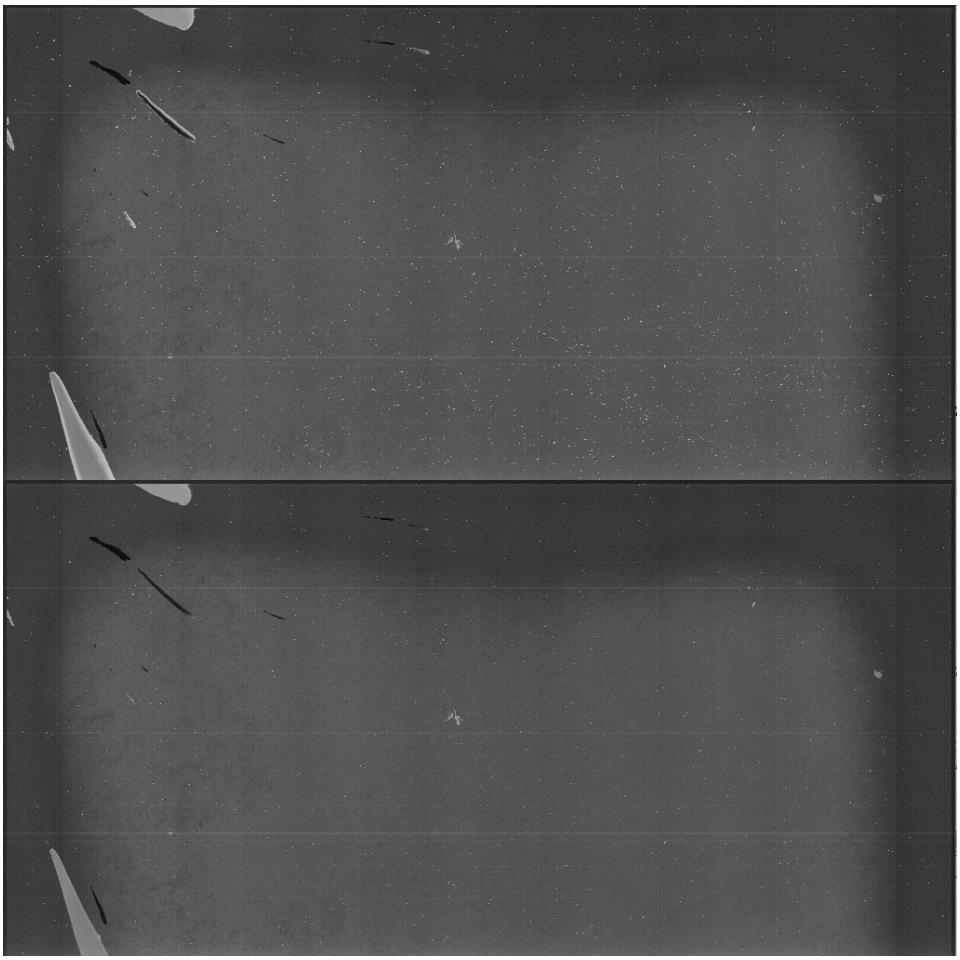

Figure 5.1: fits file containing two 512x1024 images

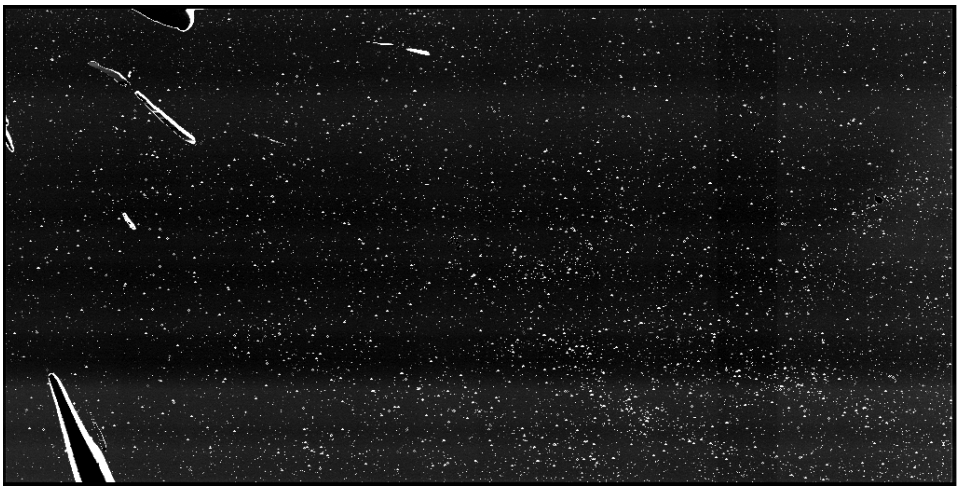

Figure 5.2: 512x1024 CDS image

However, the CDS images produced can not be used directly. Some perturbations remain (see Section 5.1.2). These perturbations can be mitigated using additional post-processing.

5.1.2. Post-processing

After CDS, the main residual perturbation is a reset perturbation (kTC effect) that is present across the lines of the detector. This effect is most noticeable on reference columns. (The HxRG detectors have 4 columns/rows on the top, bottom, right-side, and left-side of the detector which are not connected, and are therefore not light-sensitive. These are called reference columns/rows.) On a reference column the signal should be flat around the 0 value (save for the CDS noise). However, on CDS images, the signal from reference columns is not flat as shown in the figure below:

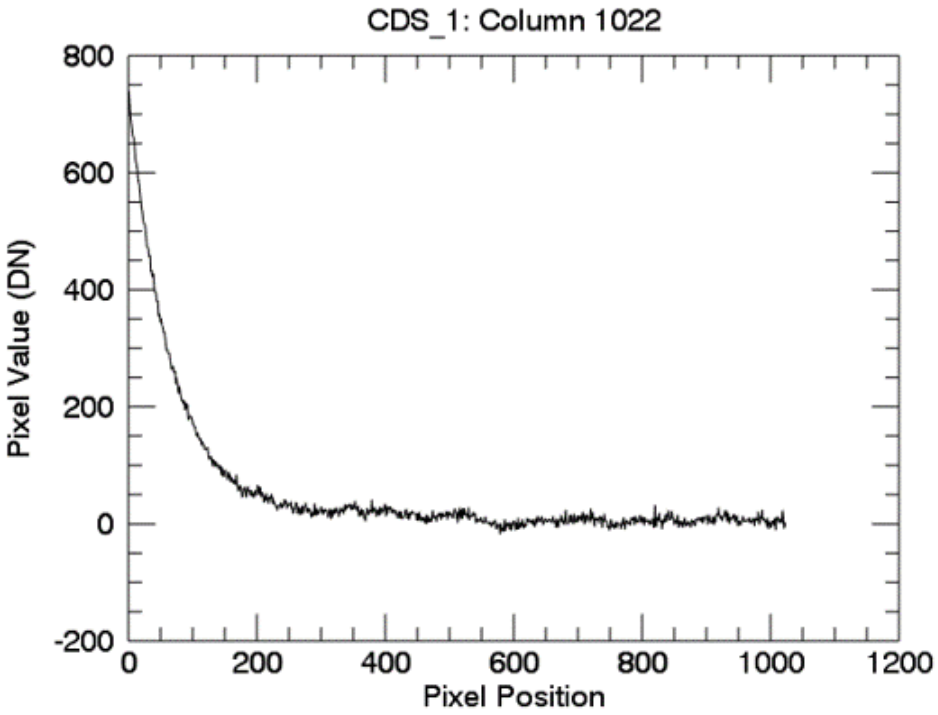

Figure 5.3: Reference column pre processing, with reset (kTC) perturbation present

Even though this reset perturbation is the most visible on reference columns, it is also present on the entire 1024x1024 frame, which requires a row correction for the entire frame. This reset perturbation is not constant from one frame to the next. Therefore, correcting each image is necessary. The same procedure will be used in-flight. The correction method is described below:

1. For each row, the 8 reference pixels (4 on each sides) are taken:

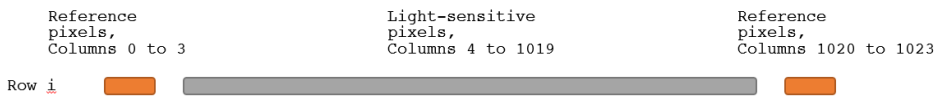

Figure 5.4: Row i pre correction diagram

2. The 8 reference pixels are sorted in increasing order.

3. Only the 4 reference pixels from the middle of the sorting are selected. (This step is implemented to take into account eventual spikes on reference pixels.)

4. The mean value M_i of these 4 reference pixels is computed. This mean value is, then, subtracted to the entire row. (Including reference pixels) :

$$Row_{corrected} = Row_i - M_i$$

Figure 5.5: Row corrected diagram

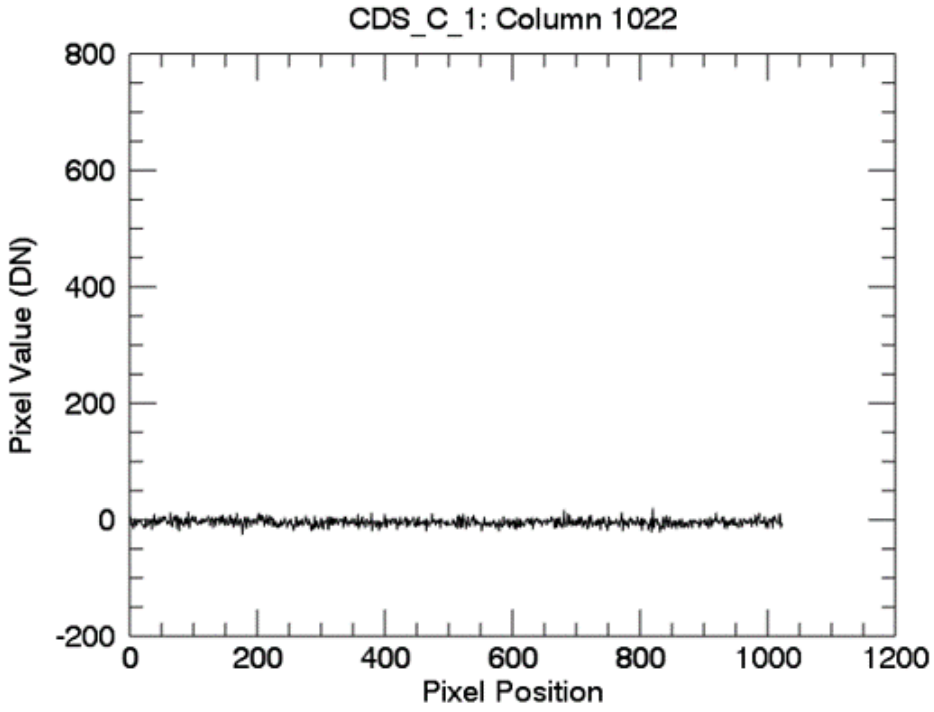

Figure 5.6: Reference column post processing, with reset (kTC) perturbation corrected

Finally, for some measurements such as quantum efficiency, a dark subtraction is required. To perform a dark subtraction, a series of N dark CDS images is captured just before the measurement series. A mean frame of the N dark CDS images is computed and then subtracted to each CDS image of the measurement series.

5.2. Linearity

5.2.1. Description

The linearity refers to the capacity of a detector to convert a quantity of light arriving on a pixel to a proportional DN output signal [32]. (The absorption of photons generate a voltage in the photodiodes. An ADC (Analog To Digital Converter) is used to convert this voltage signal into a Digital Number (DN) also referred to as Analog Digital Unit (ADU).) Ideally, the detector should be able to maintain this behavior for varying light quantities, and in different types of settings. However, this type of behavior is never perfect (see Section 4.5.3). Therefore, the linearity of a pixel is measured by comparing its response w.r.t. a theoretical linear fit. The choice of the linear fit is essential to the quality of the characterization for the linearity. It will directly impact the deviation measurement used to assess the linearity.

Small deviations to the linearity allow better modeling of the response and simplify the mathematical analysis of images. In practical terms, if the detector has small deviations, fewer measurement points are necessary to interpret the response. In-flight this avoids potential misinterpretation of the MAJIS results. For these reasons, the MAJIS instrument limits the tolerated deviation to linearity to a 5% margin.

5.2.2. Characterization procedure

Based on the knowledge of the physics of these detectors, non-linear behaviors are more commonly expected when the well is either close to being empty or close to being saturated. Therefore, during the characterization of the FM detectors, finer spacing will be used when in these areas (empty and saturation).

There are several approaches possible to evaluate the linearity of a detector. Two techniques are introduced in this section.

The linearity can be computed for every single pixel or the whole FPA as an average of every pixel. The average gives a more intuitive measure of the linearity, but for the characterization, it is required to address the linearity for each pixel. The procedure to get the linearity for every pixel and the average FPA are equivalent. To address the average linearity, selecting only operable pixels (see Section 5.9) can help avoid being impacted by outliers. Though, as the inoperable pixels are in minority, it is not mandatory. In this section, the methodology for a single pixel is described.

Linearity in charge

Successive CDS images will be taken, using increasing integration times. The measured values are ordered by increasing integration times, and the linear fit is computed. Typically, it will be computed using a least-square approach. An additional constraint on the fit is to make it pass through the (0, 0) point.

The quality of the linearity of the detector is based on the deviation of the experimental points w.r.t. the linear fit. When the linearity is measured w.r.t. the integration times, it is referred to as linearity in charge (or integration time linearity).

Flux linearity

Another analogous approach is to use increasing incoming flux for constant integration time. When using the IR detector, this can be done by increasing the temperature of a black body situated in front of the FPA. Although, this can impact the thermal control of the set-up. The linear fits are then computed w.r.t. the incoming flux. This approach is referred to as flux linearity.

For this approach, the measured signal is compared to the exact flux the detector received. This requires precise knowledge of the experimental assembly's radiometry. For this reason, linearity in flux measurements are harder to set up than linearity in charge.

5.3. Full-well capacity

5.3.1. Description

The full-well capacity is aimed at measuring the capacity of a detector to capture photons, without resets, before reaching saturation. This aspect is fundamental as in-flight it will determine the maximum integration times for observations. The integration times have to be chosen to ensure that the images are acquired while the detector is still operable.

A pixel is considered saturated after it has captured enough photons to deviate from its nominal behavior. The level at which a pixel is saturated can be defined in several ways. The FWC will vary from pixel to pixel, but these variations will usually be relatively small w.r.t. the median FWC across a given FPA.

As the FWC depends on the nominal behavior, the FWC is correlated to the linearity.

5.3.2. Characterization procedure

To estimate the FWC during the characterization campaign, the intersection of the FPA's linearity data with the 5% deviation line will be used (See Figure 5.7). Consequently, the FWC estimation for the FPA is intrinsically linked to the linear fit. As an example, for the following plot the FWC would be estimated around 73,000 e-:

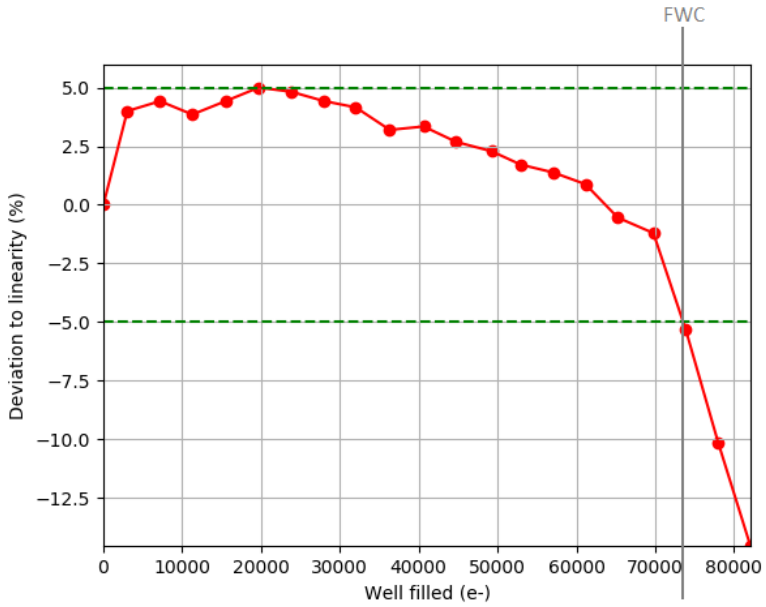

Figure 5.7: Example of deviation from linearity on an HxRG detectors

5.4. Quantum Efficiency (including PRNU)

5.4.1. Description

The quantum efficiency (QE) characterization consists in measuring the detective quantum efficiency. For the characterization, quantum efficiency and detective quantum efficiency will be used interchangeably. The physics of QE was previously addressed in Section 4.5.4. During the science phase, the QE of the FPA will influence both the interpretation of the images captured and whether certain types of observations are possible. Lower QE levels mean higher integration times to reach the level of signal desired.

The detective QE measurements, for a given pixel, is usually defined by the ratio:

$$\eta = \frac{N_e}{N_p} \tag{5.1}$$

where N_p is the number of photons received on each pixel, and N_e is the equivalent number of electrons to the signal output of the pixel. The quantum efficiency is aimed at measuring how much of the photons from incoming light flux are transformed into signal by the detector.

Similarly to the linearity, the quantum efficiency measurements of all pixels can be averaged to give a QE measurement for the entire FPA.

5.4.2. Characterization procedure

Detectors are sensitive only to specific wavelengths. Therefore, it is evident that the QE depends highly on the wavelength of the incoming photons. To fully characterize the QE of a given detector, several measurements have to be performed at as many wavelengths as desired. A QE measurement, at a given wavelength, will be done by filtering the incoming flux around that wavelength.

Based on the radiometric model and measurements performed during the characterization campaign, the incoming flux power on every pixel of the detector will be estimated for all QE measurements. To get the flux for each pixel, the inhomogeneity of the flat-field has to be corrected. It is, then, straightforward to compute the number of photons per second reaching the detector using the photon energy equation:

$$E = \frac{hc}{\lambda} \tag{5.2}$$

where h is Planck's constant and λ is the photon's wavelength.

With the number of photons reaching a given pixel per second the QE map is computed (Eq. 5.1) based on the signal observed (dark subtracted) on the associated CDS images.

From the QE map, the PRNU can be computed by comparing each pixel reported QE to the detector's median QE.

5.5. Noise

5.5.1. Description

The CDS noise is the uncorrelated noise measured on a CDS image. Using the CDS noise estimated on a series of images, it is possible to estimate the read-out noise of the detector using the noise model presented in Section 4.5.6.

To precisely assess the performance of the detector, the read-out noise is valuable. The read-out noise represents the lower limit of the noise that can be obtained with a given detector (very low signal).

For the JUICE mission, the HxRG detectors will be operated using near/full-frame retrieval over short integration times (« 1 sec) (see Section 3.7). In these non-standard conditions, it is essential to maintain good noise performance.

From previous measurements, it is known that a significantly different read-out noise is expected on reference pixels and connected pixels . The overall performance of the FPA depends on both.

5.5.2. Characterization procedure for the CDS noise

Two approaches allowing the estimation of the uncorrelated noise using CDS images will be presented.

The first approach that is proposed consists in computing a Laplacian that will allow estimating the noise on a given column of the detector. This approach is useful for a first-order estimation of the CDS noise using only two images.

This method consists in picking two successive columns (index i and $i+1$) from the same output. (The H1RG detectors used are made of 16 output channels. Each channel is composed of 64 columns of 1024 pixels.) These can be two reference or two connected columns. The following equation gives the CDS noise estimator:

$$\sigma_{CDS} = \frac{\texttt{STD}(\,(CDS2_{i+1} - CDS2_i)\; -\; (CDS1_{i+1} - CDS1_i)\,)}{2} \tag{5.3}$$

The second approach will be used more systematically for the characterization. It allows estimating the noise from individual pixels. This method requires more images to produce significant results. N successive CDS images with the same integration time are taken (The larger N is, the more significant the results are.). The noise of a given pixel is measured by computing the standard deviation of the signal value measured by the pixel across the N measurements.

5.5.3. Characterization procedure for the Read-out noise

To estimate the read-out noise the contribution of the shot noise to the CDS noise has to be eliminated. If the signal observed on the detector is too high, the shot-noise will be too high (4.9) and, therefore, drown the read-out noise. To conserve accuracy on the estimation of the read-out noise, it is best to estimate the read-out noise on pixels with low signal levels.

To compute the RON, first an image is taken. Then, using the histogram of this image, only a subset of all the pixels are selected based on their signal level. This is showcased in the following figure:

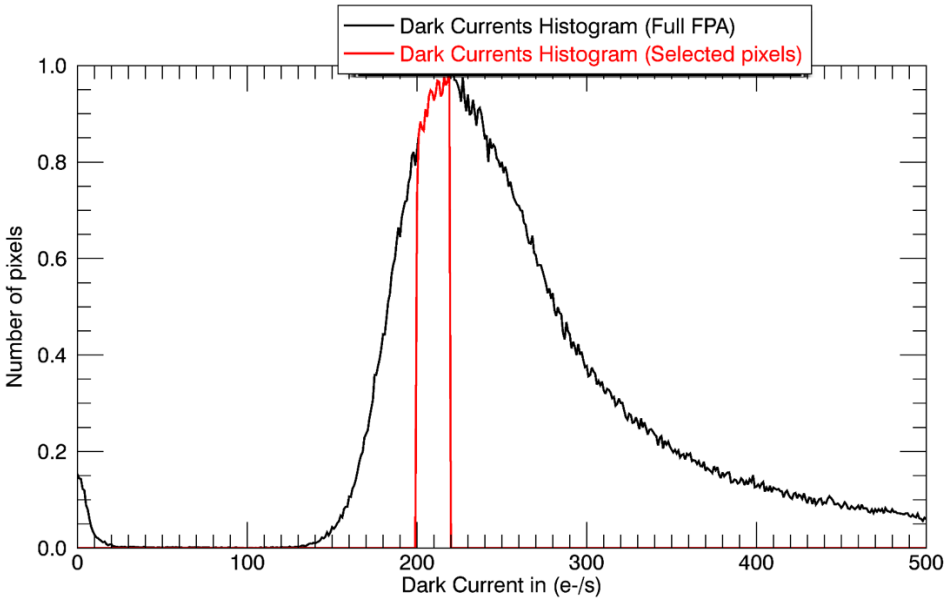

Figure 5.8: Dark currents histogram - Selection of pixels for read-out noise estimation - Slow 100kHz - EM - 84K

Using the pixels selected by this approach (Figure 5.8), the contribution from the shot-noise is given directly by Equation (4.9). In the example illustrated by Figure 5.8, the CDS noise model becomes $\sigma_{noise} = \sqrt{fix^2 + 210}$.

Then, to estimate the contribution of the RON, a Monte-Carlo simulation is used. This Monte-Carlo simulation gives a prediction of the expected CDS noise histograms for various RONs. The Monte-Carlo simulation assumes that the RON is constant across all pixels of the FPA. The RON estimation is based on which value of read-out noise gives the Monte-Carlo histogram with the best fit for the actual data histogram. The following figure shows the CDS noise histogram for the selected pixels on images captured using a detector at 84K and its best Monte-Carlo fit:

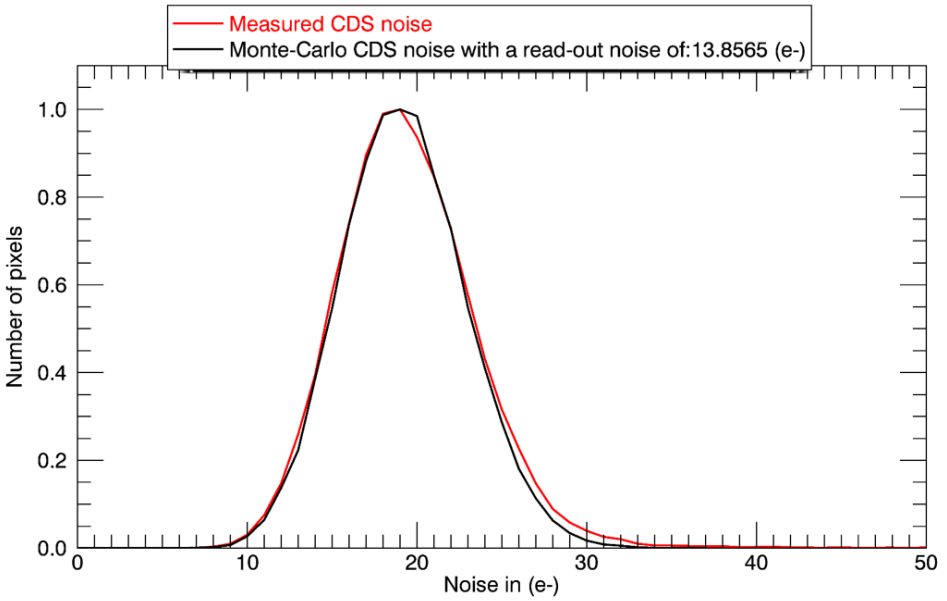

Figure 5.9: CDS noise histogram - Monte-Carlo Fit - Slow 100kHz - EM - 84K

This figure shows a very good match between the Monte-Carlo simulation and the histogram of measured

CDS noises.

5.6. Conversion gain

5.6.1. Description

The gain of the detector is used to convert the reading in digital number (DN) into the number of electrons absorbed by the detector. The detector's gain is essential to convert the measurements into physically meaningful quantities. The gain affects all measurements. As such, it is important to have access to the gain rapidly.

5.6.2. Characterization procedure for the gain

Various approaches allow estimating the gain at different degrees of precision. The first approach is to estimate the gain based on a performance parameter that is already known. For instance, the RON of reference pixels can be used; it has not significantly varied between all detectors characterized for the MAJIS instrument. (The FWC is another parameter that can be used.)

A more rigorous approach is to use the noise model to estimate the detector's gain [19]. The equation for the noise model of the detector is given by Eq. (4.9). Based on this equation, a similar equation can be derived from the noise model using digital numbers instead of electrons. This equation is:

$$\sigma^2_{noiseDN} = \frac{fix^2_{DN}}{G} + signal_{DN} \tag{5.4}$$

Based on this equation, the gain estimation methodology consists of making a linear fit for the G parameter. This is done by selecting points at different signal values and using their estimated CDS noise to fit a line through the data. To retain as much accuracy as possible it is better to remain in a linear part of the detector, i.e. ideally the data should sample the start of the well.

5.7. Persistence

5.7.1. Description

The persistence of the detector represents the impact of the previous capture on the current capture. After a reset of the detector (before a new image acquisition), some of the electrons may not have been completely flushed out and remain from the previous image. Typically, HxRG detectors have been shown to have very low levels of persistence (as low as 0.01% of persistence) [5]. It is not expected that the persistence will noticeably decrease the performances of the MAJIS instrument.

5.7.2. Characterization procedure for the persistence

To estimate the impact of the latency, an acquisition that received a significant amount of photons (enough to fill at least 50% of the well) is followed by an acquisition that received as little flux as possible. The second acquisition (low flux) is, then, compared to other (low flux) acquisitions, which were not preceded by a high flux acquisition.

To perform such a measurement, a series of N images will be acquired. At the beginning of the series (for the $\frac{N}{2}$ first images), a high photon flux will light the detector. Around the half-way point of the series, a shutter will close to prevent any flux from reaching the detector.

To implement this measurement, the timing diagram of a series of acquisitions is required. The shutter will not close instantaneously, therefore, it would be ideal if the shutter would close between two acquisitions. However, this might not be possible depending on the timing diagram.

In any case, synchronization between the shutter and the image acquisition should be implemented. The synchronization's error tolerance will depend on further investigations of the timing diagram of the acquisition software. The shutter closing time for the VIS-NIR experimental set-up is 42ms.

- Case 1:

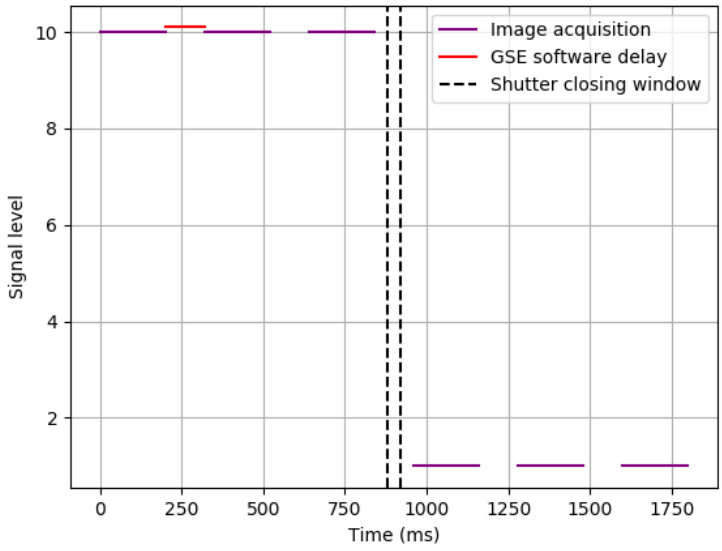

Figure 5.10: Timing diagram for a persistence measurement - Large time window

If the timing diagram shows that, between the end of the acquisition of an image and the beginning of the following acquisition, there is a time window larger than 42ms, then, the shutter closing should take place during this time window. The synchronization error tolerance depends on the duration of the time window (e.g. time window is 100ms –> error tolerance < (100 - 42) / 2 = 29 ms). In that case, the DIT of an image does not have an impact on the test sequence.

- Case 2:

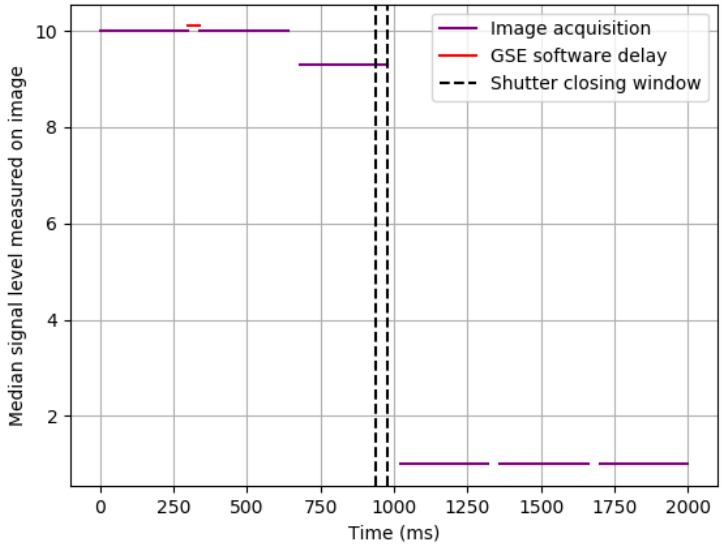

Figure 5.11: Timing diagram for a persistence measurement - Short time window

If the timing diagram shows that, between the end of the acquisition of an image and the beginning of the following acquisition, there is a time window shorter than 42ms, then, the shutter closing should take place at the end of an acquisition. When the acquisition has ended, the shutter is closed, the

following acquisition can be used to measure latency. The synchronization error tolerance has to be lower than the duration of the time window. In that case, the DIT of the images has to be large enough so that the shutter closing time does not impact the acquisition too much (DIT » shutter closing duration).

Assuming that one of the previous procedures has been implemented successfully, the persistence for each pixel can then be computed as a percentage of the signal from the image before the closing of the shutter.

5.8. Dark Current (including DSNU)

5.8.1. Description

During photons acquisitions by a photodiode, an electric current flowing through the photodiode will produce what is referred to as dark current. This will cause measurements to report the presence of constant flux. However, this flux is not due to the incoming light.

The characterization of dark currents allows for a more precise analysis of acquisitions and correct interpretation of the data. The dark current is important to ensure that the well does not get filled too fast (decreased SNR). The dark current can vary with time. Dark currents have been, in the past, shown to increase significantly the more the detectors age [6].

5.8.2. Characterization procedure

The characterization of the dark currents will be done by capturing long exposure images. During the capture, as few photons as possible should reach the detector. This is done through the use of a cold (limit black-body emission) and closed shutter (limit photons). Using this approach, the signal reported by the pixels of the FPA will be primarily dominated by the dark current. Multiple acquisitions will increase the significance of the results. A map of dark currents will be produced based on these measurements.

The dark current is highly dependent on the temperature of the detector. Consequently, a full characterization of the detector has to include the full range of operational temperatures.

From the dark currents map, the DSNU can be computed by comparing each pixel reported dark signal to the detector's median signal.

Correction strategy

In-flight, these dark current measurements will be acquired before each new type of observation and subtracted to the images for scientific analysis.

To mitigate the dark current, it is also possible to reduce the operating temperature (as long as the temperature remains in the given operable range). However, this is not always feasible in-flight.

5.9. Operability

For the flight model and flight spare detectors, several pixels (< 1%) are expected to be inoperable, i.e. they will behave significantly non-nominally. The signal levels reported by these pixels are to be analyzed with care, to avoid any misinterpretation of results. The three different categories of inoperable of pixels are:

- Pixels that are entirely non-responsive to the dark current or solely saturated are dead pixels (DP).
- Pixels that show inconsistent measurements (high noise) are hot pixels (HP).
- Pixels that show high values of DSNU and PRNU are warm pixels (WP).

To identify those pixels, maps will be generated for the whole FPA at various FPA temperatures. The operability map combining all types of inoperable pixels yields an operability map.

A subset of conditions will be applied to each pixel. These conditions will determine whether a pixel is considered operable or not. Some of the properties that are being currently considered for the operability of pixels are:

- Dark current
- CDS noise
- Quantum efficiency
- Linearity

The results of the operability will vary depending on the conditions being used as constraints.

5.10. Experimental assembly IR

In this section, the experimental assembly that is used for the characterization campaign of the IR detectors is described. As described in this chapter, several tests need to be performed to characterize the detector fully. This experimental assembly was designed to allow for all relevant aspects to be tested.

The experimental assembly is situated in a clean-room of the research institute. This ensures that no contamination will compromise the detector or perturb the testing.

5.10.1. Description

Initially, two configurations (C1 and C2a) will be used for the characterization procedure. Configuration 1 allows performing a majority of the characterization campaign. This includes the measurements for dark currents, RON, FWC, and linearity. The following diagram describes configuration 1 in detail:

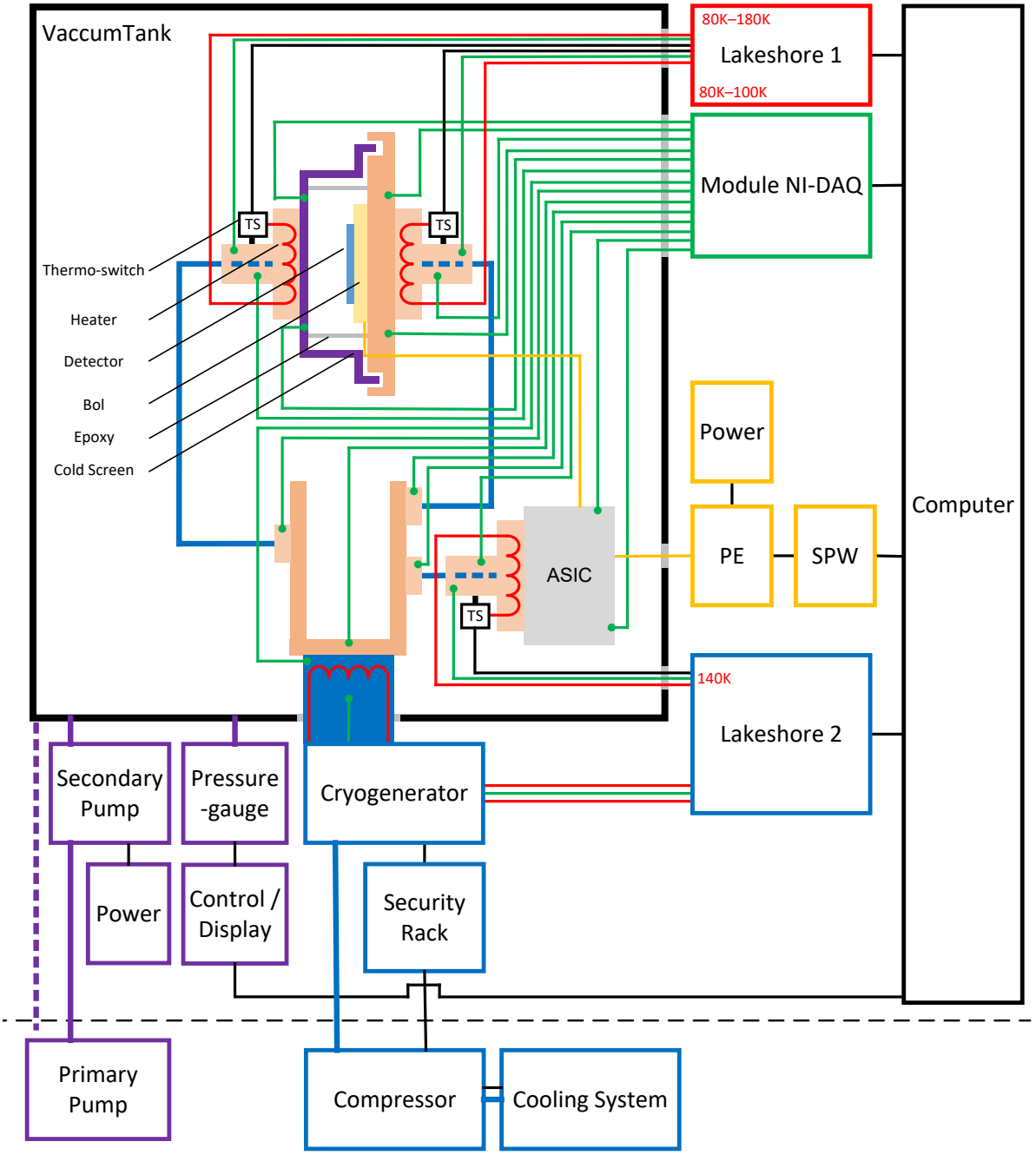

Figure 5.12: Characterization bench configuration 1 [18]

The configuration 2a is slightly more advanced. It is designed to also allow for the QE measurements and, therefore, it requires a suitable source of illumination (IR emitter in figure 5.13). In addition to the IR emitter, an integrating sphere is used to distribute the IR flux evenly. The last important element added is the filter that allows selecting a specific wavelength. The following diagram describes configuration 2 in detail:

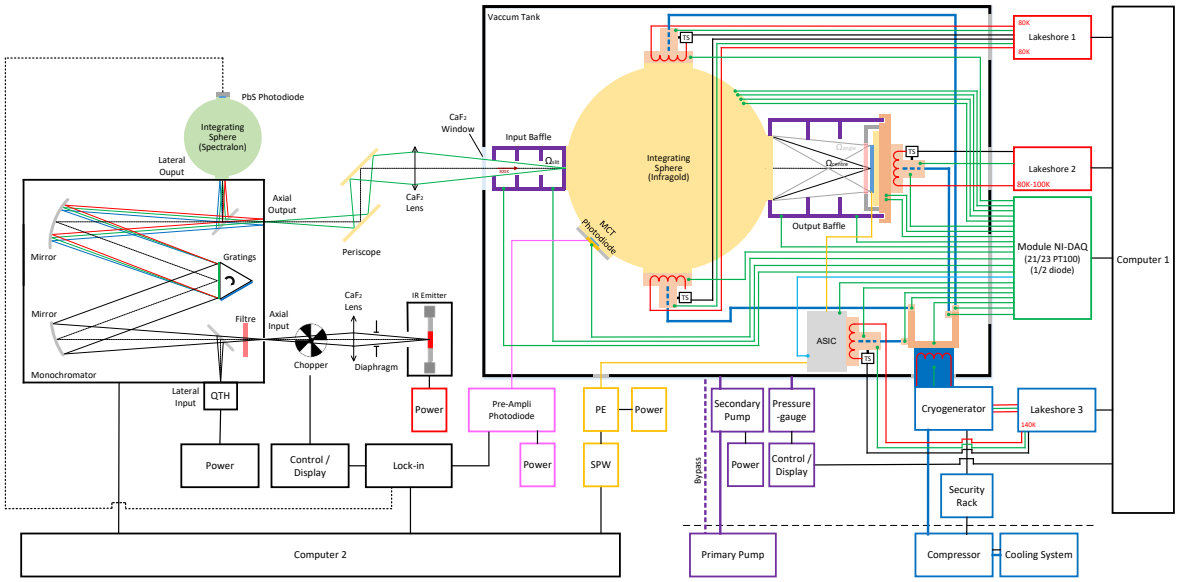

Figure 5.13: Characterization bench configuration 2a [18]

5.10.2. Validation

This experimental assembly has been validated through the use of detectors which had already been characterized. This allowed comparing the results using this experimental assembly to the expected and reported performances.

5.11. Experimental assembly VIS-NIR

In this section, the experimental assembly that is used for the characterization campaign of the VIS-NIR detectors is described based on an IASB internal document (IASB-MAJ-TN-003).

Similarly, as for the IR set-up, the experimental assembly is situated in a clean-room of the IASB. Three configurations exist for the VIS-NIR experimental assembly.

In configuration 1, a cold plate is in front of the detector, removing all flux reaching the detector except for the black-body emissions of the plate and radiation shield.

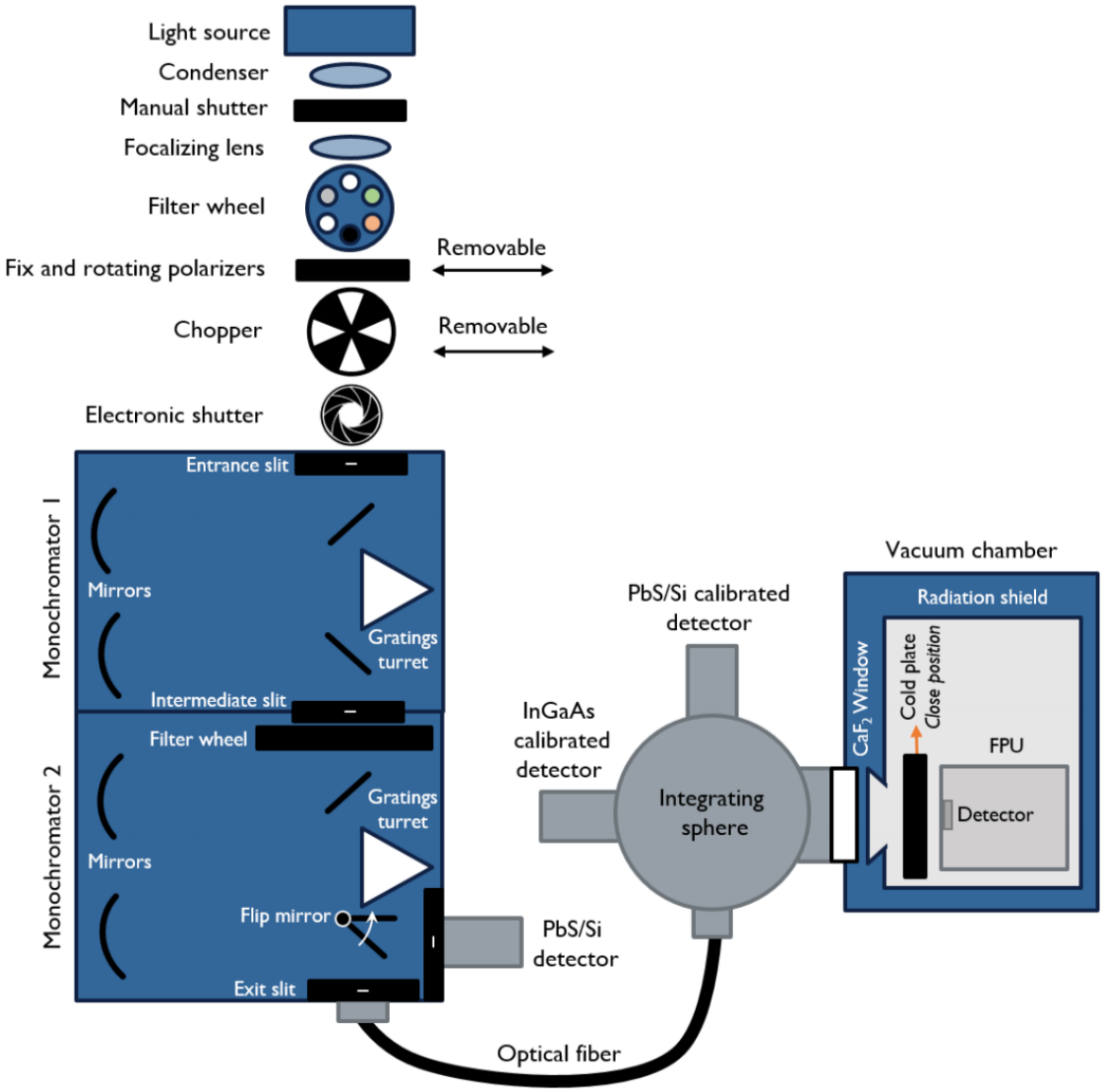

Figure 5.14: VIS-NIR characterization bench configuration 1

In configuration 2, a variable intensity light source covering all wavelengths required for the VIS-NIR FPA characterization is present in front of the detector. This light source is composed of a quartz halogen lamp providing the photons, a filter wheel to tune the intensity of the flux and a double monochromator to provide monochromatic light.

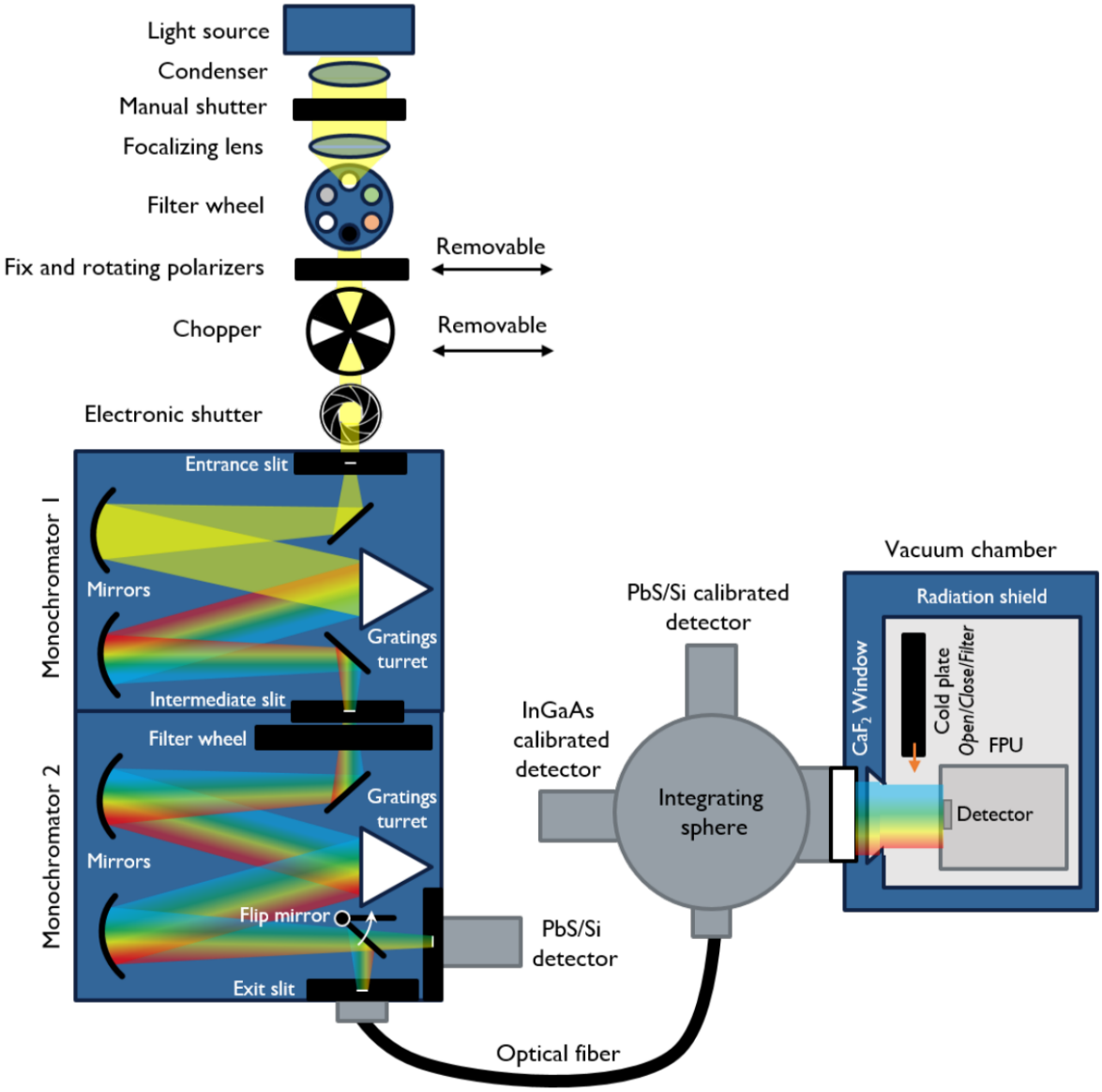

Figure 5.15: VIS-NIR characterization bench configuration 2

In configuration 3, the LVF used by the MAJIS instrument to focalize different wavelengths on different columns of the detector is present in front of the detector. To reproduce the behavior of the MAJIS spectrometer, a focusing array produces the convergence beam that reaches the LVF.

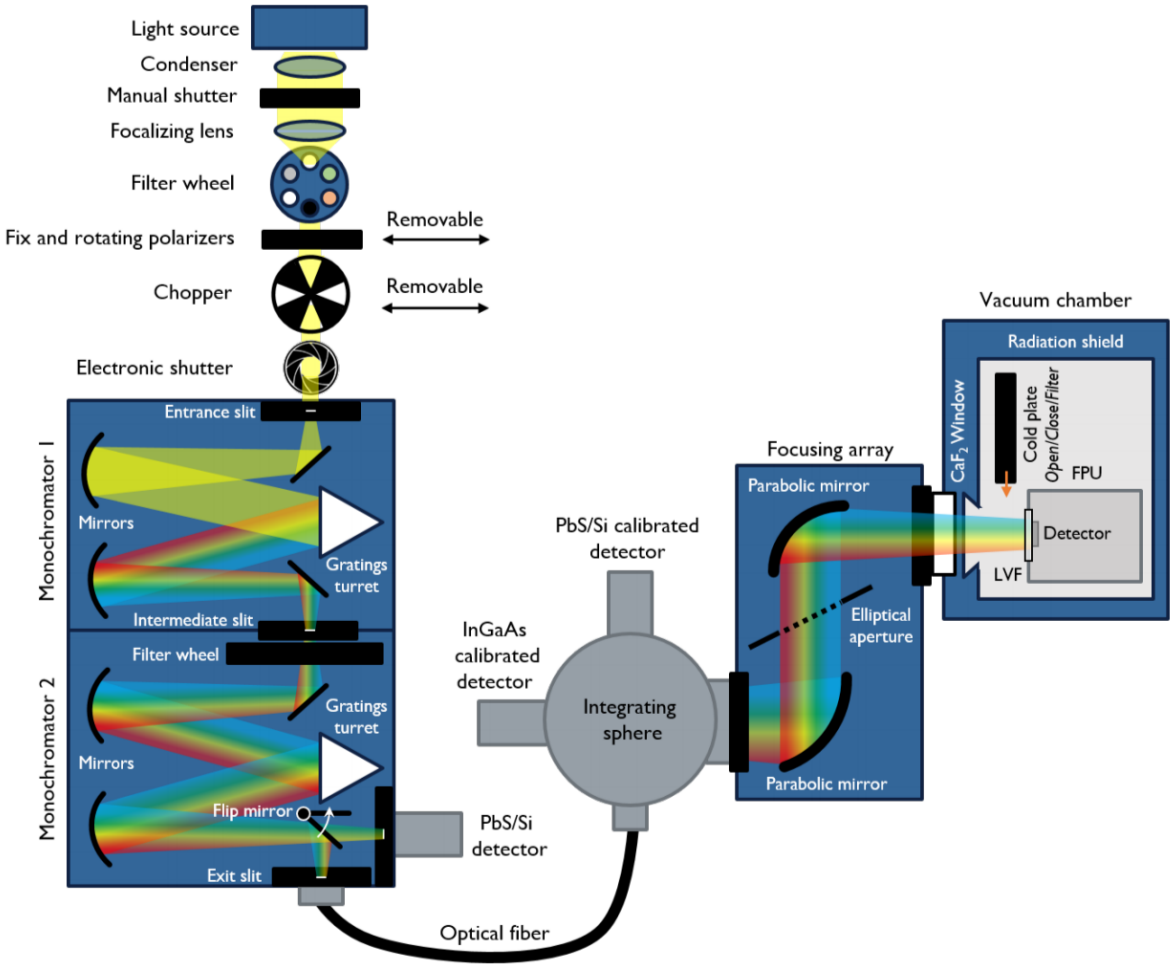

Figure 5.16: VIS-NIR characterization bench configuration 3

5.12. Test Plan

Several aspects entered into play for the preliminary design of the test plan. Central parameters are the data volume and duration of the measurements of the entire campaign.

Duration

The length of the campaign is dependent on several aspects. Based on the previous campaigns performed at the IAS, some of the elements that should be considered to give a significant estimation of the duration of the tests are:

- Thermal dynamics (expected to be the main limiting factor)
- Number of measurements
- Adjustments and tuning
- Redundancies in testing/optimization

As an example, the following organizational chart describes a simple cycle that aims at minimizing the duration of the testing:

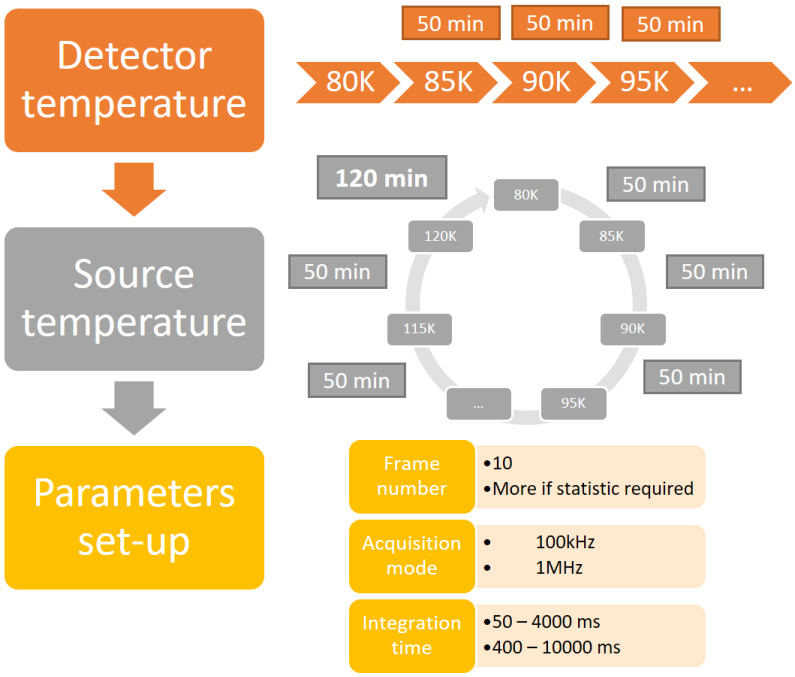

Figure 5.17: IR Detector characterization campaign cycle organizational chart in configuration 1 (Light source is a black body)

The previous figure highlights the importance of limiting the number of temperature changes to reduce the duration of the campaign. The thermal dynamic of the set-up is relatively long, which is why it is essential to avoid going back and forth between temperatures. Due to the capacities of configuration 2 to perform measurements more rapidly, it is planned that only 2 source temperatures will be used in configuration 1 for the flight campaigns.

Due to readiness issues, the EM-IR campaign only covered configuration 1.

The number of FPA temperatures covered will depend on the time available. For the IR FPA, the goal is to at least cover the following temperatures: 75, 80, 90, 95, 100, and 105K (JUI-IAS-MAJ-PL-034). The following table summarizes a sequence of measurements for configuration 1 (JUI-IAS-MAJ-PL-034). This sequence will be performed at the beginning of the flight detectors' characterization.

Characterizing:	**FPA T**	**Parameter change**
Dark+FWC+DSNU+RON	90	Source T set to 90K
Gain+Linearity	90	Source T set to 110K
Dark+FWC+DSNU+RON	95	Source T set to 90K
Gain+Linearity	95	Source T set to 110K
Dark+FWC+DSNU+RON	...	Source T set to 90K
Gain+Linearity	...	Source T set to 110K

Table 5.1: Configuration 1 test sequence

The sequence for configuration 2 is described below. Configuration 2 will deliver more types of measurements (JUI-IAS-MAJ-PL-034-1.0):

Characterizing:	**FPA T**	**Parameter change**
Dark	90	Dark conditions
Gain+Linearity	90	Black-body emitter temperature set to 1023K Monochromator: $\lambda = 2.25\mu m$, $\Delta\lambda = 20nm$
Persistence	90	$\lambda = 2.25\mu m$, $\Delta\lambda = 100nm$
QE	90	$\lambda = 2.25\mu m$,..., $\lambda = 5.60\mu m$
Linearity	90	$\lambda = 4.5\mu m$
Gain+Linearity	95	$\lambda = 2.25\mu m$, $\Delta\lambda = 20nm$
Persistence	95	$\lambda = 2.25\mu m$, $\Delta\lambda = 100nm$
Gain+Linearity	...	$\lambda = 2.25\mu m$, $\Delta\lambda = 20nm$
Persistence	...	$\lambda = 2.25\mu m$, $\Delta\lambda = 100nm$

Table 5.2: Configuration 2 test sequence

These sequences were designed to optimize the duration of the campaign and ensure that all the performance parameters are addressed.

Similar, but independent, test plans are designed for the VIS-NIR campaigns by the team at the IASB.

5.13. Conclusion

The main elements of the methodology developed for the characterization of the detectors of MAJIS are described in this chapter. The data-reduction process was implemented to eliminate several perturbations affecting the detector. Unperturbed images allow for a correct interpretation of the measurements reported by the detector.

The characterization procedures shall provide accurate estimations of all the parameters relevant to the performances of the MAJIS instrument.

The experimental set-up and test plans have been designed to provide all the measurements required to successfully perform the characterization campaigns.

6

Results of EM IR campaign

6.1. IR campaign

The EM (Engineering grade model) IR detector of the MAJIS instrument was characterized to anticipate and prepare for the characterization of the flight model and spare detectors. Most of this characterization campaign was performed using the Slow 100kHz acquisition mode. Several measurements were made to ensure that the images did not change significantly using the Fast mode. For the full characterization, the measurements are expected to be performed for both acquisition modes. This EM characterization will cover the following performance parameters:

- linearity
- dark current
- noise
- operability

The methodology used for the analysis of the results from this campaign was described in Chapter 5.

6.2. Data reduction

In addition to the data-reduction presented in Chapter 5, another step was included. During the pre-campaign analysis, a significant amount of stray-light was noticed on the detector. This stray-light will not be present while in-flight. Its origin is linked to the experimental set-up. This stray-light will also impact the characterization of the IR flight detectors. Therefore, if not taken into account, its impact during the campaigns will prevent an accurate characterization of the performances of the detector.

The stray-light observed on the detector was independent of the FPA temperature. Based on the dark current section from Chapter 4, it is known that for the HxRG detectors the dark current decrease rapidly with decreasing temperature. Images were, then, taken with an FPA at 72K in dark conditions. These conditions were used to isolate the stray-light. Therefore, all the remaining signal observed on the images was dominated by the stray-light.

To take into account these observations, the following procedure was followed for the analysis of each image. A mapping of the stray-light was produced based on the images captured at 72K. For all image acquisitions during the EM IR campaign, after the data-reduction procedure presented in Chapter 5 was followed, the stray-light map was, then, subtracted to the CDS image. With this subtraction, a meaningful analysis of the measurement could be performed.

6.3. Linearity

The linearity of a pixel is evaluated to estimate how much of the well can be used without entering a significantly non-nominal behavior.

6.3.1. Performance estimation - Basic linear fit

To begin investigating the linearity of the detector, a basic fit is required. The fit that was computed for every pixel of the FPA was a linear least-squares fit of the linearity data.

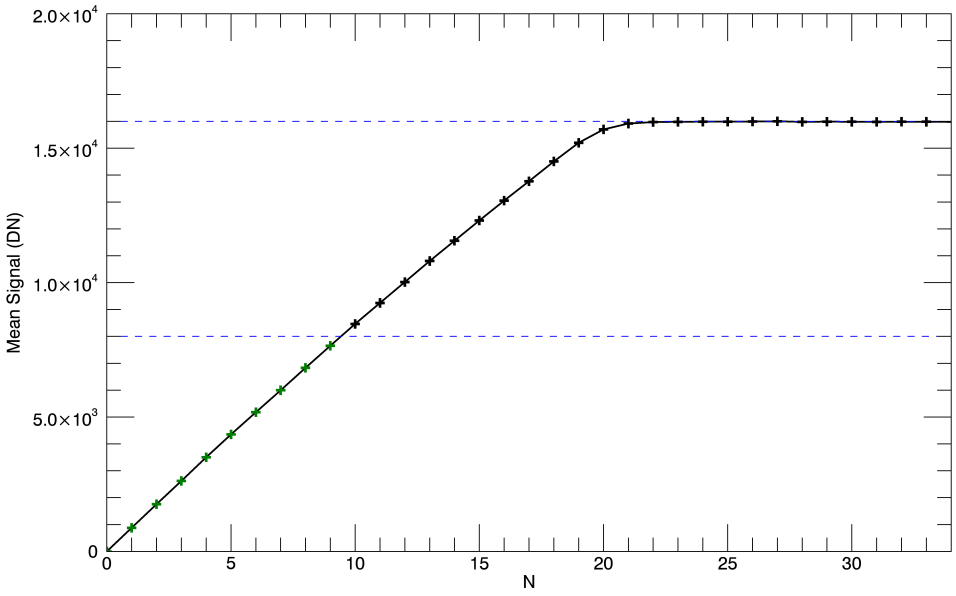

Figure 6.1: Linearity data for a typical pixel, 90K, Slow 100kHz

In Figure 6.1 the x-axis *N* represents factors of an arbitrary integration time selected to allow for sufficient resolution on the data. The number of points used was based on the saturation level observed for the pixel. Only points under 50% of the saturation level (dotted line) were used to compute the linear fit (green points in Figure 6.1).

Problem encountered

The first analysis made on the detector was to estimate the ratio of points that remained within the linearity constraints (±5%) with increasing integration times. The following figure describes the evolution of this ratio:

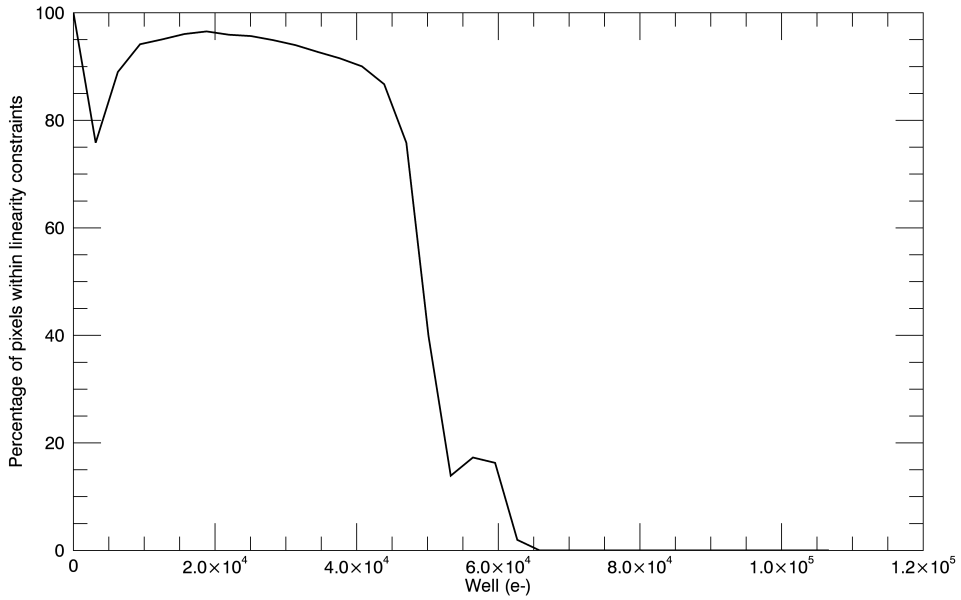

Figure 6.2: Percentage of linear pixel as a function of equivalent integration time

The well content is computed using the gain of the detector (e-/DN) and the initial slope of the mean value of the linearity data.

Figure 6.2 shows two unexpected dips in the percentage of pixels within the linearity constraints. The first "dip" takes place at the beginning of the well for $N = 2$. The second "dip" occurs when the well has already been significantly filled, around $N = 18$.

Pixels concerned by these two dips were investigated. The linearity data of pixels that breached the 5% constraints at these points were analyzed. Typically, the expected observations would be close to linear behavior for the first few points of the linearity data followed by a decrease in slope until saturation (concave data). This typical behavior is showcased in the figure below:

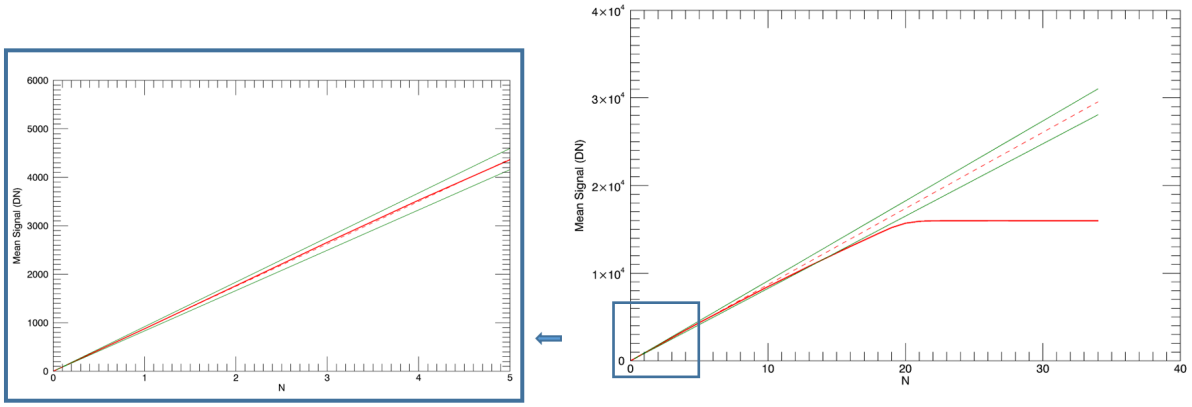

Figure 6.3: Standard Linearity

In figure 6.3, the red line is the actual linearity data, the dotted red line is the linear fit based on the linearity data, and the green lines represent the 5% limit for the deviation to linearity.

Type 1 of non-standard linearity

The first "dip" occurs for $N = 2$ in Figure 6.2. It shows that for several pixels (about 20%), the second value of the linearity data deviates from the linear fit by slightly more than 5%. However, the following value falls

back within the linearity constraints. The following plot highlights the increase in slope that occurs for a large number of pixels.

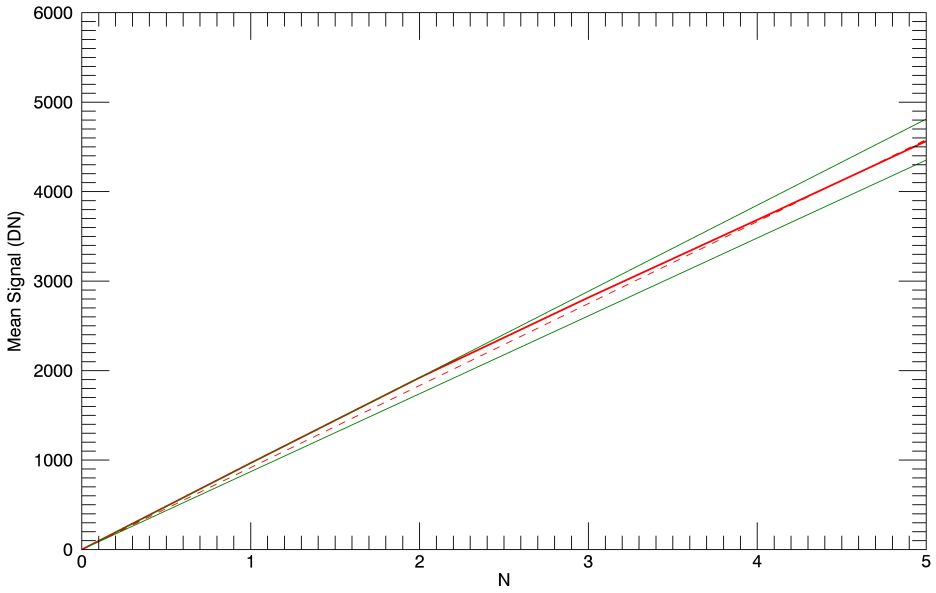

Figure 6.4: Flawed Linearity (Start of well)

Figure 6.4 shows that the linearity data (solid red line) crosses the 5% linear deviation limit (solid green line). For this pixel, the linearity-aspect of the operability constraints is breached. The data indicates that for a significant number of pixels the slope of the linearity data increases for $N = 2$.

There is a drop of about 20% in Figure 6.2. However, more than 20% of pixels show an increase in slope for $N = 2$ is higher. Indeed, any pixel for which the increase in slope is below the 5% deviation to linearity would not be registered in Figure 6.2. Therefore, they would not be included in the 20% of non-linear pixels causing the first dip in the figure.

Type 2 of non-standard linearity

The second type of non-standard linearity is responsible for the dip around $N = 18$ in Figure 6.2. Around 5% of pixels seem to be affected by this non-standard behavior. This effect occurs when the well is almost saturated. These non-standard pixels show a sudden increase in slope when the well is almost full. The following plot highlights the increase in slope that occurs for these pixels when the well is almost full:

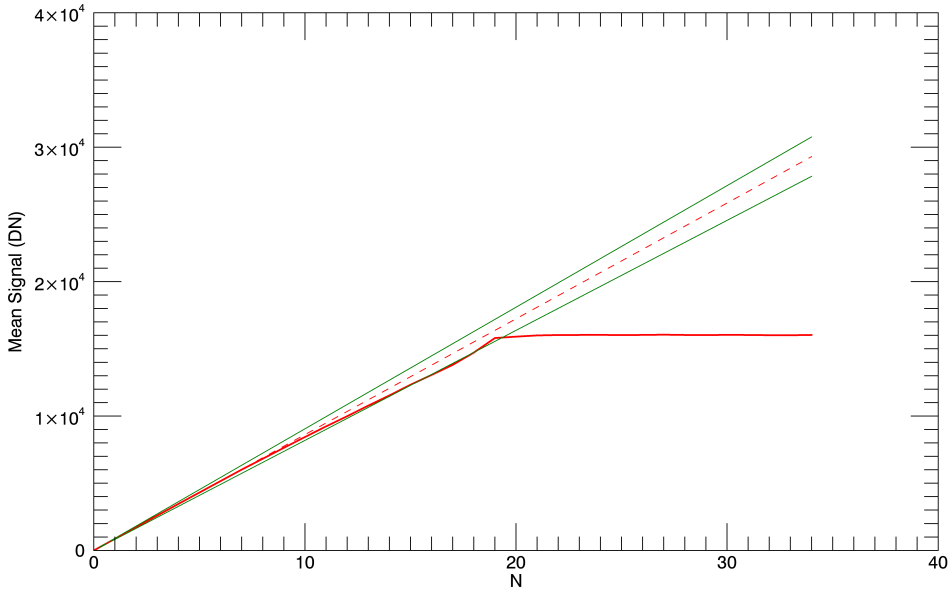

Figure 6.5: Flawed Linearity (End of well)

The previous figure shows the linearity data of a pixel where, initially, the slope decreases (nominal behavior). Then, when they get close to the saturation, the deviation to the linearity exceeds 5%. However, due to the sudden increase in slope, the deviation will go back within the limits for a few N. This causes the second dip around $N = 18$ in Figure 6.2.

6.3.2. Performance estimation - Updated linear fit

For practical reasons, it is much more useful to have a linear fit which allows the pixel to remain within the deviation to linearity constraints for as long as possible. If the variations w.r.t. the linear fit are small, the pixel will not be flagged as inoperable too rapidly. This would lead to a severe underestimation of the full-well capacity.

Due to the behaviors described in the previous section, the linear fit has been adapted. The algorithm to compute the linear fit is described below:

For each pixel, the measured linearity data is divided by its corresponding N value. The slope of the linear fit is, then, equal to the maximum of these values divided by 1.05. This fit ensures that the deviation to linearity remains below 5% for as much integration time as possible.

Using this linear fit the evolution of the ratio of pixels within the linearity constraints with increasing integration times is much closer to the initial expectations, as shown in the figure below:

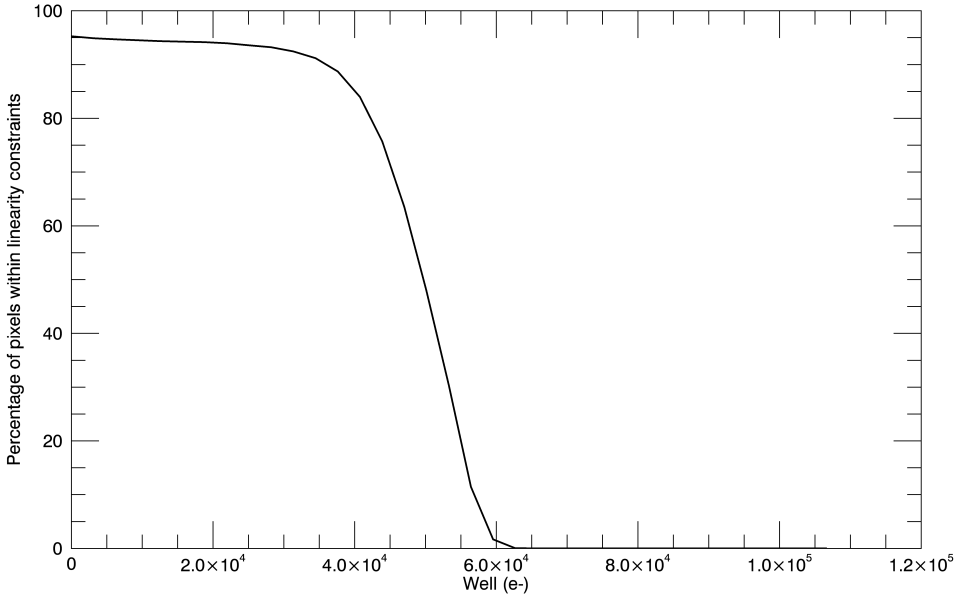

Figure 6.6: Ratio of pixels within linearity using the new fit

This figure shows that the two dips that occurred previously have been removed by the change in the type of linear fit used.

Based on the observations of this characterization campaign, the characterization of flight detectors' linearity should include fine resolution around the points of non-standard linearity observed. (Start of the well and close to saturation).

Furthermore, this confirms the importance of increasing the resolution of measurements when these non-standard behaviors occur, i.e. when the well is close to being empty or close to being full.

6.3.3. Consequences for the instrument in-flight

The analysis of the linearity measurements has shown diversity in the pixels' responses. A bad pixel in terms of linearity will generally be expected to show a very concave linear response. However, a significant amount of the pixels in the IR-EM detector have been shown to behave erratically. Significant nonlinearities can deteriorate the quality of the data.

The less linear the detector is, the more care has to be put in the analysis of images taken by the instrument. It also becomes harder to extrapolate and interpolate results based on the flat-field linearity normalization. The less linear a detector is, the more precise the characterization of the detector has to be. Furthermore, highly non-linear behavior in pixels can generally be an indicator of inoperable pixels [18].

The CDS noise measured on a given pixel of the detector is also significantly influenced by the linear response of this pixel. Indeed, the photon noise and dark noise are both affected by the local gain (see Section 4.4.2). The local gain will usually decrease with increasing electrons in the well. This decrease in local gain will decrease the impact of the photon noise and shot noise and increase the impact of the quantization noise.

6.4. Dark Current

The dark current is important to ensure that the well does not get filled too fast to optimize the SNR. The dark current is highly dependent on the temperature of the detector. Therefore, a full characterization of the detector has to include the full range of operational temperatures.

The dark current of the full FPA was estimated based on the peak value observed for the histogram of dark currents of all pixels. The following figures showcase different histograms of dark currents for the EM FPA at 84, 89 and 91K.

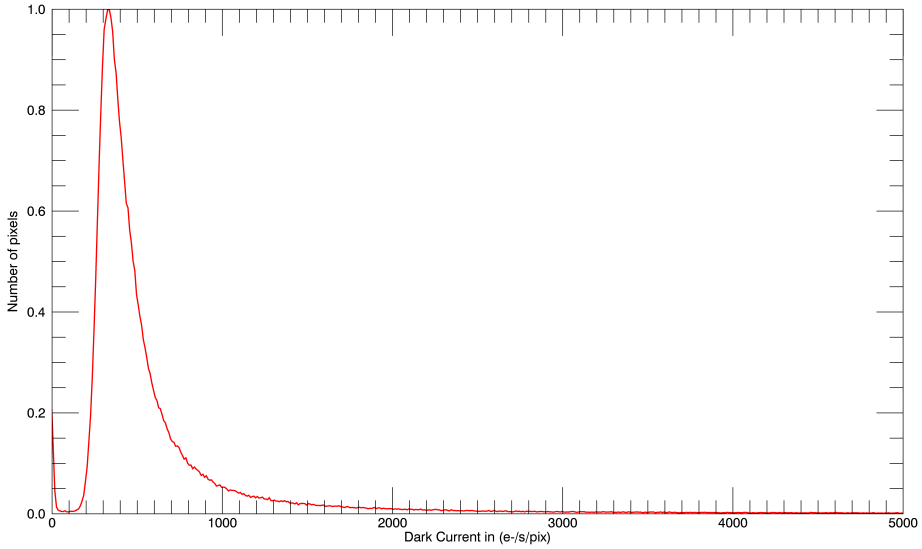

Figure 6.7: Dark Current Histogram 84K - Slow 100kHz - EM

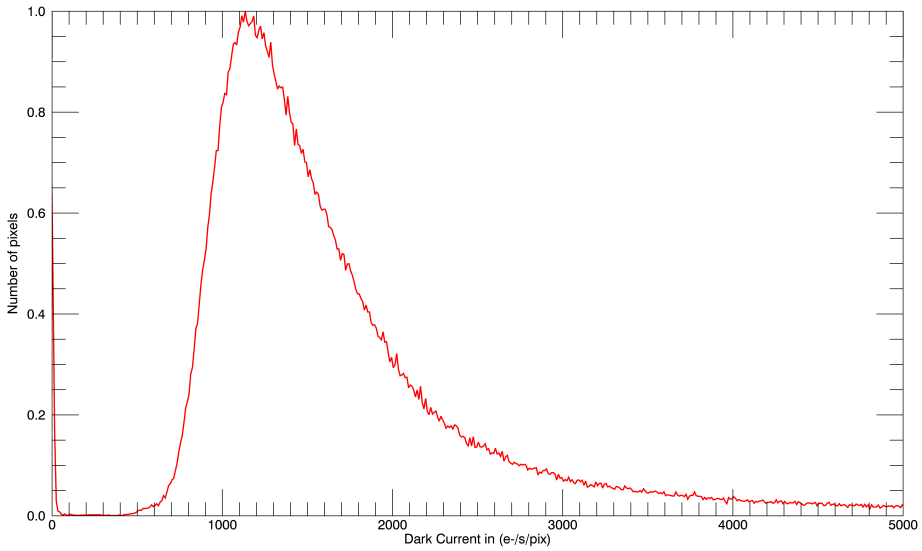

Figure 6.8: Dark Current Histogram 89K - Slow 100kHz - EM

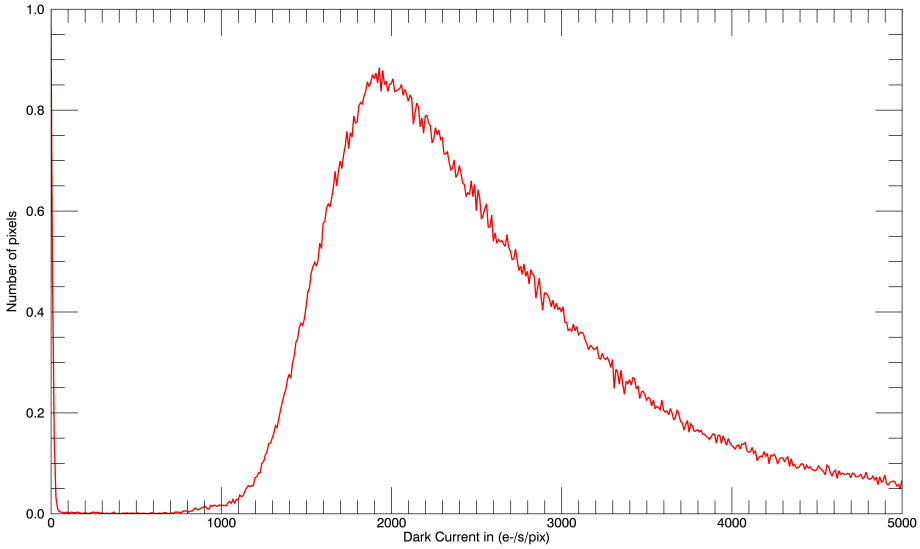

Figure 6.9: Dark Current Histogram 91K - Slow 100kHz - EM

Using the peak value instead of the mean or median value ensures that the value registered is representative of the behavior of the detector, i.e. this is the value representative of most of the nominal pixels of the detector. With this approach the dark currents were estimated at different temperatures within the nominal range. The following figure, shows the evolution of dark currents as a function of temperature for the Slow 100kHz:

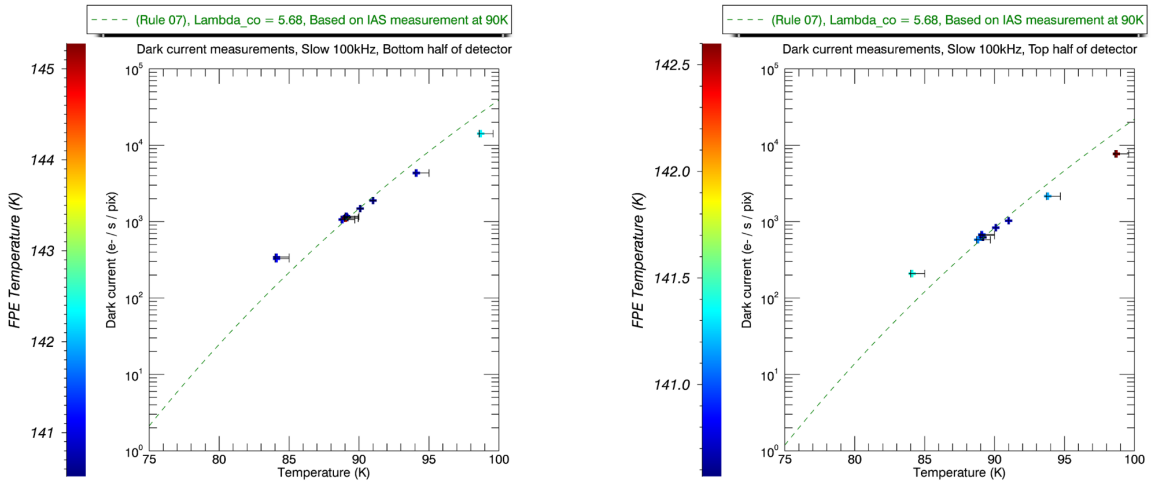

Figure 6.10: Dark Current - Slow 100kHz - EM

As expected, the dark current increases with increasing temperature. It was mentioned in previous Chapters that the empirical Rule 07 predicts the evolution of dark currents of HgCdTe photodiodes as a function of temperatures. For this detector, Rule 07 is applied with the equations and parameters given below [40]. (based on Equation (4.6), we have $\lambda_e = \lambda_{cutoff}$):

$$J = J_0 \, e^{C \frac{1.24q}{k\lambda_{cutoff} T}} \tag{6.1}$$

where:

Equation Parameter	Parameter Value	Unit
J_0	8367.00001853855	A/cm^2
λ_{cutoff} (50% of peak QE)	5.68	µm
λ_{scale}	0.200847413564122	µm
$\lambda_{threshold}$	4.63513642316149	µm
Pwr	0.544071281108481	
C	1.16239134096245	

Table 6.1: Parameters for Rule 07

However, in this case, the values reported by Rule 07 were far from the measurements. The green dotted line only takes into account the relative variations of dark current predicted by Rule 07 and uses as base value the dark current measured at 90K. This plot also displays the influence of FPE temperature based on the color of the points. Based on these measurements, the FPE temperature does not seem to have a significant impact on the dark current of the detector.

For this EM detector, Rule 07 is a bad predictor for the evolution of dark currents from an absolute perspective and still unsatisfying from a relative (green dotted line) perspective.

6.4.1. Consequences for the instrument in-flight

First, as was expected, the detector's temperature will greatly influence the performances of the detector in terms of dark current. As mentioned in previous chapters, the dark current will have a significant impact on the capacity to optimize the SNR. Based on the observational cases, the temperature of the instrument can increase significantly leading to deteriorated performances. This will be addressed in more detail in the study of observational cases in Chapter 8.

The nominal operating range of temperatures for the FPE is between 120 and 160K. The FPE temperature was shown to have no noticeable impact on the dark current in this range. The FPE temperature is affected by outside influences but will also increase significantly during a series of observations. As the measurements show no significant change in the dark current, the increase in temperature bound to happen with long uninterrupted series of observations is not expected to decrease the performances of the FPA.

6.5. Noise

Performance estimation - CDS Noise

As the signal due to dark currents increases with increasing temperature (see Chapter 4), the CDS noise also increases with increasing temperature (Equation (4.9)). The following figures showcase different histograms of CDS noises for the EM FPA at 84, 89 and 91K.

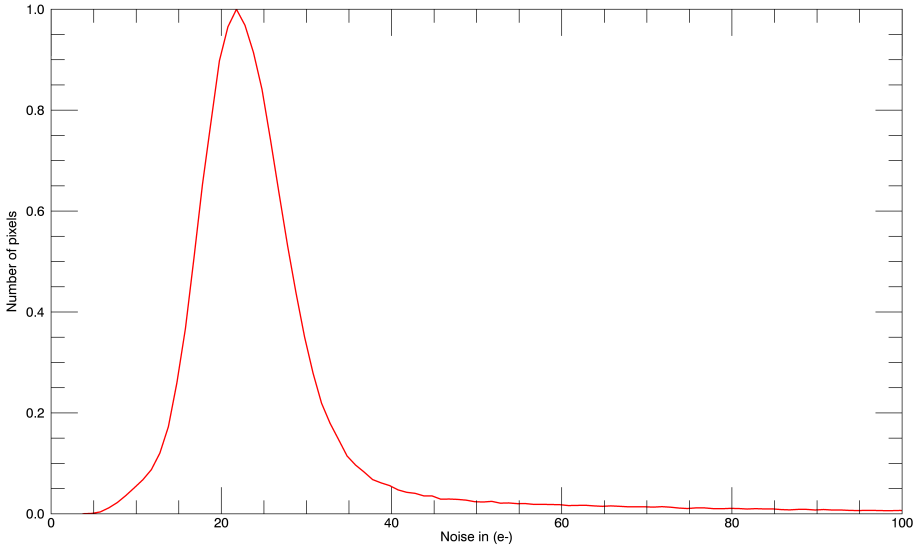

Figure 6.11: Noise Histogram 84K - Slow 100kHz - EM

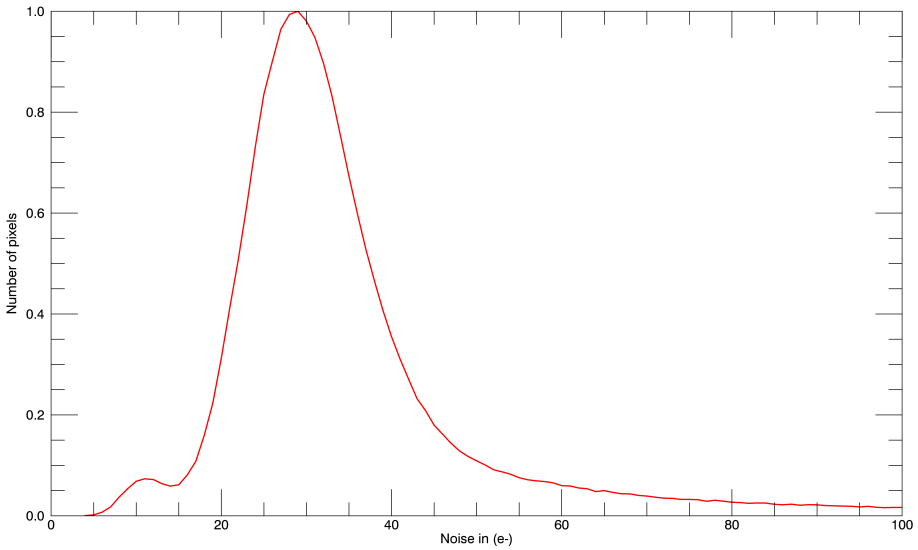

Figure 6.12: Noise Histogram 89K - Slow 100kHz - EM

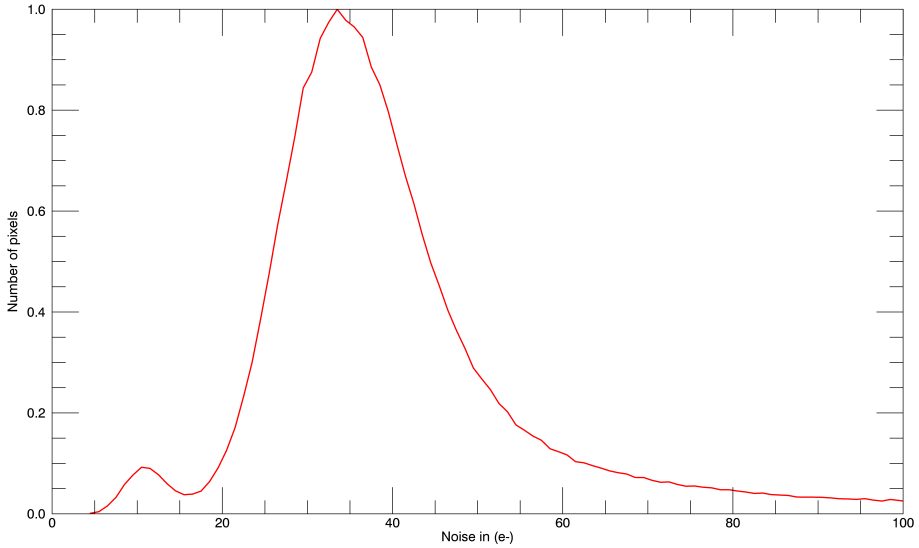

Figure 6.13: Noise Histogram 91K - Slow 100kHz - EM

Performance estimation - RON

Using the previously described methodology, the read-out noise for the EM detector was estimated at different FPA and FPE temperatures:

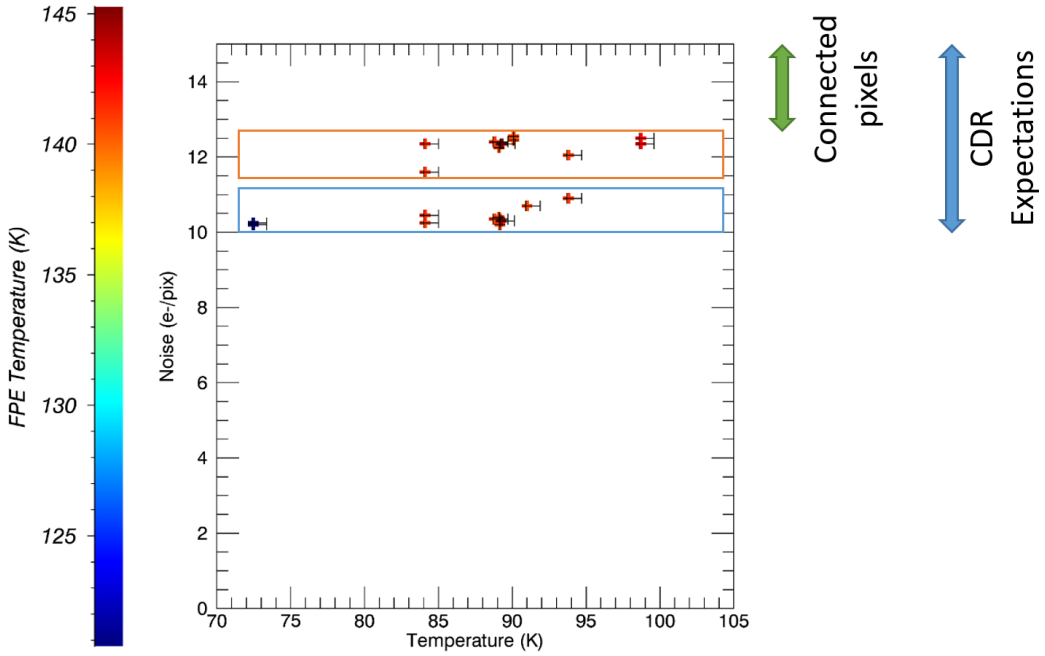

Figure 6.14: Read-out noise - Slow 100kHz - EM (Reference pixels)

Figure 6.14 highlights that, although the detector's temperature does not seem to impact the noise performances of the detector, the detector oscillates between two read-out noise levels from CDS image series to CDS image series. However, even with the higher noise level, the read-out noise remains within the range of expected noise performances. The connected pixels read-out noise estimations were not shown because,

due to their higher signal levels, the accuracy of the estimations were too low to distinguish between the two noise-levels. Based on all the read-out noise estimations, it appears that on a given series of images the read-out noise is constant across the entire array of connected pixels. (This also holds for reference pixels, but, the read-out noises are different between connected and reference.)

6.5.1. Consequences for the instrument in-flight

The noise model validation was described in Section 5.5. The read-out noise determines the lowest value of noise that can be observed. The read-out noise is particularly relevant for low signal observations (see Section 4.5.6). Low signal acquisitions will occur during the observations of the exosphere of the Galilean moons, and of the surfaces of those moons for some wavelengths (see Section 3.7). For these observations, the read-out noise will have a strong impact on the levels of SNR that can be reached.

6.6. Operability

For the EM IR campaign operability maps were built using the following parameters based on the specifications document established before the campaign:

- Dark Current < 7000 e-/s
- CDS Noise < 70 e-
- Quantum Efficiency > 35%

From these conditions, it follows that the operability of the FPA will significantly decrease with increasing temperatures. Currently, no QE tests have been performed at the IAS. The QE is a performance parameter unlikely to be significantly influenced by the temperature. To get an idea of the evolution of the operability with the temperature, operability tests were held using only the first two conditions. The following figures are operability maps of the EM detector at various temperatures using this subset of conditions. Red pixels signify a breach of the noise constraint and green pixels a breach of the dark current constraint, and yellow for both.

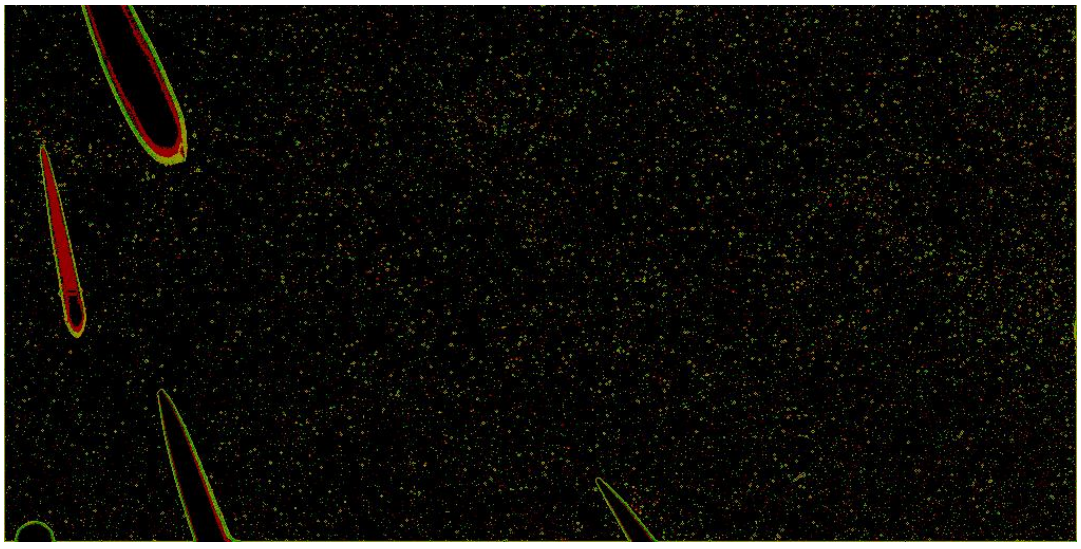

Figure 6.15: Operability map at 84K

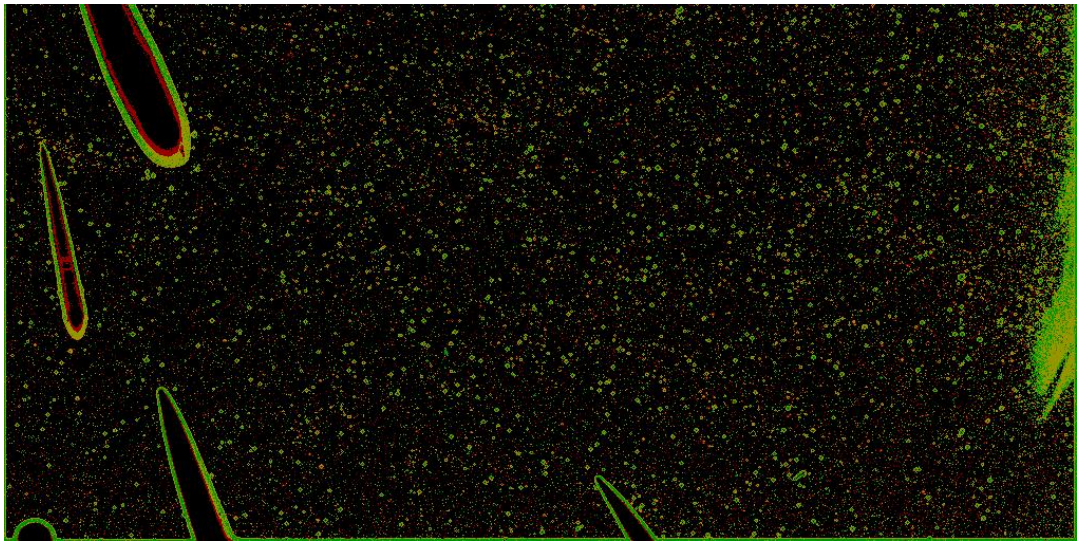

Figure 6.16: Operability map at 90K

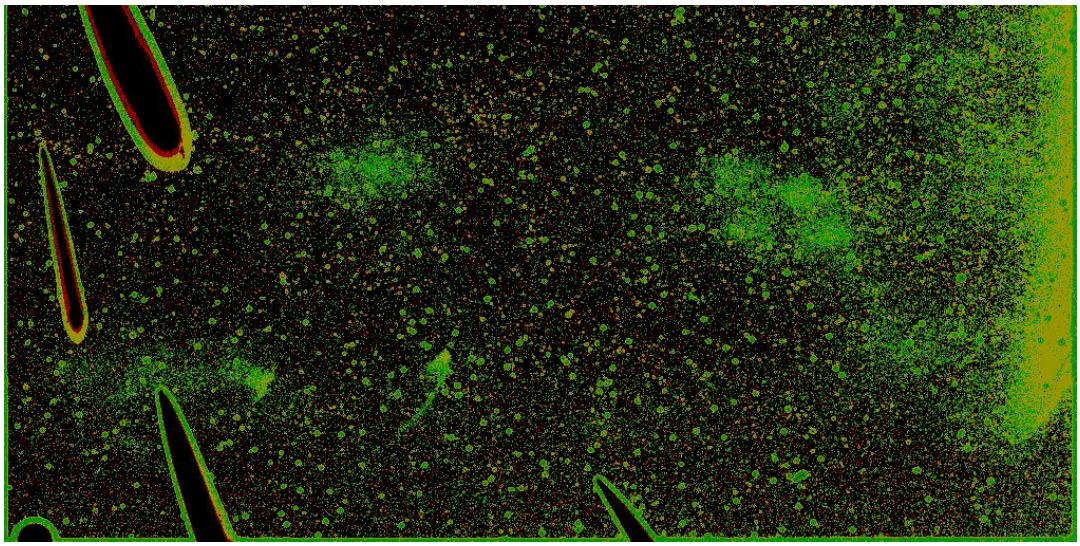

Figure 6.17: Operability map at 93K

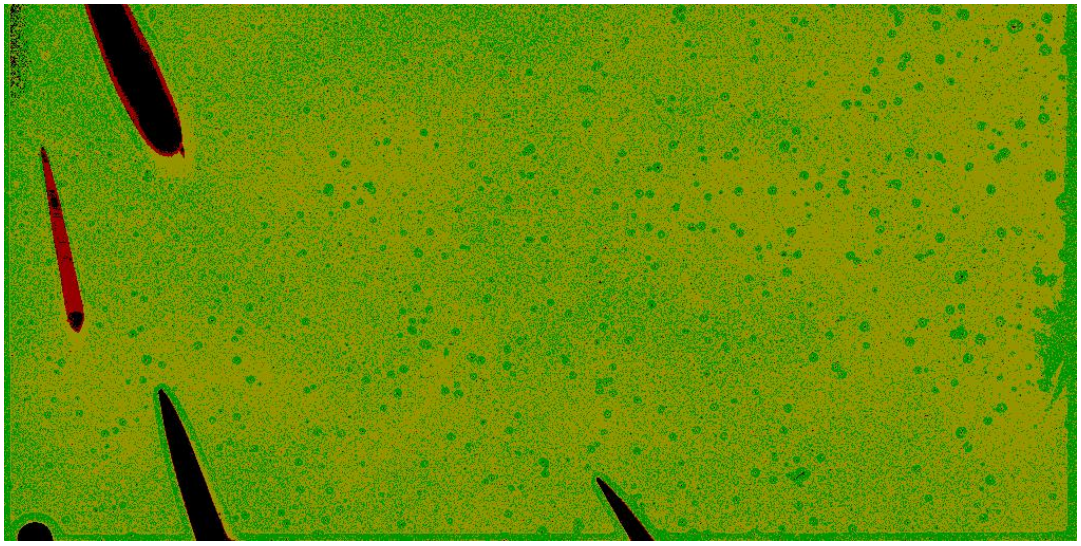

Figure 6.18: Operability map at 98K

These maps show that the operability constraints used do not address successfully the visible clusters of bad pixels. Pixels that in both frames of the CDS images (reset-read and read) are at the same value (dead or saturated), will appear to be operable even though they are useless. An additional constraint should be added to ensure that the pixels are still responsive.

Another aspect is that the constraint addressing the CDS noise should rather limit the read-out noise. Indeed, using the CDS noise instead of the read-out noise serves only to add a redundancy due to the link between the shot-noise and dark current (see Section 4.5.6). The updated operability constraints used were:

- Dark Current < 7000 e-/s
- **Read-out** Noise < 70 e- (see Chapter 5)
- *Quantum Efficiency > 35% (No QE measurements available to apply the constraint)*
- **Deviation to linearity < 5%**

The following map was established at 90K with the new constraints, red pixels signify a breach of the noise constraint, green pixels a breach of the dark current constraint, blue pixels a breach of the deviation to linearity constraint:

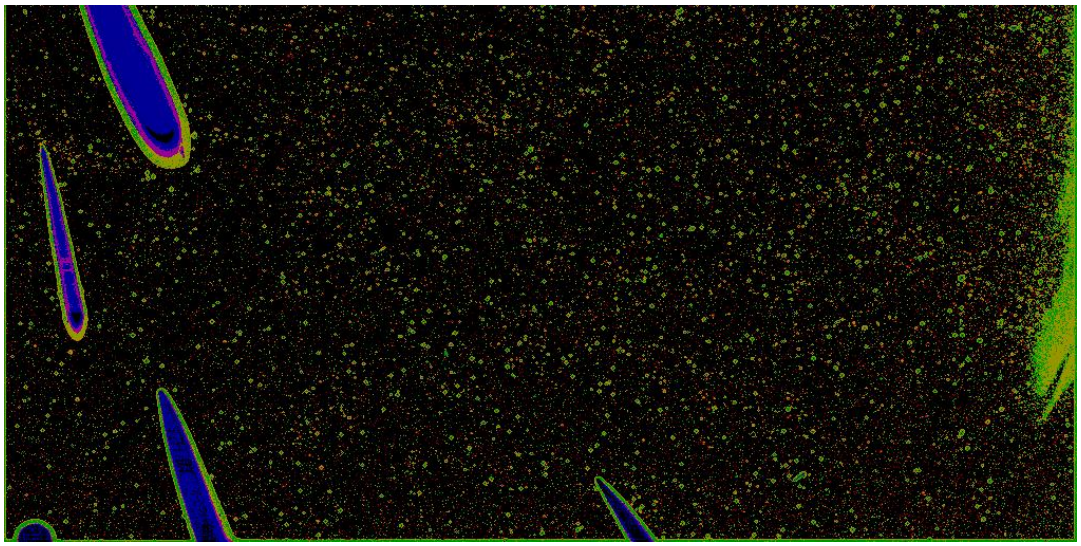

Figure 6.19: Operability map with updated constraints at 90K

This map shows that the linearity constraint (blue zones) correctly identifies the large defects on this detector. This map shows much better coverage of operability based on the cosmetic of this detector.

6.7. Performances summary

FPA T (K)	**FPE T**	**CDS noise (e-)**	**RON (REF) (e-)**	**DC (e-/s/pix)**	**Operability**
84.1	141	21	10	335	93.95
88.8	141	27	10	1066	
93.8	141	35	12	4336	65.81
98.7	142	61	12	14217	2.11
89.1	141	29	10	1169	88.13
90.08	141	32	12	1483	85.99
91	141	34	10	1883	83.46
89.16	141	29	10	1136	
72.4	121	28	10	N/A	N/A

Table 6.2: EM FPA Performances summary - Slow 100kHz

FPA T (K)	**FPE T**	**CDS noise (e-)**	**RON (REF) (e-)**	**DC (e-/s/pix)**
84.1	142	35	27	330
88.8	141		29	1155
93.8	142	41	29	4200
98.7	143	53	27	14920
89.1	141	38	27	1200
90	155	41	29	1140
72.4	121	35	29	N/A

Table 6.3: EM FPA Performances summary - Fast

6.8. Conclusion

It is difficult to eliminate all the stray-light on the IR FPA. However, subtraction of residual signal based on measurements at low temperatures makes evaluating the performances of the FPA possible.

Linearity is highly dependent on the linear fit used. A standard has been established on the method to be used for the computations of the linear fit. This new standard will be used during the FM FPA characterization campaign. The detector has displayed non-standard behaviors w.r.t. the linearity. Two main types of abnormal behaviors have been identified. During the FM FPA characterization campaign, specific analyses will be carried out to assess the presence of similar non-standard pixels.

As expected, dark currents increase with increasing temperature. However, the evolutions measured on the EM detector can not be accurately described by the Rule 07. The dark currents of the FM FPA are expected to follow the Rule 07 more closely.

The noise model appears to be well understood. The results are well in line with the theory. To confirm the uniformity of the read-out noise distribution, additional tests with the FM FPA should be conducted.

On the EM FPA, several bad clusters are present. These are not representative of the performances of the FM FPA. The operability of the FM FPA is expected to be higher than the operability measured on the EM. Area without cluster and stray-light (close to the center of the EM detector) are expected to be more representative of the FM FPA. As expected, the operability decreases significantly with increasing temperatures. Based on all measurements, it is expected that the main limiting factor at higher temperatures will be the dark current (Figure 6.18). At lower temperatures, the impact of all parameters is more comparable.

7

Results of EM VIS-NIR campaign

7.1. Introduction

This campaign was performed using the EM VIS-NIR detector of the MAJIS instrument. It was characterized to anticipate and prepare for the characterization of the flight model and spare detectors using the IASB facilities. This campaign covered both acquisition mode when it was feasible. This EM characterization will cover the following performance parameters:

- linearity
- dark current
- noise
- conversion gain
- quantum efficiency
- latency

Due to set-up and time constraints, measurements, during this campaign, were acquired only at an FPA temperature of 125K. The analysis of this campaign was performed using the data-reduction, methodology, and facilities presented in Chapter 5.

7.2. Stray light

7.2.1. Window closed - "Dark"

As the previous campaign has shown, it can be difficult to prevent stray light from reaching the detector. Considering that the detector used for this campaign covered the VIS-NIR range, thermal emissions were expected to have a lower impact.

To assess the level of stray light, images were captured. Configuration 1 (see Fig. 5.14), with the cold plate closed (no illumination coming from the integrating sphere), was used. The FPA temperature was 140K (nominal VIS-NIR temperature).

For this EM detector, the median dark current in these conditions was expected to be around 1100 e-/s/pix. The median signal measured on these images was around 2600 e-/s/pix.

It was concluded that this difference in signal could have two possible origins:

- **(1)** The removable cold plate temperature was too high, which induced stray light that added to the 1100e-/s/pix dark signal.
- **(2)** The signal was exclusively dark current, therefore, the dark current increased since last checked. (1 year ago)

To discriminate which of these two hypotheses was at the origin of the difference, the temperature of the FPA was lowered to 125K. The median signal measured on images at 125K was around 370 e-/s/pix.

Based on Chapter 4, a decrease in temperature would induce a decrease in dark current, which is coherent with **(2)**.

As the temperature of the removable cold plate in front of the detector was also affected by this decrease in temperature, **(1)** could also be valid with both the stray light and dark current being reduced.

The following figure shows profiles from two images captured at 125 and 140K (the 125K profile was multiplied by a 7.44 ratio to bring both profiles to the same scale):

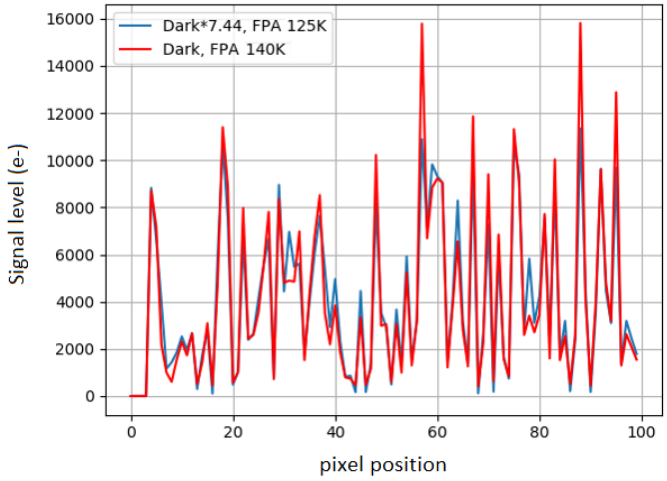

Figure 7.1: Profile comparison of two "dark" images taken with an FPA temperature of 140K and 125K

The full images are displayed in the figure below, with an adaptation of the scales used:

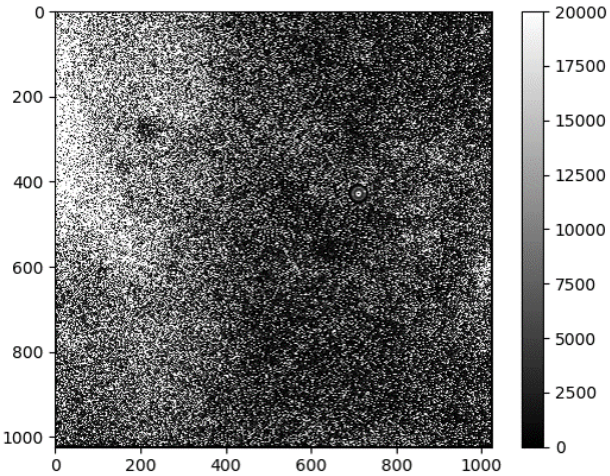

Figure 7.2: "Dark" image taken at 140K FPA temperature

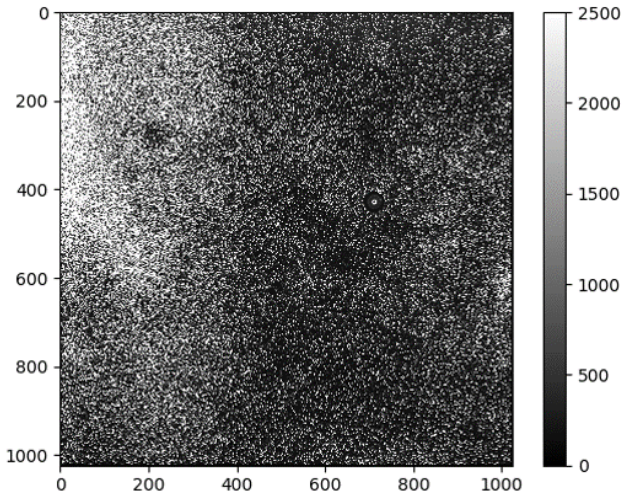

Figure 7.3: "Dark" image taken at 125K FPA temperature

These 3 figures show that the pattern of signal is the same when multiplied by a scaling factor. This would rather indicate that all the signal is due to the dark current. Indeed, it is unlikely that a completely homogeneous stray light would reach the detector.

Furthermore, the IASB provided a reference for the expected black-body emissions of the cold-plate reaching the detector based on their radiometric analysis of the set-up. The following figure describes the evolution of the stray light as a function of the temperature of the cold-plate:

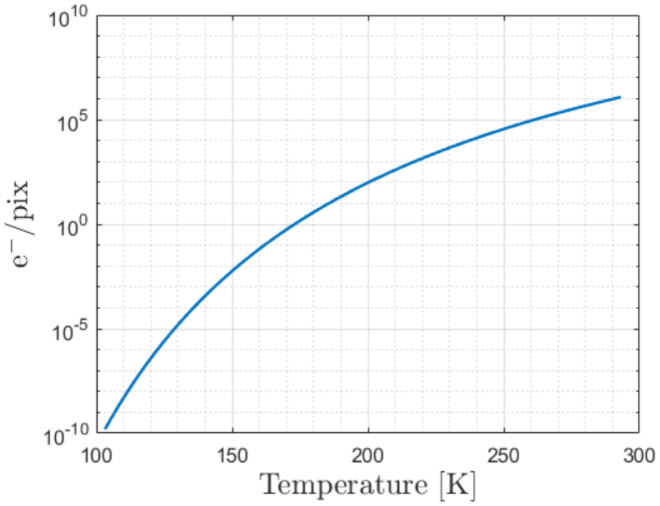

Figure 7.4: Black body emissions reaching the detector as a function of the cold-plate's temperature

The following table summarizes the impact of the black-body emissions for both configurations based on Figure 7.4:

FPA T (K)	**Cold-plate T (K)**	**Black-body emissions (e-/s/pix)**
140	196	80
125	189	20

Table 7.1: Expected stray light for both temperature configurations

Using the radiometric model presented in Figure 7.4, the stray light should be almost negligible for both

measurements. Based on the radiometry and the cosmetic of the images, it was concluded that the stray light in this set-up was marginal and that the dark had increased for unknown reasons.

7.2.2. Window open - Flux turned off - "Dark"

Another stray light test was performed with the window between the detector and the integrating sphere open. The flux was turned-off, based on initial radiometric modeling no flux should reach the detector.

In these conditions, the "dark" images were captured in full frame with minimum integration time (740 ms for the Slow 100kHz and 74 ms for the Fast). For both acquisition modes and both integration times, the "dark" images were saturated. After making revisions to the radiometric model, it appeared that the black-body emissions from the integrating sphere (which was at room temperature) were saturating the detector.

To determine whether images could be captured without reaching saturation, an SWPF was placed inside the vacuum chamber right in front of the detector. This SWPF was expected to reduce the flux coming from the window to the wavelengths 1.0-1.6 µm. For these wavelengths, the radiometric model predicted that all the black-body emissions would be filtered out.

The following image is an example of an image taken with the SWPF in front of the detector:

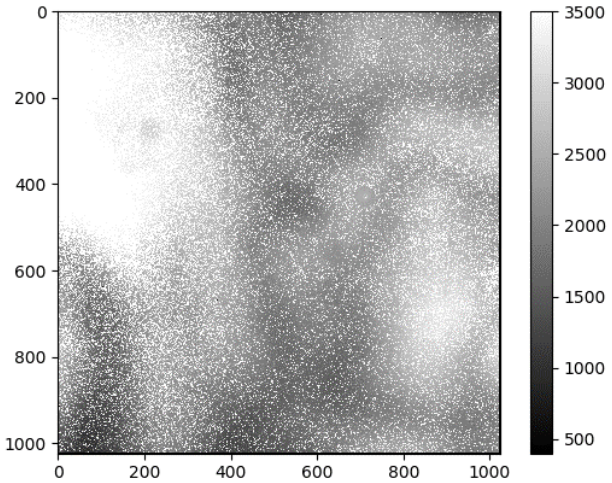

Figure 7.5: Open window with SWPF filtering black-body emissions (125K FPA temperature)

The median flux measured on images with the SWPF in front of the detector was around 2500 e-/s/pix, which was larger than the dark current measured when the window was closed. This meant that some of the black-body emissions got through the SWPF.

The following table summarizes the stray light and dark current observations:

	DC (closed)	**DC + BB (open)**	**DC + BB + SWPF (open)**
Median flux (e-/s/pix)	370	N/A (SATURATION)	2,500

Table 7.2: Stray light and dark current measurements

While the SWPF significantly improves the situation, issues remain. As mentioned, the band-pass of the SWPF is 1-1.6 µm. This precludes from exploring the whole desired wavelength range of 0.5-2.35 µm.

To capture images using the whole wavelength range, another approach was designed. Using the windowing microcode, it is possible to reduce the minimum integration time by reducing the number of rows taken.

Integration time (ms)	5	9	18	37	74
Number of rows	64	128	256	512	1024
Median flux (e-/pix)	7,500	14,500	28,200	54,500	65,000

Table 7.3: Median flux as a function of windowing and integration time without SWPF

Based on the previous table, it can be noticed that saturation can be avoided using smaller windows and integration times. Although this approach allows for measurements to be made using all desired wavelengths, this is limiting in terms of the variety of parameters that can be changed. Using 18 ms integration times, less than half of the well is filled by black-body emissions.

7.3. Dark Current

The dark current is estimated by analyzing the signal levels observed on CDS images acquired without incoming flux (see Section 5.8).

7.3.1. Performance estimation

The dark current had to be indirectly assessed to validate the stray light levels. Therefore, based on the previously mentioned measurements, the dark was estimated at two FPA temperatures (140K and 125K). At 140K, the peak dark current was around 2,600 e-/s/pix (see Figure 7.2). At 125K, the peak dark current was around 370 e-/s/pix (see Figure 7.3).

7.3.2. Consequences for the instrument in-flight

Although the dark current estimated from this campaign is higher than expected, the measurements were performed on an engineering grade model. This model has significantly worse expected performances than the flight model. Therefore, the absolute value of the dark estimated in this section does not change the expectations for the FM.

A similar kind of increase in dark current to the one observed in this section would be problematic for the flight detectors. The VIS-NIR FM detector would not be affected significantly by such an increase as its expected dark values are almost negligible for MAJIS observations (<10 e-/s at 140K). However, variations in dark current for the IR flight detectors could hinder the performances of the MAJIS instrument for the associated wavelengths.

This kind of evolution is not unheard of for HxRG detectors [6]. Based on observations made during the development of the JWST project, an increase in dark current after storage was noticed for H2RG detectors. However, following this project all new HxRG detectors (after 2012) have been produced using the “bake-stable” process [6]. The JWST reliability improvement program confirmed that this process resolved the issue [6].

No additional consequences other than the one presented in Chapter 6, have been derived based on the analysis of this campaign.

7.4. Read-out Noise

The read-out noise for the EM VIS-NIR detector was estimated for both acquisition modes at an FPA temperature of 125K.

7.4.1. Performance estimation

The RON is estimated by isolating several pixels with low signal on a series of images (see Section 5.5.3). This low signal ensures that the RON is a dominating factor in the noise model (see Eq. 4.9).

The following figure illustrates the estimated RON for the Slow 100kHz. Blue points represent a single pixel. The coordinates associated with a pixel are given by the measured signal and CDS noise. The green points are the ones being used to estimate the RON (low signal and low shot noise). The red line describes the theoretical noise model for a RON of 19 e-/pix.

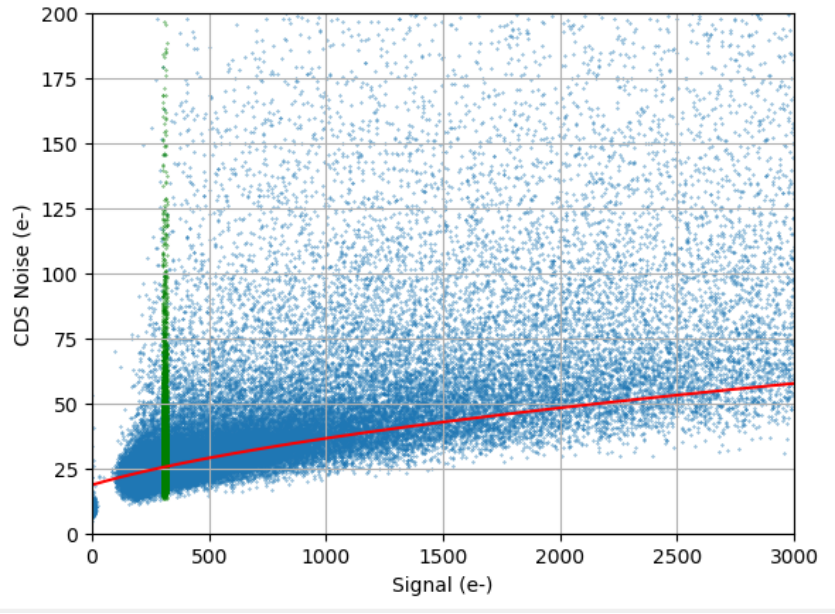

Figure 7.6: Read-out noise model - Slow 100kHz - EM VIS-NIR - FPA 125K

The following figure illustrates the estimated RON for the Fast. The red line describes the theoretical noise model for a RON of 32 e-/pix.

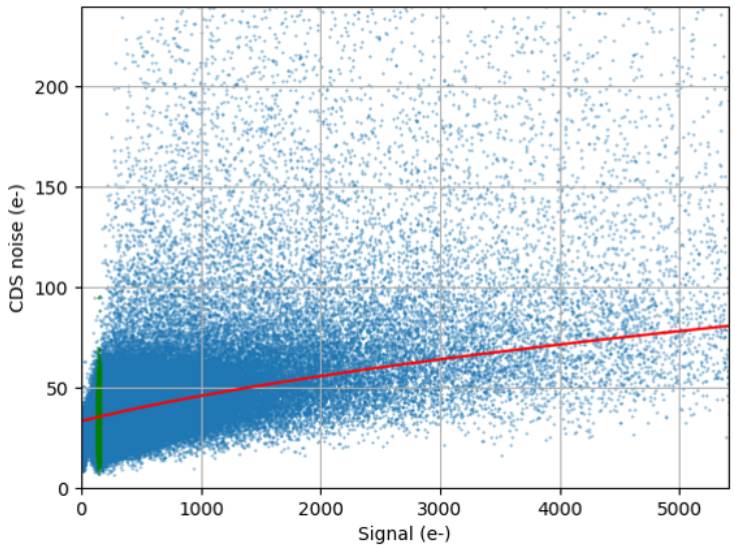

Figure 7.7: Read-out noise model - Fast - EM VIS-NIR - FPA 125K

These RON values are consistent with the expected performances of the detector based on the performances reported by TIS and the literature [5]. In addition, the measured CDS noises (blue points) show a good match with the theoretical noise model (red-line). This validates that the noise model presented in Section 4.5.6 describes accurately the evolution of the CDS noise as a function of the measured signal.

7.4.2. Consequences for the instrument in-flight

Based on this analysis, the expected consequences are the same as the one mentioned for the EM IR campaign. The read-out noise will mainly have an impact on the expected SNR for low-signal observations. (Due

to the short integration times, many observations will have relatively low signal compared to the read-out noises, see Section 3.7)

7.5. Linearity

For this campaign, the linearity was explored using both acquisition modes. The approach described in Section 5.2 as linearity in charge was used. The linearity was explored using increasing integration times using a constant flux.

7.5.1. Fast

This first figure describes the evolution of the mean signal for increasing integration times for pixels selected in a cosmetically good looking area of the detector:

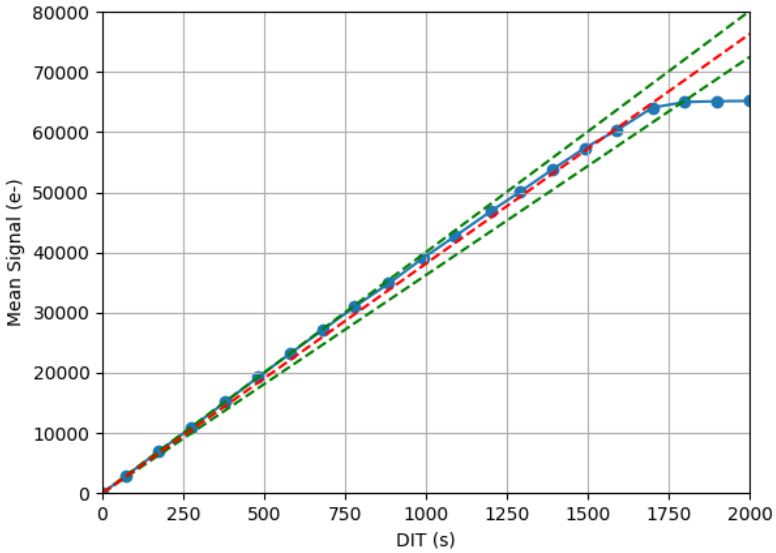

Figure 7.8: Mean linearity data for nominal pixels - EM-VIS-NIR - Fast

This figure uses the same linearity data as the previous figure and displays the deviation to the linear fit:

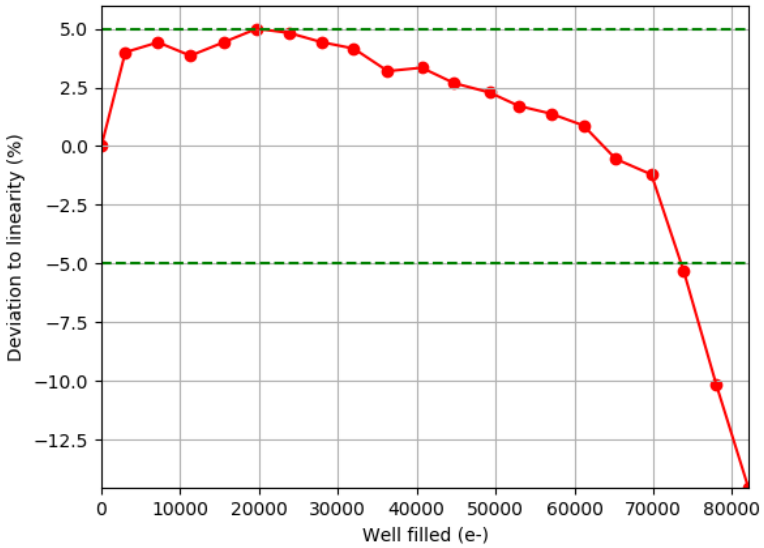

Figure 7.9: Mean deviation to linearity for nominal pixels - EM-VIS-NIR - Fast

The general behavior of the mean value for these nominal pixels is expected to be representative of the general performances of the flight detector. It shows a relatively good linear response with no significantly noticeable abnormality, up until the FWC is reached around 64,000 e-.

It is, however, noted that the biases used for the Fast microcode (which were not designed for the EM VIS-NIR FPA) were not optimal. A digital saturation was reached before the detector saturated its well. The figure below displays a raw read image (before CDS) almost entirely digitally saturated at 12 bits (4096) acquired with an integration time of 1.9s:

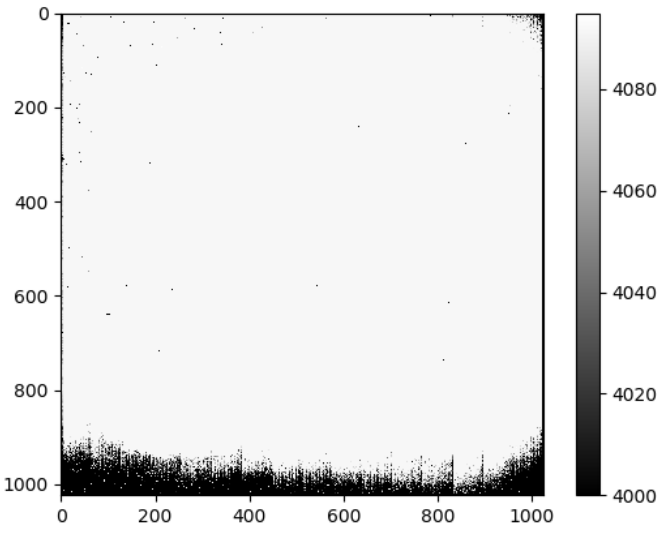

Figure 7.10: Saturated raw read - EM-VIS-NIR - Fast

Therefore, the linearity data has been truncated toward the end. The full well capacity of the FPA is, thus, higher than what will be estimated based on this data.

The following figure display the evolution of pixels breaking the 5% deviation to linearity as a function of how much there well is filled:

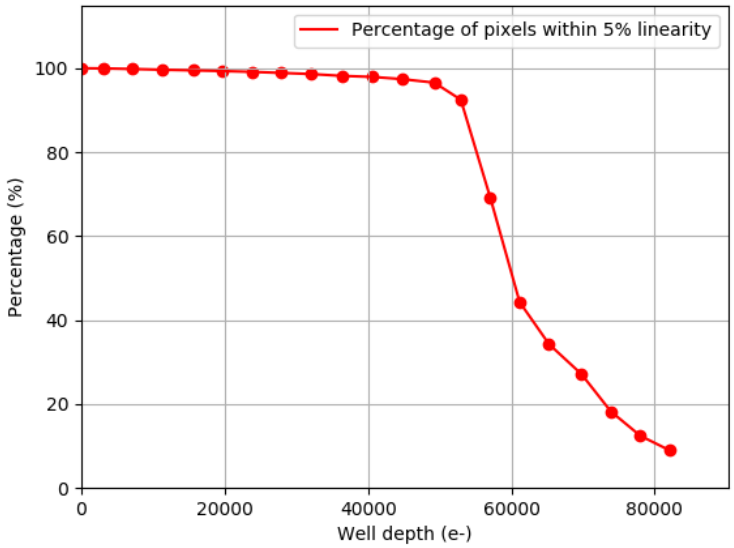

Figure 7.11: Percentage of pixels within 5% deviation- EM-VIS-NIR - Fast

This figure indicates that almost all pixels have a good linear behavior (<5% deviation) up until 50,000 e-.

7.5.2. Slow

The same approach has been used to analyze the data in the Slow acquisition mode. This figure describes the evolution of the mean signal for increasing integration times. The pixels were selected in a cosmetically good looking area of the detector:

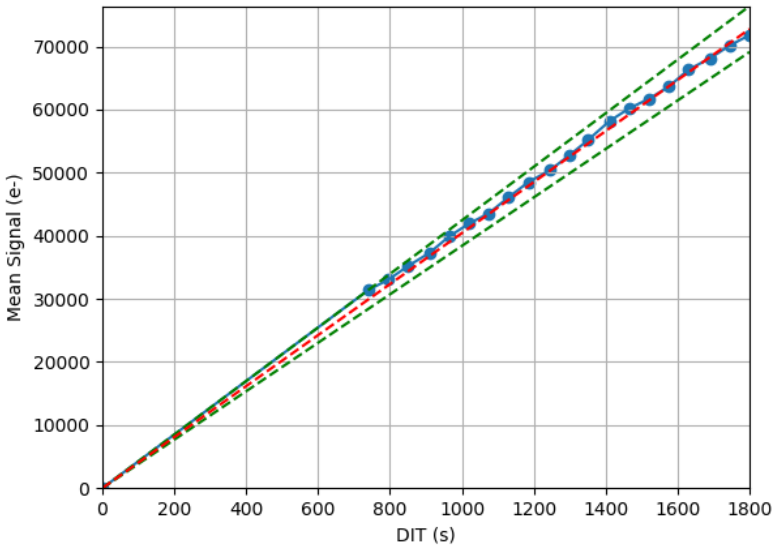

Figure 7.12: Mean linearity data for nominal pixels - EM-VIS-NIR - Slow 100kHz

This figure uses the same linearity data as the previous figure and displays the deviation to the linear fit:

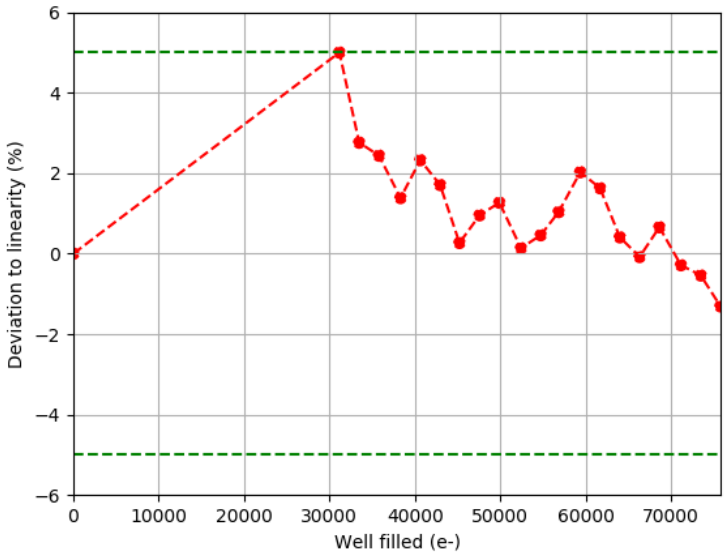

Figure 7.13: Mean linearity data for nominal pixels - EM-VIS-NIR - Slow 100kHz

There is a strong difference between the two acquisition modes. The Slow linearity data show a significant amount of jitters from one measurement to the next. The validation of the microcode has confirmed that this behavior is not due to the acquisition mode. Based on the observations of these jitters, further analyses of the set-up were conducted by the IASB. It is likely that the lamp was not stable during these measurements which lead to errors in measurements responsible for the jitter in the previous figures. The general behavior of the mean value is hard to assess because of these errors.

Unlike for the Fast, the biases used with the microcode allowed the linearity data to not get digitally saturated at 65,000 e-. However, the measurements did not reach the well saturation either leaving the full-well depth not estimated.

The following figure displays the evolution of pixels breaking the 5% deviation to linearity as a function of how much their well is filled:

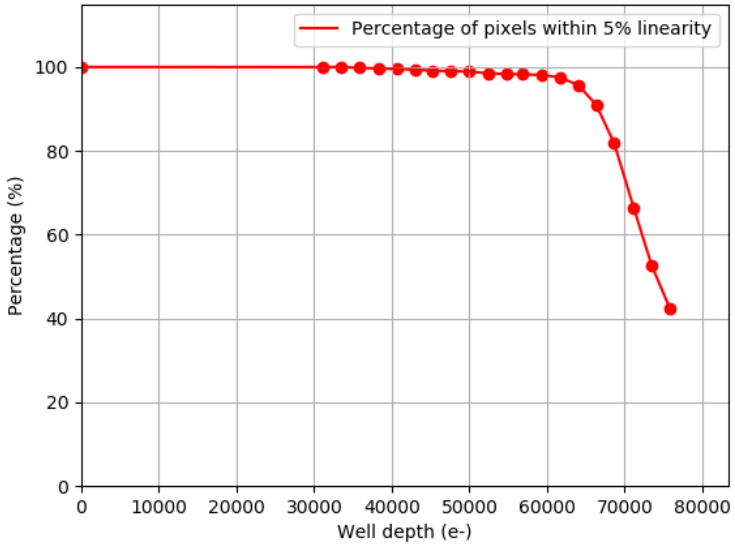

Figure 7.14: Percentage of pixels within 5% deviation- EM-VIS-NIR - Slow 100kHz

Although the data is not completely accurate, this figure indicates that almost all pixels have a good linear behavior (<5% deviation) up until 60,000 e-. No noticeable non-standard anomalies have been shown by the VIS-NIR detector.

It will be important for the characterization of the flight detectors to improve the stability of the lamp and to use more sensors to monitor the radiometry.

7.5.3. Consequences for the instrument in-flight

Although the campaign linearity measurements were not completely successful, the EM VIS-NIR has displayed performances that are not alarming for the flight detectors. Overall no new consequences, have appeared following this campaign.

7.6. Conversion gain

Based on the performances of the detector (reference pixels RON and FWC) the conversion gain was approximated to be around 2.0 e-/DN. To validate that the gain approximation was legitimate, the more rigorous methodology described in Section 5.6 was applied to the Fast linearity data acquired during this campaign.

7.6.1. Performance estimation

To sample the data, pixels which reported similar signal (1 DN around the median signal) were selected. The reported signal of those pixels was then plotted against the square of the CDS noise in the following figure:

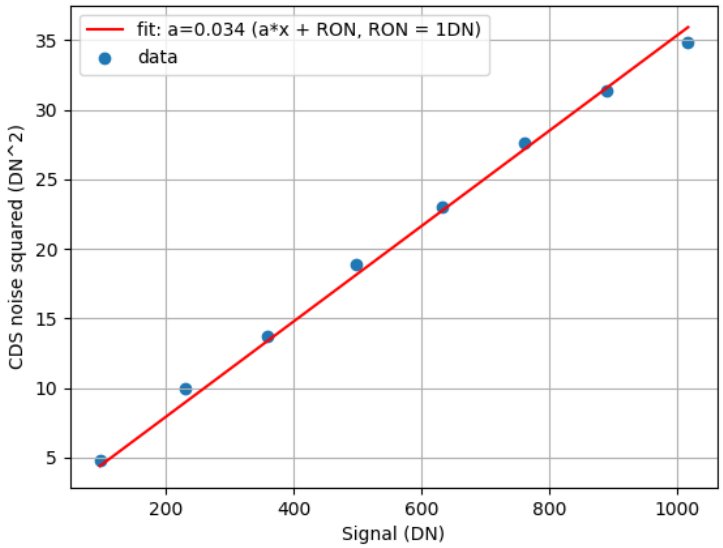

Figure 7.15: Estimation of the gain a (DN/e-)- EM-VIS-NIR - Fast

From this figure, the e-/DN gain $\frac{1}{a}$ can be estimated to be around 1.9 e-/DN, which is well in line with the previous rough approximation of the gain.

7.6.2. Consequences for the instrument in-flight

The gain enters into play for all measurements that the MAJIS instrument will perform. Once it has been accurately characterized, however, the impact on the instrument is mainly limited to its contribution to the quantization noise.

7.7. Quantum efficiency

The quantum efficiency is an essential aspect of the analysis of in-flight measurements and, therefore, an important aspect of the characterization campaigns. The quantum efficiency measurements require a good

knowledge and monitoring of the radiometry of the set-up as the incoming flux has to be known for every pixel.

7.7.1. Performance estimation

As mentioned previously in Section 7.2, the QE measurements are affected by the unexpected black-body emissions of the set-up. Due to these black-body emissions, only the Fast could be used for the QE measurements. No QE measurements were performed with the Slow 100kHz. However, it is unlikely that the acquisition mode has a significant influence on the FPA's QE.

To compute the QE a dark subtraction is required. However, in this case, the subtraction will include both the dark and the stray light (full background subtraction). These background CDS images will be different depending on whether the SWPF is in front of the detector or not. The following figures displays two background images. First, an unfiltered background image:

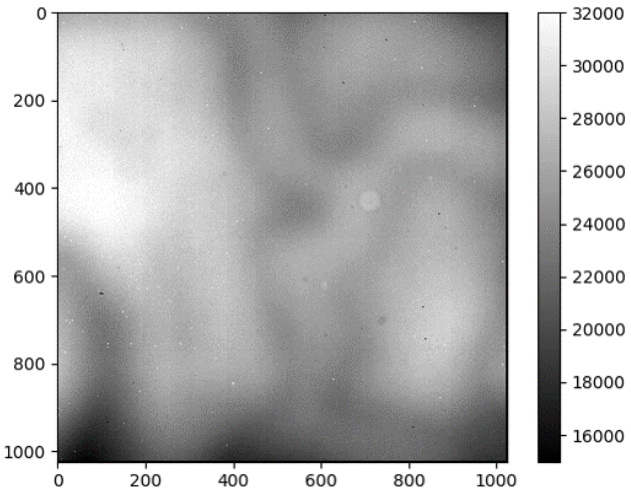

Figure 7.16: Open window without SWPF, unfiltered black-body emissions (125K FPA temperature) - Fast - 18ms DIT

As it was noted in the stray light section, to reach low enough integration times (for the detector not to be saturated), the images have to be captured using only 256 rows. Therefore, the image displayed previously is a mosaic of 4 independent captures stuck together (Figure 7.16).

The following figure shows a background image with black-body emissions filtered by the SWPF:

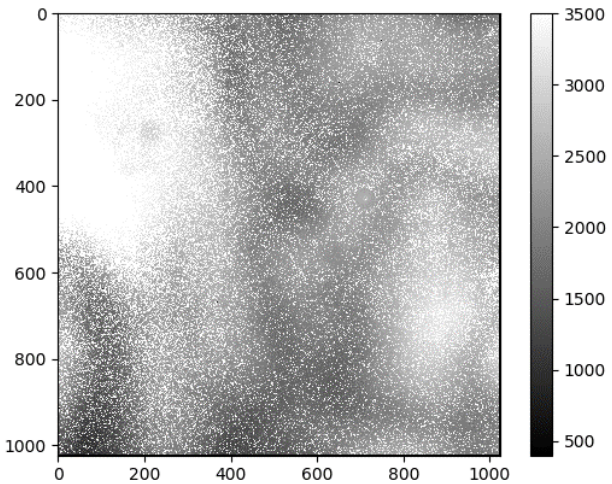

Figure 7.17: Open window with SWPF filtering black-body emissions (125K FPA temperature) - Fast - 1s DIT

For wavelengths, between 1.0 and 1.6 μm, an SWPF filtered background will be subtracted. For other wavelengths, an unfiltered background is subtracted.

Starting with the SWPF images, the following figures display on the left the QE for each pixel of the array on a suitable scale and on the right the histogram of the QE estimations. The wavelengths are 1000, 1230, and 1500 nm:

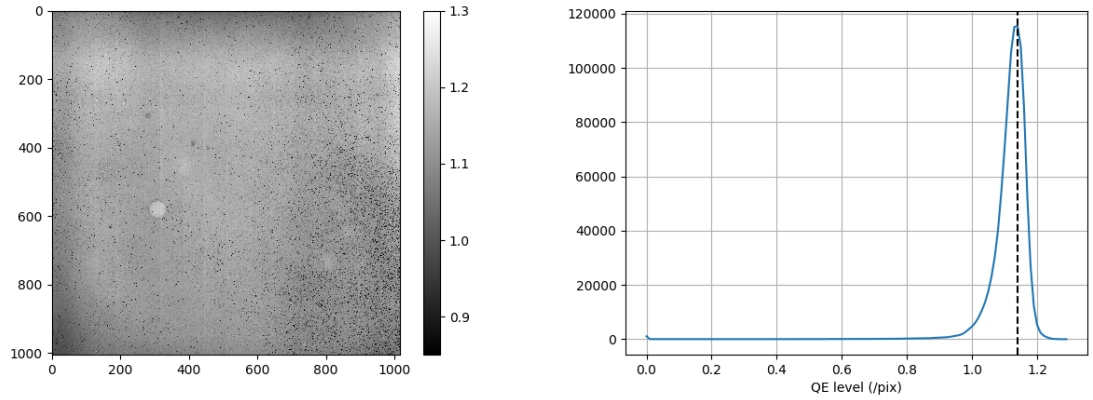

(a) 1000nm QE image

(b) 1000nm QE histogram

Figure 7.18: 1000nm QE

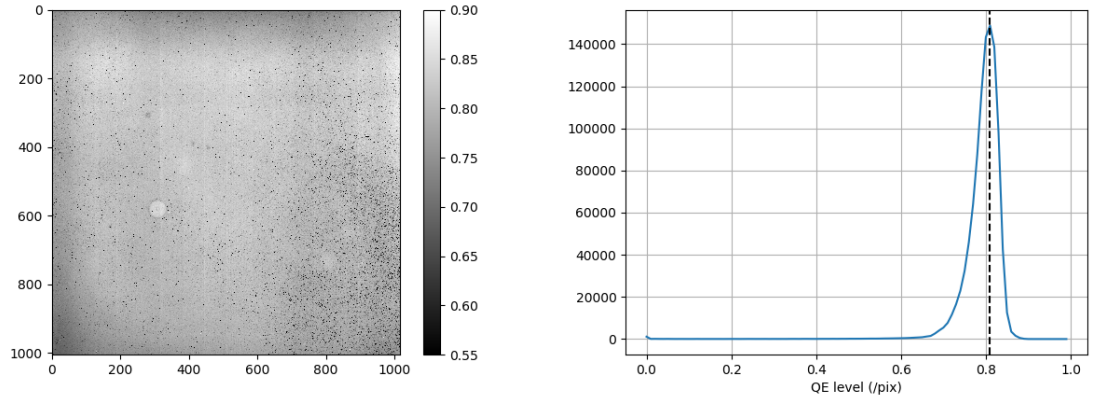

(a) 1230nm QE image

(b) 1230nm QE histogram

Figure 7.19: 1230nm QE

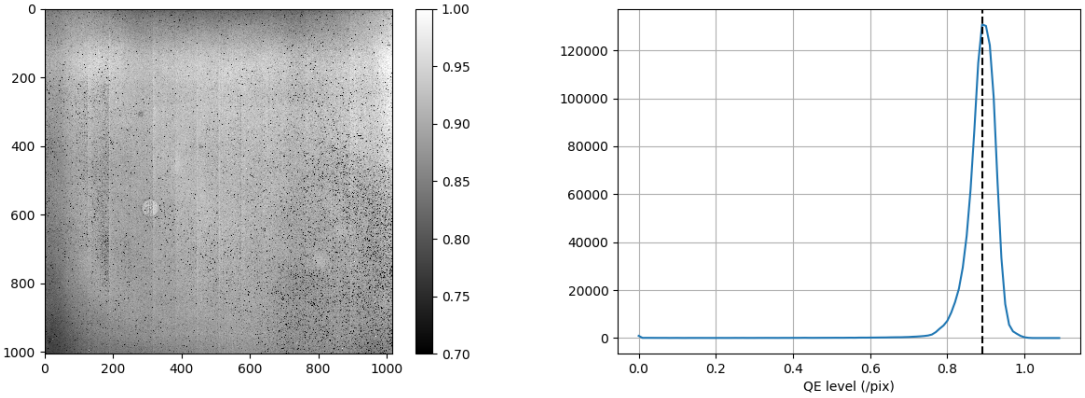

(a) 1500nm QE image

(b) 1500nm QE histogram

Figure 7.20: 1500nm QE

Figure 7.18 show that the radiometry is not reliable. Although the magnitudes of the estimations are right, the QE is expected to be around 0.7-0.8. Some of the measurements are about 50% too high, even exceeding the 1.0 theoretical limit.

The measurements without the SWPF, are mosaic of four 256 rows independent measurements. This explains the slight offset which can be visible between 256 rows for a same wavelength. The wavelengths used are 800, 2000, and 2350 nm:

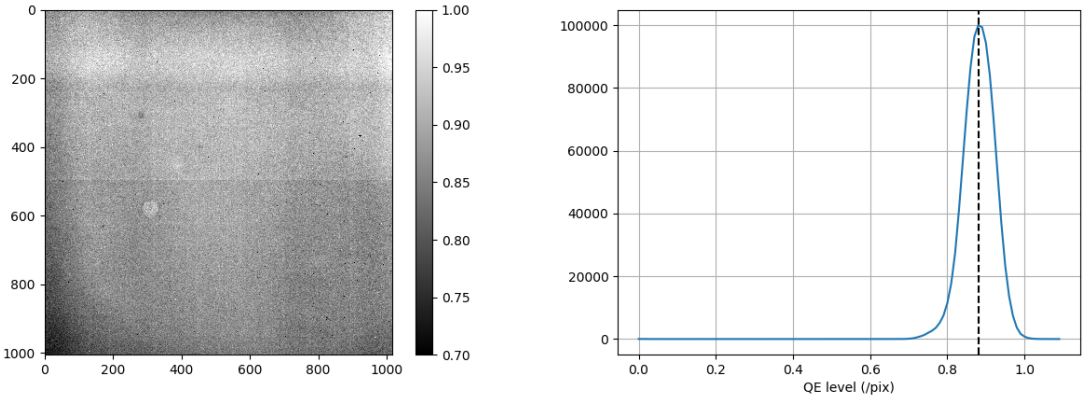

(a) 800nm QE image

(b) 800nm QE histogram

Figure 7.21: 800nm QE

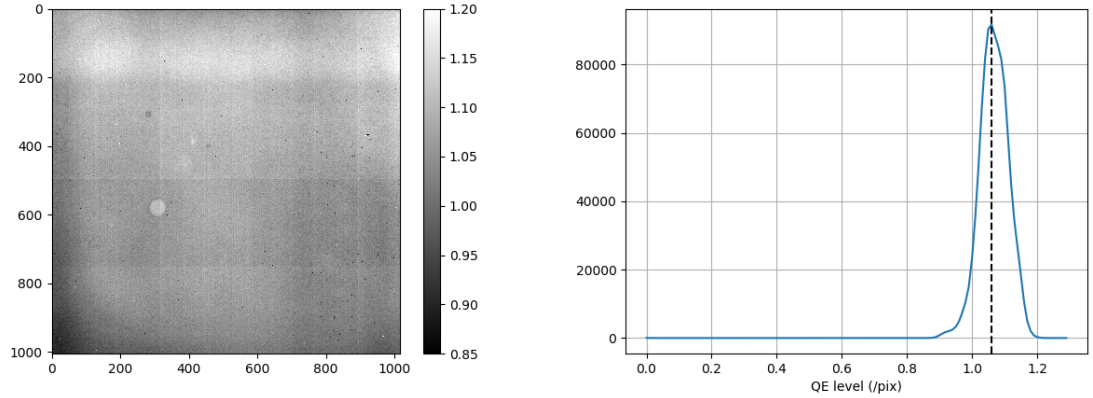

(a) 2000nm QE image

(b) 2000nm QE histogram

Figure 7.22: 2000nm QE

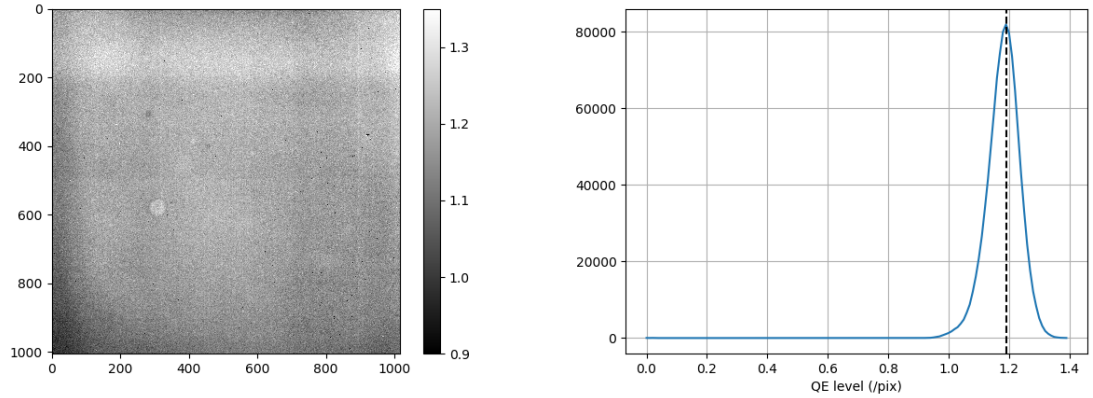

(a) 2350nm QE image

(b) 2350nm QE histogram

Figure 7.23: 2350nm QE

Even with the important black-body emissions, the magnitude of the QE measurements is still correct. However, the radiometric error seen in Figure 7.18 is also visible on some of these measurements. The QE is too high for Figure 7.22 and Figure 7.23 with errors reaching about 50% of the expected value. Based on these measurements it appears that the set-up for the radiometry does not allow for a reliable estimation of the QE.

This highlights the improvements that will have to be made for the flight model campaigns to ensure that the detectors can be characterized successfully.

7.7.2. Consequences for the instrument in-flight

The QE is an essential performance parameter of the detector for in-flight observations. The QE enters into account for all observation as it determines the levels of signal the detector will measure. Its impact is especially important as it is used to estimate the duration of each observation. Errors in QE characterization could lead to images being saturated due to integration times being too large.

Following this analysis, no specific consequences can be derived because of the significant uncertainty on the error levels of the measurements.

7.8. Persistence

The persistence of the HxRG detectors is supposed to be negligible for the operating of the MAJIS instrument. Based on the literature and previous testing, it is expected to be barely noticeable [5]. The persistence measurements require synchronization between the shutter closing and the acquisition of images (See Section

5.7).

7.8.1. Performance estimation

A series of twenty 512-rows images were captured with a 68 ms integration time (Fast acquisition mode). The first images were receiving a strong light flux. The shutter was closed around the middle of the series. The exact chronology of the events was not recorded. The following figure displays the median signal received for each image, with a reconstructed chronology of events, the two black dotted lines represent the closing of the shutter:

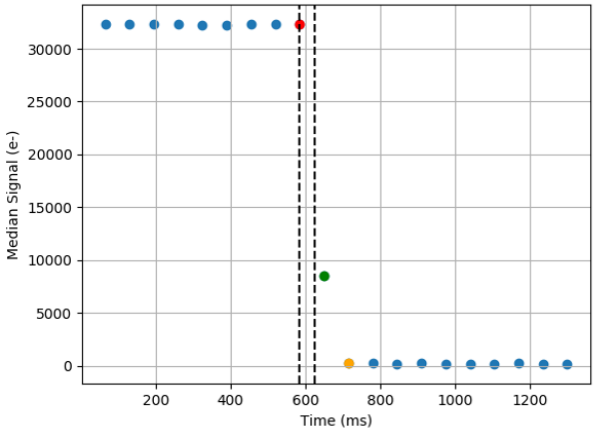

Figure 7.24: Persistence measurement median signal - Fast - 68ms DIT

From this figure, it appears that the CDS image following the closing of the shutter still shows a significant signal. The signal is much higher than the expected persistence. The following figures display the images corresponding to the red (last illuminated image) and green (first image after shutter closing) points on the previous figure:

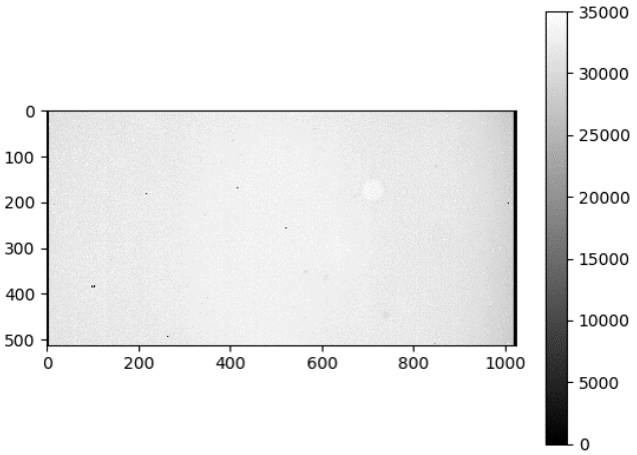

Figure 7.25: Image N°9 (red point) illuminated - Fast - 68ms DIT

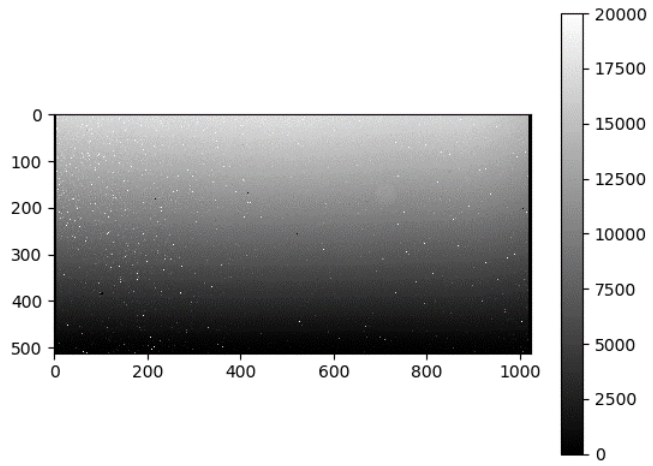

Figure 7.26: Image N°10 (green point) shutter closing - Fast - 68ms DIT

Each image is acquired row by row. From image N°10 it appears that the shutter closed during the acquisition of the image leading to the visible gradient. The first rows (shutter close to being open) received a lot of flux while the last rows (shutter almost closed) received less flux. The following figure describes the evolution of the median signal of the images using only the last rows that were acquired:

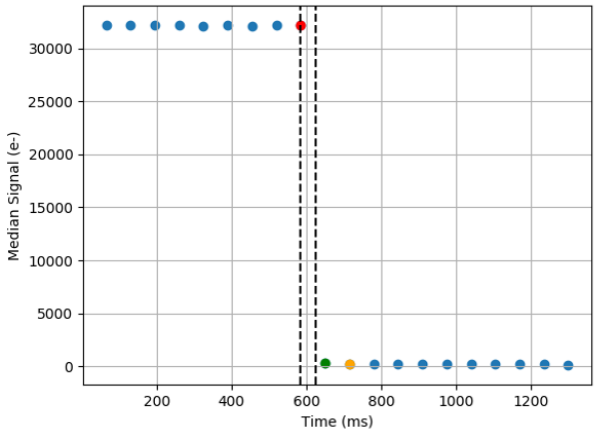

Figure 7.27: Persistence measurement last rows median signal - Fast - 68ms DIT

From this figure, it is clear that the persistence is much less than it seemed in Figure 7.24. Although, as it is unclear how exactly closed the shutter was, this figure does not give a straight estimate of the persistence.

For the flight campaigns, the synchronization of the shutter and the acquisitions will have to be implemented correctly to estimate accurately the persistence. It is noted that the measurement of this parameter is not considered essential to the success of the campaign

7.8.2. Consequences for the instrument in-flight

A high persistence could significantly deteriorate the performances of the instrument. It would impact the depth of well available for each image, and require post-processing for its removal. However, based on the low expected persistence on the flight detectors, there are no major consequences.

7.9. Performances summary

Measurement	Result	Conditions
Dark (closed)	2,600 e-/s/pix	Slow 100kHz – FPA 140K
Dark (closed)	370 e-/s/pix	Slow 100kHz – FPA 125K
Read-out Noise	10 e-/pix (ref.) 19 e-/pix (con.)	Slow 100kHz – FPA 125K
Read-out Noise	24 e-/pix (ref.) 32 e-/pix (con.)	Fast – FPA 125K
Dark (open)	N/A (Saturation)	Fast – FPA 125K
Dark (open) + SWPF	2,500 e-/s/pix	Fast – FPA 125K
Dark (open) (Windowing)	28,200 e-/pix (not saturated in 18 ms)	Fast – FPA 125K DIT 18 ms – 256 rows
Gain (validation)	2.0 e-/DN	Fast – FPA 125K
Linearity	Nominal	Fast – FPA 125K
Linearity	Not nominal (even with the correction coefficients)	Slow 100kHz – FPA 125K
QE (1.0,1.23,1.5 µm)	(1.2, 0.8, 0.9)	Fast – FPA 125K
Latency	Unsuccessful measurements	Fast – FPA 125K

Table 7.4: EM FPA Performances summary - Slow 100kHz

7.10. Conclusion

Due to errors in the radiometric model, significant black-body emissions are reaching the detector in the VIS-NIR experimental assembly. Still, it was possible to perform useful measurements as a result of the use of an SWPF and/or windowing.

The dark currents were shown to have increased over a short period of time. This might be due to the lesser quality of the engineering grade detector. It is expected that FM detectors will not show such increases.

Noise measurements have confirmed that the noise model was accurate. The RON measured were in line with the expected performances of HxRG detectors.

The linearity measurements showed an unstability. The origin of this unstability is still to be confirmed, but it is suspected to be linked to the radiance of the lamp. Using the linearity measurements, the conversion gain was also estimated.

Quantum efficiency measurements were not entirely successful. On some of the wavelengths sampled, QE higher than 1 were measured, but the error level was about 50% at most. Therefore, the order of magnitude for the photometry of the experimental assembly appeared to be right. Nevertheless, improvements will be required for the FM campaign.

Persistence measurements were not successful either. They will require that the shutter and the acquisition are synchronized.

8

Impact on MAJIS performances

For this thesis, two EM FPAs have been characterized. Their performances are not entirely representative of the performances of the FM detectors. But, their characterizations can be used to estimate the performances that can be expected of the FM detectors.

First, the performances that were assumed for the preliminary radiometric model are compared to the updated estimations of performances. Then, the impact of the dark current on the radiometric situation is addressed using Ganymede as an example. Finally, an analysis of the SNR performances of the MAJIS instrument is conducted.

8.1. Radiometric model

Chapter 3 gave a description of the assumed performances for the radiometric model. The following tables compare the performances used for the SNR analyses and the performances the EM MW-IR and VIS-NIR detectors have shown.

Detector performance parameter	**Expected performances**	**Measured performances**
Dark current (per binned pixel)	25 e-/sec	**<25 e-/sec (FM)** **<10,000 e-/sec** (FS)
Total read noise (per binned pixel) (Slow 100kHz)	40 e-	**35 e-**
Total read noise (per binned pixel) (Fast)	80 e-	**65 e-**
FWD (per binned pixel)	240,000 e-	> 300,000 e-
QE plateau	70-80 %	80 %

Table 8.1: Summary of VIS-NIR FPA performances

Detector performance parameter	**Expected performances**	**Measured performances**
Dark current (per binned pixel)	7000 e-/sec	**<6,000 e-/sec**
Total read noise (per binned pixel) (Slow 100kHz)	40 e-	**30 e-**
Total read noise (per binned pixel) (Fast)	80 e-	**65 e-**
FWD (per binned pixel)	160,000 e-	> 250,000 e-
Operability	99 %	99 % at 90K

Table 8.2: Summary of MW-IR FPA performances

Overall, the characterization campaigns have not highlighted any major problems with the initial assumptions on the performances of the detectors.

The performances shown by the EM detectors are promising.

In many respects, the EM detectors have outperformed the original assumptions.

However, the campaigns have highlighted several aspects that will have to be carefully monitored for the FM and FS campaigns. (Dark, operability, linearity)

8.2. Impact from the evolution of the dark

As described in Chapter 3, the MAJIS instrument will subtract dark current maps of its detectors when making observations. The acquisition of the dark current map occurs before a target frame is acquired. Changes in FPA temperatures can occur between the acquisition of a dark map and a target frame. The dark current's increase as a function of the temperature of the FPA has been described in Section 6.4. These changes in FPA temperatures can lead to errors in dark current subtraction, which would result in significant losses of radiometric accuracy.

The radiometric model for the three mainly targeted Galilean moons was developed internally (JUI-IAS-MAJ-TN-022). The following figure describes the expected VIS-NIR and MW-IR signal per 36 µm pixel for Ganymede, Europa and Callisto :

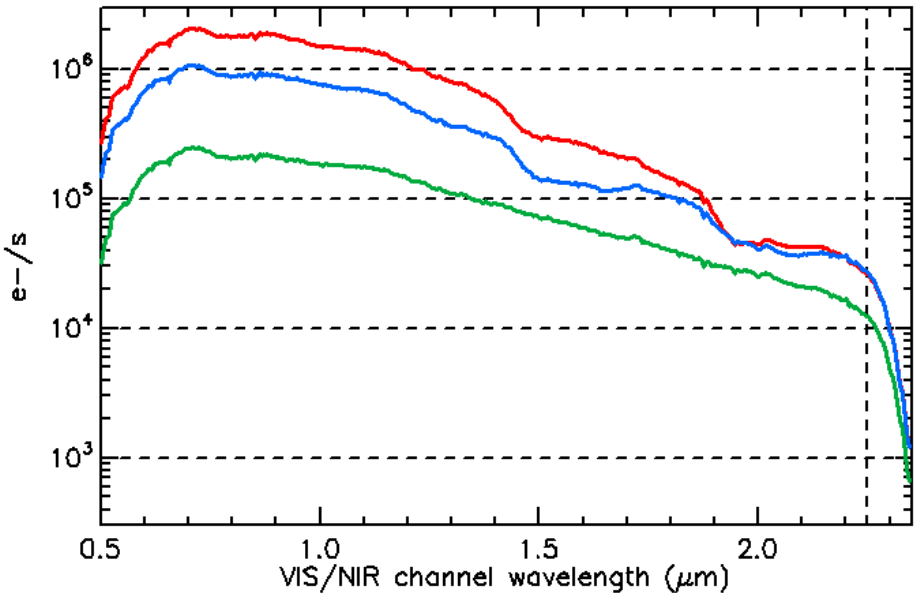

Figure 8.1: Signal in e-/s/pixel expected from Europa (red), Ganymede (blue) and Callisto (green) as a function of the wavelength for the VIS-NIR channel of MAJIS

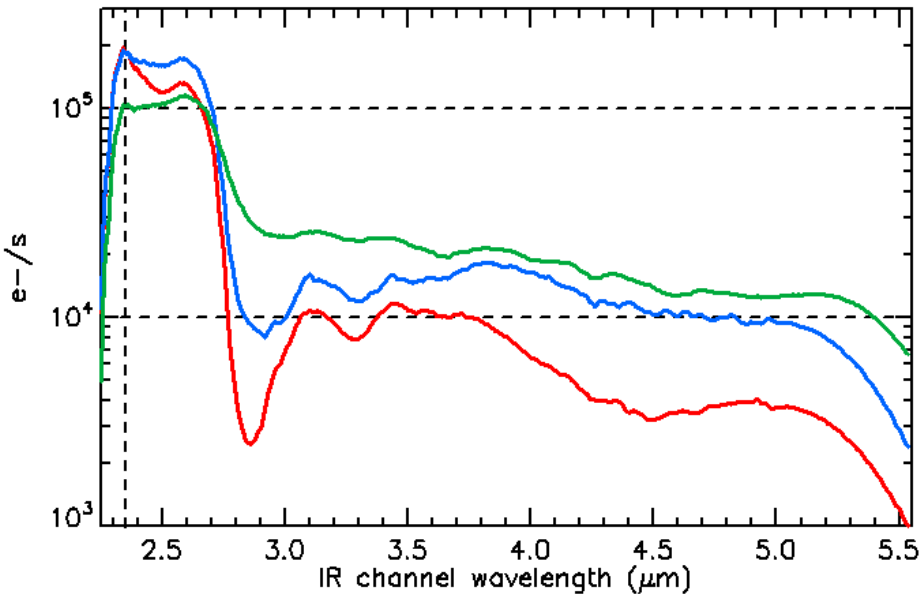

Figure 8.2: Signal in e-/s/pixel expected from Europa (red), Ganymede (blue) and Callisto (green) as a function of the wavelength for the MW-IR channel of MAJIS

This figure shows that for some of the wavelengths (>2.9 µm), signal ≤ 10,000 e-/s/pix can be expected for Ganymede and Europa. For these lower signal acquisitions, the impact of errors in dark current subtraction is more important. An analysis of the impact of errors in dark current subtraction was conducted (JUI-IAPS-MAJ-RP-007). The analysis compared the variations in the dark current to expected signals from Ganymede. Based on the results from Section 6.4, this analysis was completed. The formula used to compare variations in the dark due to variations in FPA temperature to an expected signal is the following:

$$R_{\Delta} = \frac{DC(T+\Delta T) - DC(T)}{S} \tag{8.1}$$

where R_{Δ} is the ratio used to estimate the radiometric impact, $DC(T)$ is the dark current at a given FPA temperature, T is the initial FPA temperature when the subtracted dark map was acquired, ΔT represents the change in FPA temperature between the dark and target frames, and S is the expected signal.

The following figures describe the ratio of variations in dark current to signal for two wavelengths of the Ganymede expected signal (2.0 and 3.3 µm) (see figure above). These wavelengths correspond to the water ice band and C-H stretch (organic species) The coordinates of a point on the following images are (ΔT, T). The magnitude of the point corresponds to the ratio R_{Δ}. This ratio was computed using interpolated dark current values based on measurements from the EM MW-IR campaign(see Figure 8.5).

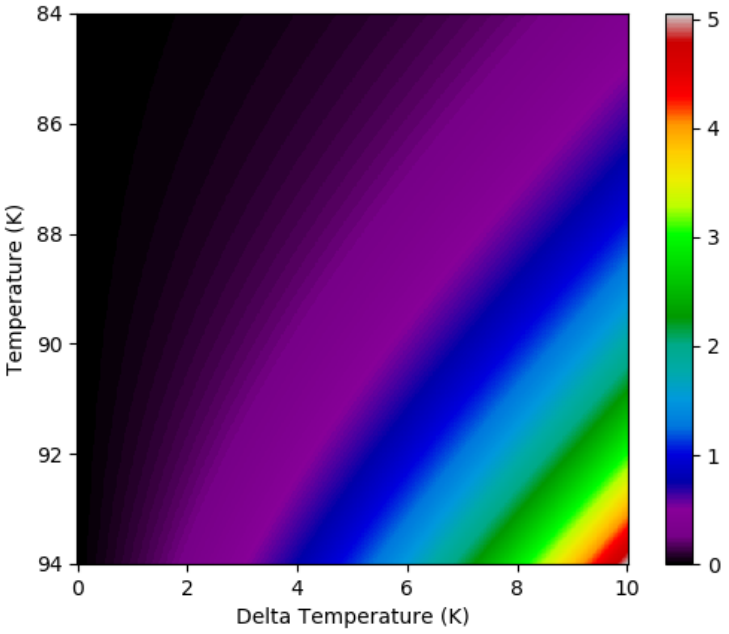

Figure 8.3: Influence of the dark current for Ganymede at 5 µm

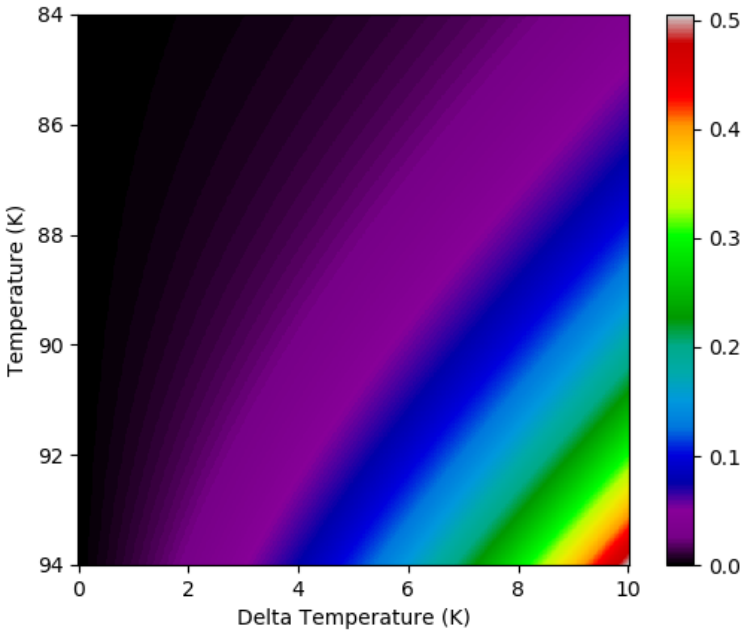

Figure 8.4: Influence of the dark current for Ganymede at 2.5 µm

These figures show that the variations in dark current can represent a significant signal increase. The impact will be different depending on the wavelength observed. Wavelengths for which the signals are lower are more sensitive. Observations made at high operating FPA temperature T are also more affected (i.e. at 90K increases in temperature will have a stronger negative impact than they would at 84K).

To avoid being affected by these variations the dark map used for the subtraction can be adapted. As it was shown in Figure 7.1, the dark signal holds the same cosmetic at different FPA temperatures. Only the magnitude of the dark current is affected by the increase in temperature. Furthermore, although Rule 07 has been shown to be a bad predictor for the evolution of the magnitude of dark currents as a function of the FPA temperature in Section 6.4, a simple exponential model can be used to interpolate the measurements of dark currents as shown in the following figure:

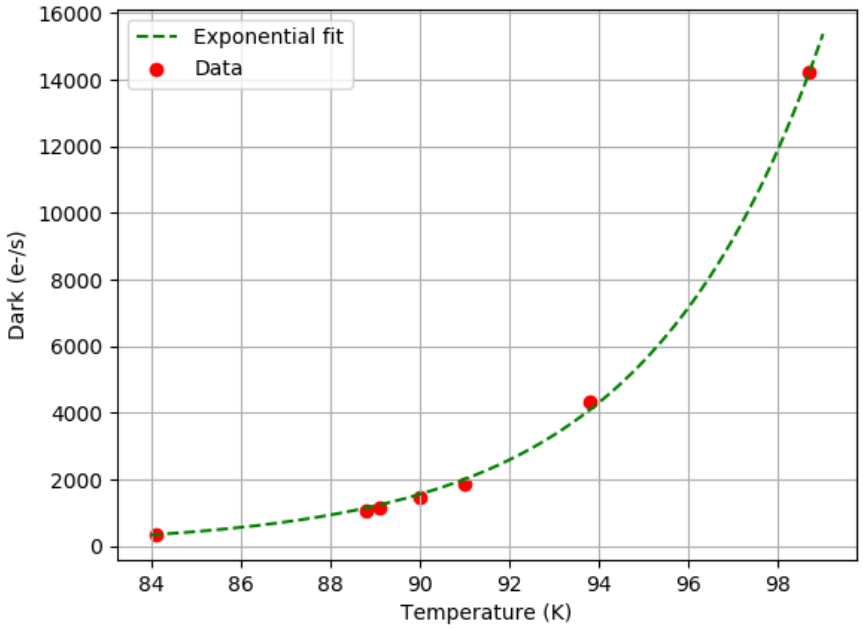

Figure 8.5: Interpolation of EM MW-IR FPA dark measurements using an exponential model

Temperature sensors are present on the MAJIS instrument to record the evolution of the MW-IR and VIS-NIR FPAs' temperature during the mission. Based on the previous remarks it is possible to highly reduce the impact of the dark variations. To do so, any dark map subtraction done by MAJIS should be scaled by a factor based on the interpolation of the exponential fit.

8.3. Impact of increase in temperature on MW-IR operability

Section 6.6 showed that for the MW-IR detectors, the operability rapidly decreased with increasing temperatures due to an overflow phenomenon. This could lead to a significant decrease in the operability of the FM detectors for temperatures within the operating range.

The following figures describe the impact of the phenomenon for a "hot" pixel with a very high dark current for temperatures ranging from 72K to 98K using the same integration time.

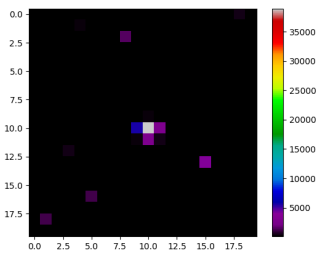

Figure 8.6: Hot pixel's dark current impact on neighboring pixels at 72K

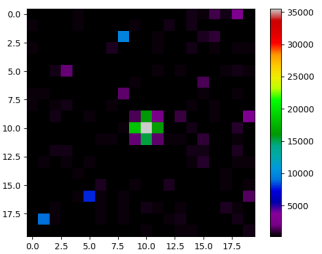

Figure 8.7: Hot pixel's dark current impact on neighboring pixels at 84K

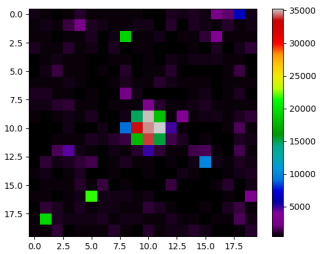

Figure 8.8: Hot pixel's dark current impact on neighboring pixels at 89K

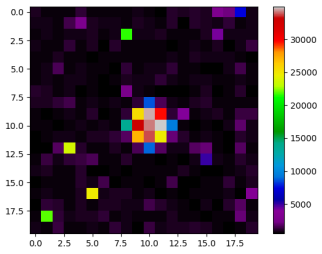

Figure 8.9: Hot pixel's dark current impact on neighboring pixels at 90K

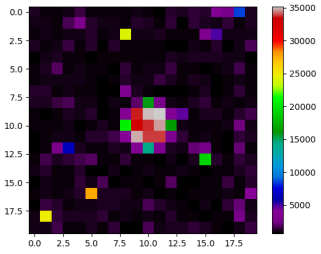

Figure 8.10: Hot pixel's dark current impact on neighboring pixels at 91K

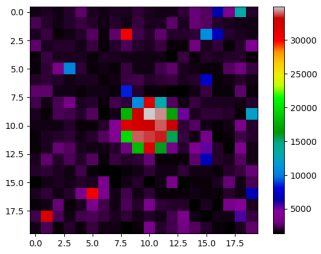

Figure 8.11: Hot pixel's dark current impact on neighboring pixels at 93K

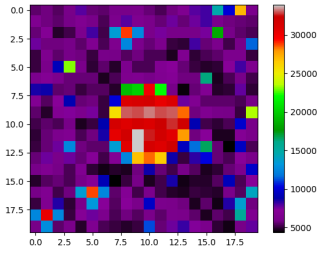

Figure 8.12: Hot pixel's dark current impact on neighboring pixels at 98K

Figure 8.6 shows that at 72K the center pixel was inoperable because saturated. Three of its neighbors are already affected by the overflowing dark current's electrons. From 72K to 98K more and more of its neighbors are affected and become inoperable. Using an arbitrary limit of 10,000e-, the number of pixels reaching this limit due to the overflow of the central pixel at the various temperatures is summarized in the table below:

FPA's Temperature (K)	72	84	89	90	91	93	98
Number of pixels affected	1	5	9	10	13	21	34

Table 8.3: Impact of temperature on MW-IR "hot" pixels

Table 8.3 shows that even with a detector with very low inoperability at 90K, the operability at higher temperatures can decrease rapidly due to the overflowing contaminating other pixels.

This indicates that for observations at high operating temperatures, the scientific returns of the MW-IR channel could be significantly diminished. Although, it is important to indicate that the operability requirement for the MW-IR FM detector is 99%. Therefore, even with a factor of 5, the large majority of the detector would still be usable.

8.4. Conclusion

This chapter has shown that the performances measured during the characterization campaigns can be summarized as better than the performances used for the SNR analyses performed by the MAJIS team. This implies that the characterization campaigns indicate that MAJIS should be able to reach its scientific goals.

An analysis of the evolution of dark currents has shown, using expected signals from Ganymede as a reference, that the dark currents are highly sensitive to the FPA temperature. This reinforces the critical importance of accurate dark subtraction in-flight to preserve the scientific value of the measurements.

Finally, the degradation of operability with temperature has shown to be a potential issue for the MW-IR channel. The impact of this issue will be highly dependent on the performances of the detector at 90K. If the requirements for the FM FPAs are met, the MW-IR detector should not be affected too significantly.

9

Conclusion

9.1. Conclusion

This MSc thesis was focused on the characterization of the detectors of the MAJIS instrument. The first part of the thesis was a literature study providing information on the background of the JUICE mission, the description of the MAJIS instrument and the physics of the detectors used. The second part of the thesis mainly revolved around the analysis of the data from the characterization campaign of the MW-IR and VIS-NIR EM detectors. The characterization of the **EM** detectors has shown that the MAJIS instrument could be expected to reach its scientific goals. Furthermore, these **EM** campaigns have allowed preparing for the characterization of the **FM/FS** detectors.

MAJIS scientific goals are very numerous, so that a complete and exhaustive review of these goals is out of scope this thesis. This thesis focused on the composition of the surface of Ganymede with the identification of two major expected components : ice water and organic species. To assess these science cases, SNR analyses were produced by the MAJIS team. The expected SNR levels highly depend on the performances of the detectors. These analyses showed that for the specific performances of the detectors described in Section 3.7, the identification of the species of interest was possible on Ganymede, even for HR observations (lower expected SNR).

However, it has been shown in Sections 3.2, 3.3, and 3.6 that the specific operational characteristics of the detectors would create new and original challenges due to the unusual conditions in which they will be used in terms of the large operational temperatures, low integration times, and numerous cosmic rays. Therefore, it was necessary to check that the performances described in Section 3.7 could be reached by the **FM/FS** detectors.

Following the descriptions of the performance parameters made in Section 4.5, specific characterization procedures were established in Chapter 5. These procedures have been followed during the characterization campaigns of the **EM** detectors and they will, also, be followed for the characterization of the **FM/FS** detectors with a few adaptations. All these procedures allowed to accurately assess the performances of the detectors and determine whether they were compliant with the performances required to reach the scientific objectives of MAJIS. Two experimental assemblies (VIS-NIR and MW-IR) have been developed to allow for the characterization procedures to be performed on the detectors.

The analyses of the MW-IR **EM** detector campaign have shown that reducing the stray-light to a satisfying level (negligible compared to dark measurements) was a real challenge for the experimental set-up. Yet, measurements could still be produced by getting rid of it through post-processing. The linearity of HxRG detectors was shown to be complex. It was particularly intricate around the beginning and the saturation of the well. The dark currents levels were shown to significantly increase with temperature, this increase can be modeled using an exponential fit. However, the Rule 07 [40] does not accurately describe this evolution. The theoretical noise model was validated by the measurements performed. Furthermore, the RON estimated was better than the assumed noise used in Section 3.7. While within the operating range (120-160K) the FPE temperature did not have an impact on the performances of the detector. Finally, the campaign showed that an increase of the FPA temperature could lead to a significant decrease in operability. This is due to a phenomenon where single inoperable pixels transform into clusters of inoperable pixels when the temperature increases.

The analysis of the VIS-NIR **EM** detector campaign showed that the VIS-NIR experimental set-up design was flawed due to an underestimation of the black-body emissions by the Belgium partner in charge of the setup. Nevertheless, the characterization campaign still produced a large number of significant measurements. This detector was not representative of the **FM** VIS-NIR detector w.r.t. the dark current. Therefore, the measurements in and of themselves can not be translated to the performances expected of the **FM** VIS-NIR detector. However, a significant increase (doubled in a year) in dark current was noticed for these detectors. Although the **FM** detectors are expected to be more stable, the dark stability will be monitored closely. The RON measured with the **EM** were below the ones used in Section 3.7. The linearity of the detector was satisfying with the Fast mode, however, the Slow linearity measurements were not successful (due to experimental set-up instability). The radiometry of the set-up did not permit to precisely estimate the QE of the detector.

Overall, the performances that the **EM** detectors displayed were satisfying as they were better than the performances that were assumed by the MAJIS team to conclude that MAJIS would reach its scientific objectives (Section 8.1). Based on the characterization of the **EM** detectors, the **FM** detectors are expected to significantly surpass the performances required to fulfill the scientific objectives.

On some specific aspects, the **EM** detectors have led to reservations. For these potential issues, the **FM** detectors will be closely monitored. First, the detector's dark currents dependency with temperature was shown to possibly lead to a significant loss in SNR. Additionally, increases in dark current due to the storage of the detectors could significantly hurt the scientific returns of MAJIS. Finally, the rapid decrease in operability for **MW-IR** detectors with increasing temperature is an unexpected issue that can depreciate the **MW-IR** channel measurements.

9.2. Recommendations

9.2.1. Scripts and procedures

During this MSc thesis, scripts and procedures were developed for the characterization of the **EM** detectors. These scripts and procedures can be used for the upcoming **FM/FS** campaigns. Improvements could be made to better estimate some of the performance parameters.

Most notably, the Conversion Gain procedure as presented in Section 5.6, only takes into account start-of-the-well measurements to estimate the initial gain. A possible improvement would be to characterize the evolution of the local gain using measurements at different levels of filling of the well.

9.2.2. Planning of FM campaign

The planning of the campaigns will have to take into account the issues highlighted by the characterization of the EM campaigns. The linearity characterization should use fine spacing around both edges of the linear range to take into account the non-standard behaviors observed during the EM MW-IR campaign. Also, the characterization of the dark current should be used to monitor any possible increase due to the storage of the detectors.

9.2.3. Experimental assembly improvements

Issues with the VIS-NIR and IR experimental set-ups should be fixed or mitigated before the FM/FS campaigns.

The dominant stray-light in the VIS-NIR experimental assembly set-up will not be eliminated in time for the FM campaign. Yet, efforts should be made to better understand the filtering of black-body emissions that the SWPF provides. A different SWPF could be used to let shorter wavelengths pass increasing the range of usable wavelengths.

On the MW-IR assembly, many improvements have been made to reduce the stray light to the levels that were observed during the EM campaign. Further reducing the stray-light might require too much time and effort to be an efficient use of the time available.

The VIS-NIR set-up reported issues with the stability of the radiance (see Section 7.5.2). A stable light flux is required for most of the characterization campaign. Therefore, it is essential that the team solves these issues before the start of the FM campaign.

9.2.4. Unresolved issues

Some issues mentioned during the campaigns are still unresolved and could warrant further investigation.

So far, the evolution of the local gain has not been explored in detail. Therefore, its exact impact on the performances and, specifically, on the noise model is not entirely understood. This should be addressed by

the FM/FS characterization campaigns.

Another effect that was not completely resolved by the EM characterization campaigns is the decrease in operability for increasing temperatures for the MW-IR detectors. The exact evolution with respect to the temperature should be characterized. Furthermore, it appears that for the MW-IR detectors the saturated pixels electrons overflow in their neighbors' wells, this effect should be characterized accurately.

A

IR filter and Optical Head performances

This appendix presents the current expected performances of the OH and IR filter for reference.

OH performance parameter	**iPDR assumptions**	**Current assumptions**
OH background temperature	140 K nominal	140 K nominal
Optical efficiency	Peak 30%	Peak at 55 %
Grating dispersion	Assumed linear from first to last spectel of detector	Use nominal dispersion equation from LDO

Table A.1: Summary of assumed OH performances

IR filter performance parameter	**iPDR assumptions**	**Current assumptions**
Cold baffled housing height	2.9 cm	2.9 cm
Filter sizes	Made to match detector FOV (inc. aperture angle)	Made to match detector FOV (inc. aperture angle)
LVF coating to detector distance	1 mm	1 mm
Smile effect	29 nm	23 nm
LVF FWHM	5.0 % CWL	Custom
Order blocking	OD3 everywhere	OD4 (LVF)
BPF peak transmission	80%	90%

Table A.2: Summary of assumed IR filter performances

Bibliography

[1] J Arenberg, J Flynn, A Cohen, R Lynch, and J Cooper. Status of the jwst sunshield and spacecraft. In *Space Telescopes and Instrumentation 2016: Optical, Infrared, and Millimeter Wave*, volume 9904, page 990405. International Society for Optics and Photonics, 2016.

[2] James W Beletic, Richard Blank, David Gulbransen, Donald Lee, Markus Loose, Eric C Piquette, Thomas Sprafke, William E Tennant, Majid Zandian, and Joseph Zino. Teledyne Imaging Sensors: infrared imaging technologies for astronomy and civil space. In *High Energy, Optical, and Infrared Detectors for Astronomy III*, volume 7021, page 70210H. International Society for Optics and Photonics, 2008.

[3] Nagaraja Bezawada, Derek Ives, and David Atkinson. Conversion gain non-linearity and its correction in hybridised near infrared detectors. In *Focal Plane Arrays for Space Telescopes III*, volume 6690, page 669005. International Society for Optics and Photonics, 2007.

[4] Michael T Bland, Adam P Showman, and Gabriel Tobie. The production of Ganymede's magnetic field. *Icarus*, 198(2):384–399, 2008.

[5] R Blank, S Anglin, JW Beletic, Y Baia, S Buck, S Bhargava, J Chen, D Cooper, M Eads, M Farris, et al. The HxRG Family of High Performance Image Sensors for Astronomy. In *Solar Polarization 6*, volume 437, page 383, 2011.

[6] Richard Blank, Selmer Anglin, James W Beletic, Sid Bhargava, Ryan Bradley, Craig A Cabelli, Jing Chen, Don Cooper, Rick Demers, Michael Eads, et al. H2rg focal plane array and camera performance update. In *High Energy, Optical, and Infrared Detectors for Astronomy V*, volume 8453, page 845310. International Society for Optics and Photonics, 2012.

[7] Karl W Böer and Udo W Pohl. *Semiconductor physics*. Springer, 2018.

[8] A. Boutonnet, J. Schoenmaekers, W. Martens, and T. Yamaguchi. JUICE: Consolidated Report on Mission Analysis (CReMA). In *WP-578*. ESA, 2014.

[9] Pierre-Elie Crouzet. *Etude des proprietes d'un detecteur infrarouge H2RG pour l'optimisation d'un spectrographe embarque sur le satellite SNAP/JDEM*. PhD thesis, Université de la Méditerranée - Aix-Marseille II, 2009.

[10] Nibir K Dhar, Ravi Dat, and Ashok K Sood. Advances in infrared detector array technology. *Optoelectronics-Advanced Materials and Devices*, 7:149–188, 2013.

[11] TM Edwards, EJ Bunce, and SWH Cowley. A note on the vector potential of connerney et al.'s model of the equatorial current sheet in jupiter's magnetosphere. *Planetary and Space Science*, 49(10-11):1115–1123, 2001.

[12] Linda Elkins-Tanton. *Saturn and Jupiter*. Chelsea House Publications, 2006.

[13] ESA. ESA's 'Cosmic Vision'. `https://jwst.nasa.gov/content/observatory/sunshield.html`, 2014. Accessed: 2020-03-03.

[14] ESA. CREMA 3.0 interactive 3D tool. `https://www.cosmos.esa.int/web/juice/crema-3.0`, 2018. Accessed: 2019-01-08.

[15] ESA. JUICE Science Payload. `http://sci.esa.int/juice/50073-science-payload/`, 2018. Accessed: 2019-31-07.

[16] WM Folkner, R Woo, and S Nandi. Ammonia abundance in Jupiter's atmosphere derived from the attenuation of the Galileo probe's radio signal. *Journal of Geophysical Research: Planets*, 103(E10):22847–22855, 1998.

[17] Richard Greenberg, Paul Geissler, Gregory Hoppa, B Randall Tufts, Daniel D Durda, Robert Pappalardo, James W Head, Ronald Greeley, Robert Sullivan, and Michael H Carr. Tectonic processes on Europa: Tidal stresses, mechanical response, and visible features. *Icarus*, 135(1):64–78, 1998.

[18] Pierre Guiot. *L'expérience MAJIS: développement d'un imageur spectral pour les lunes de Jupiter*. PhD thesis, Université Paris-Saclay, 2019.

[19] James R Janesick, K Kalassen, and T Elliott. Ccd characterization using the photon transfer technique. In *Proc. SPIE*, volume 570, pages 7–19, 1985.

[20] TV Johnson, CM Yeates, and R Young. Space science reviews volume on Galileo mission overview. In *The Galileo Mission*, pages 3–21. Springer, 1992.

[21] OL Kuskov and VA Kronrod. Internal structure of Europa and Callisto. *Icarus*, 177(2):550–569, 2005.

[22] Sunwoong Lee, Robert T Pappalardo, and Nicholas C Makris. Mechanics of tidally driven fractures in Europa's ice shell. *Icarus*, 177(2):367–379, 2005.

[23] Alfred S McEwen, Laszlo Keszthelyi, Paul Geissler, Damon P Simonelli, Michael H Carr, Torrence V Johnson, Kenneth P Klaasen, H Herbert Breneman, Todd J Jones, James M Kaufman, et al. Active volcanism on Io as seen by Galileo SSI. *Icarus*, 135(1):181–219, 1998.

[24] Arturo Morales-Acevedo. Thin film CdS/CdTe solar cells: research perspectives. *Solar Energy*, 80(6): 675–681, 2006.

[25] NASA. PIA01081: Color Mosaic and Active Volcanic Plumes on Io. `https://photojournal.jpl.nasa.gov/catalog/PIA01081`, 1997. Accessed: 2020-03-03.

[26] NASA. Mission to Jupiter Galileo. `https://www.jpl.nasa.gov/missions/galileo/`, 2014. Accessed: 2020-03-03.

[27] NASA. Possible 'Moonwich' of Ice and Oceans on Ganymede (Artist's Concept). `https://www.jpl.nasa.gov/spaceimages/details.php?id=PIA18005`, 2014. Accessed: 2020-03-03.

[28] NASA. JWST: ABOUT THE SUNSHIELD. `http://www.esa.int/Science_Exploration/Space_Science/ESA_s_Cosmic_Vision`, 2016. Accessed: 2020-02-02.

[29] G Piccioni and Y Langevin. MAJIS (Moons And Jupiter Imaging Spectrometer) for JUICE: Jupiter system objectives. *EPSC abstracts*, 8, 2013.

[30] AA Plazas, C Shapiro, R Smith, J Rhodes, and E Huff. Nonlinearity and pixel shifting effects in HXRG infrared detectors. *Journal of Instrumentation*, 12(04):C04009, 2017.

[31] Zachary Prieskorn, Christopher V Griffith, Stephen D Bongiorno, Abraham D Falcone, and David N Burrows. Characterization of Si hybrid CMOS detectors for use in the soft X-ray band. *Nuclear Instruments and Methods in Physics Research Section A: Accelerators, Spectrometers, Detectors and Associated Equipment*, 717:83–93, 2013.

[32] George Rieke and Rieke George. *Detection of Light: from the Ultraviolet to the Submillimeter*. Cambridge University Press, 2003.

[33] Antoni Rogalski. Infrared detectors: an overview. *Infrared Physics & Technology*, 43(3-5):187–210, 2002.

[34] Antonio Rogalski. *Infrared detectors*. CRC press, 2010.

[35] Michael Rowan-Robinson. *Night vision: Exploring the infrared universe*. Cambridge University Press, 2013.

[36] Joe Schmit, Paul Kruse, and Ernie Stelzer. Development of a 0.1 eV bandgap semiconductor at the Honeywell Research Center (1959-1985). In *Infrared Technology and Applications XXXV*, volume 7298, page 72982R. International Society for Optics and Photonics, 2009.

[37] G Smadja, C Cerna, and A Ealet. Measurement of the non-linearity and interpixel capacitance of a h2rg (2k× 2k) near-ir detector. *Nuclear Instruments and Methods in Physics Research Section A: Accelerators, Spectrometers, Detectors and Associated Equipment*, 610(2):615–621, 2009.

[38] RA Soref. Extrinsic IR photoconductivity of Si doped with B, Al, Ga, P, As, or Sb. *Journal of Applied Physics*, 38(13):5201–5209, 1967.

[39] Simon M Sze and Kwok K Ng. *Physics of semiconductor devices*. John wiley & sons, 2006.

[40] WE Tennant. Rule 07 revisited: Still a good heuristic predictor of p/n HgCdTe photodiode performance? *Journal of Electronic Materials*, 39(7):1030–1035, 2010.

[41] D. Titov, O. Grasset, and L. Fletcher. JUICE: Science Requirements Document. In *Science Requirements Document*. ESA, 2014.